THE EFFECT OF DESIGN VARIATIONS ON STRESSES IN TOTAL ANKLE ARTHROPLASTY

by

Karol Galik

B. S. in M. E., University of Transport and Communications, Zilina, Slovak Republic

M.S. in M.E. University of Pittsburgh, Pittsburgh, PA

Submitted to the Graduate Faculty of

School of Engineering in partial fulfillment

of the requirements for the degree of

Doctor of Philosophy

University of Pittsburgh

2002

UNIVERSITY OF PITTSBURGH

SCHOOL OF ENGINEERING

This dissertation was presented

by

Karol Galik

It was defended on

April 12, 2002

and approved by

Stephen Conti, M.D., Associate Professor, Orthopaedic Surgery

Christopher Earls, Ph.D., Associate Professor, Civil Engineering

Mark Miller, Ph.D., Assistant Research Professor, Mechanical Engineering

Oladipo Onipede, Ph.D., Assistant Professor, Mechanical Engineering

Dissertation Director, Patrick Smolinski, Ph.D., Associate Professor, Mechanical Engineering

THE EFFECT OF DESIGN VARIATIONS ON STRESSES IN TOTAL ANKLE ARTHROPLASTY

Karol Galik, Ph.D.

University of Pittsburgh, 2002

The objective of this study was to analyze stresses and strains in the talus and the Ultra-High-Molecular-Polyethylene (UHMWPE) insert with two talar component designs of the Agility® ankle implant. A three-dimensional finite element method (FEM) model of the tibia, fibula, talus and the implant was developed for the study. An analytical solution of two counterformal cylinders was derived and a two-dimensional cross-sectional FEM model was included to investigate how the results of stresses in the UHMWPE correlate to the three-dimensional model.

The analysis of the three-dimensional model found stress concentrations in the UHMWPE due to edges of the talar components. The wider talar component decreased stresses in the middle of the sagittal plane below the yield limit, although, the peak stresses at the edges remained unchanged. We showed that it was possible for von Mises stress to increase while contact pressure decreased. This phenomenon was observed for different Poisson's ratios and thicknesses of the UHMWPE insert. We found that there was a qualitative discrepancy between the results from two-dimensional models and the

three-dimensional model for the narrower original talar design which was directly related to the assumption of plane strain condition of the two-dimensional model.

The potential subsidence of talar component of the implant into the cancellous bone of the talus was investigated based on strain failure criteria. Results showed that the edges produced localized yielding of cancellous bone in both of the talar component designs. The yielding zone was wider in the narrower implant. A failure of cancellous bone, defined as 1.5% strain, was predicted for both of the talar components on the posterior-medial corner. The strain in this corner reached 1.7% for the wider component and 2.6% for the narrower component. The average strain fell from 0.39% for the standard talar component to 0.3% for the modified component, both below the yield strain of 0.8%. In studying the effect of flexion angle, a full support of the talar component by cortical bone was found to be beneficial.

DESCRIPTORS

Ankle joint implant

Finite element model

Tibia

Polyethylene

Polyethylene thickness

Fibula

Talus

Total ankle arthroplasty

UHMWPE

Conformal cylinders

ACKNOWLEDGMENTS

I would like to thank my advisors Dr. Patrick Smolinski and Dr. Mark Miller for their invaluable help over the whole course of my study and especially in the final stages of computer simulation and interpretation of results. I am grateful for research support from DePuy, Warsaw, Indiana and Dr. Stephen Conti, Orthopeadic surgeon from UPMC Hospital, Pittsburgh PA.

A would specially thank to my family, my wife Amy who made the work much more enjoyable. Thanks to my son Alex with whom I could refresh my mind on the many ski trips we made to the local ski resort.

TABLE OF CONTENTS

LIST OF TABLES

LIST OF FIGURES

1.0 INTRODUCTION

Total ankle arthroplasty (TAA) is the process of replacing a diseased natural ankle with a prosthetic implant. Inspired by the success rate of hip and knee arthroplasty, several ankle implants were developed in the early and mid 1970's.[1] However, these implants produced unsatisfactory results in longer follow-up periods.[2] Implants were previously improved intuitively, based on clinical reports. Little or no experimental or analytical stress analysis was done using bone-implant models. Because of the complex nature of the models, the most widely used analytical approach has been the finite element method (FEM). Numerous FEM models have been created for hip and knee arthroplasty, but few can be found for ankle arthroplasty[3-7] or for the ankle joint in general.[8-14] No three-dimensional model of total ankle arthroplasty has included more than one bone. Detailed three-dimensional models of bones and soft tissues around the ankle have been developed[8, 11-14], but were used in studies other than arthroplasty. And only recently an article was published investigating stresses in two ankle implant designs although without bones in the model.[15]

To our knowledge, this model is the first three-dimensional model that contains an ankle implant with all surrounding bones of the ankle joint. This work will study one particular ankle joint implant, the Agility® ankle implant, produced by DePuy (Warsaw, Indiana) which consists of three parts: a tibial metallic tray, an ultra-high-molecular-weight polyethylene (UHMWPE) insert and a talar metallic component. The tibial tray spans the fused tibiofibular syndesmosis and the design has proven to be successful in

limited clinical use. Since 1988, there have been two reported fractures of the tibial tray and no reports of subsidence or aseptic loosening. The tibial tray has subsequently been thickened and no fractures have been reported since. The talar component is believed to be prone to subsidence and has been recently modified. The original shape of the talar component, in an attempt to preserve original kinematics of the ankle joint, narrowed significantly anterior-posteriorly, mimicking the shape of the talus. It is much narrower medio-laterally than to the tibial component. The modified talar component is almost as wide posteriorly as anteriorly to increase the articulating area between the component and UHMWPE insert. In addition, a base was added to increase the interface area between the talus and the implant.

The objective of this study is a parametric stress and strain analysis of the Agility® ankle joint implant in the talus and in the UHMWPE insert due to the change in the shape of the talar component. The talar component and the UHMWPE insert almost conform in the sagittal plane and have a flat-on-flat type of contact in the frontal plane. A simplified model of two conformal cylinders may approximate these bodies. For this reason an analytical solution of two counterformal cylinders was derived and compared to the three-dimensional FEM model. In addition, a two-dimensional FEM model of the implant cross-section was created to investigate how this widely used technique corresponds to the three-dimensional model. It is generally believed that an increased thickness of the UHMWPE insert decreases contact pressure at the articulating surfaces. This hypothesis was examined for this particular implants design. An investigation of possible failure of the talus was performed in the neutral position and three positions of

dorsi-plantar flexion. The talar bone was assigned heterogeneous elasto-plastic properties for cancellous bone to account for variation of density and modes of failure in tension and compression.

2.0 BACKGROUND

2.1 Anatomy of the Ankle Joint

The ankle joint is created by articulations among the tibia, fibula, and talus. The tibiofibular articulation is a syndesmosis: a joint with little movement limited by a tight ligament. The tibiotalar joint is a synovial joint: a joint allowing a great range of motion, filled with sinovial fluid. The tibia, fibula, and talus meet to create the ankle joint.

The tibia is located on the medial side of the leg and has a greater cross section than the second long bone of the leg, the fibula (Figure 2.1). The tibia is in a direct line between the femur and the talus, and carries most of the load (see Section 3.3). The tibial shaft is triangular in cross section.[16]

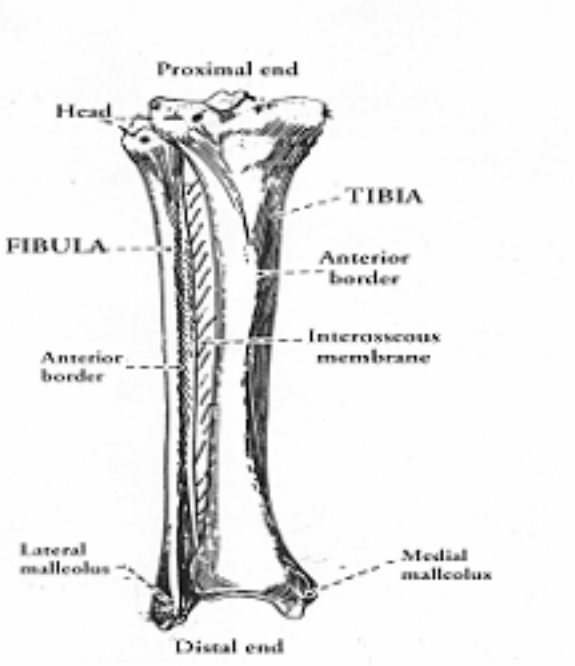

Figure 2.1 Anterior view of the tibia and fibula (adapted from Rosse[17]).

A cross section of the shaft of the tibia is distinguished by anterior, interosseous and medial borders which divide the surface of the tibia into medial, lateral and posterior surfaces (Figure 2.2). The anterior border, also called the crest of the tibia or the shin, is the most dominant of the three borders. The medial border is smooth and rounded superiorly and inferiorly, but more prominent at the coronal midplane of the tibia. The interosseous border provides for the interosseous membrane that connects the tibia and the fibula. The medial malleolus causes the distal end of the tibia to be asymmetric and enlarges the surface area of the ankle joint.

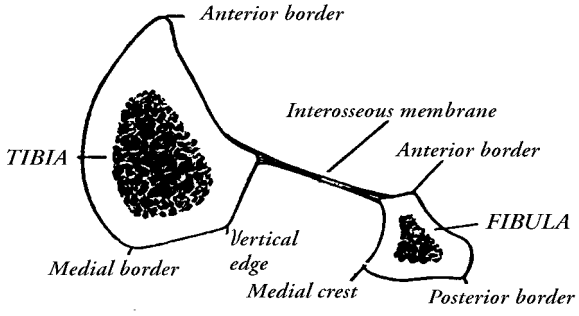

Figure 2.2 Transverse cross section through the right tibia and fibula[16]

The fibula has a much smaller cross section than the tibia and varies in cross-section due to the attachment of muscles and ligaments. The shaft has three borders: anterior, posterior, and interosseous; and three surfaces: medial, lateral, and posterior. The distal extremity, also called the lateral malleolus, has a triangular articular facet that contacts the lateral side of the talus and has a convex, lateral surface that articulates with

the rough concave medial surface of the tibia. This articulation stabilizes the ankle joint in dorsi/plantarflexion.

The talus is the only bone of the foot articulating with the tibia and the fibula. It also articulates with the calcaneus distally and with the navicular anteriorly. The talus has a rounded head, a neck, and a cuboidal body (Figure 2.3).

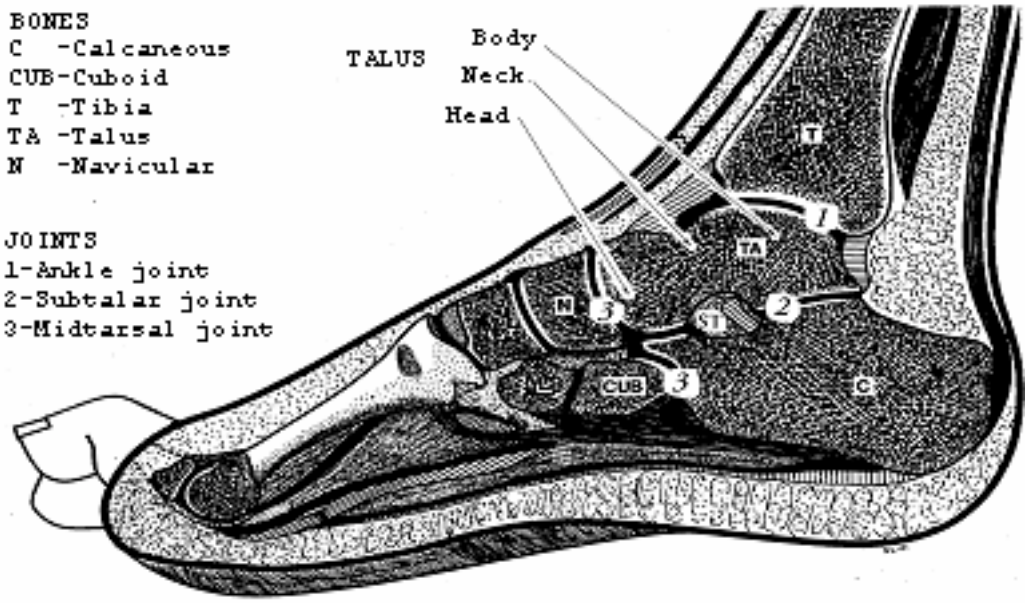

Figure 2.3 Sagittal section of the right foot (adapted from Jacques[18])

The surface of the head of the talus articulates with the navicular. The neck of the talus is smaller in cross sectional area than the head and is the most fracture prone part of the talus. The body of the talus is almost entirely covered with articular cartilage. The superior surface of the talus (the dome) articulates with the distal tibia. The most distal part of the body articulates with the calcanaeus. The other two articular surfaces of the talus are the lateral surface connecting to the lateral malleolus (distal end of the fibula)

and the medial surface connecting to the medial malleolus (distal end of the tibia). According to Inman,[19] the radius of curvature of the trochlea is smaller on the medial than on the lateral side. As a result, the trochlea are of conical rather then cylindrical shape (Figure 2.4) causing the ankle joint axis to be tilted in the frontal plane (the ankle joint axis is discussed further in Section 2.3).

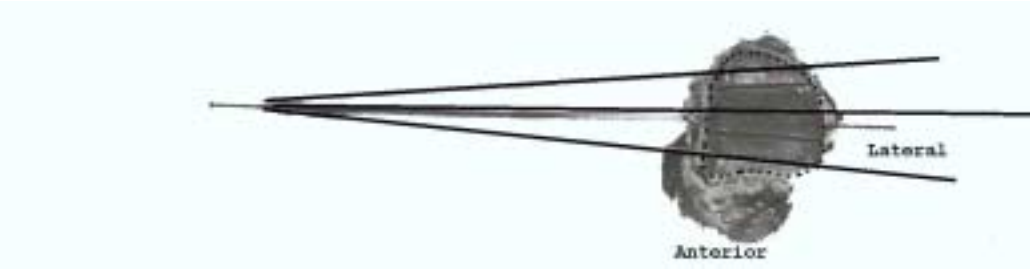

Figure 2.4 Conical shape of the trochlea.[19] Trochlear surface highlighted by dotted line

2.2 The Joints of the Foot

There are three joints in the foot that allow most of the motion: the ankle joint, also called the talocrural joint; the subtalar joint; and the midtarsal joints. The remaining joints of the foot allow only small motions and do not require frequent medical attention.[20]

The ankle joint, created by talo-tibial-fibular articulations, is not a hinge joint because the axis of rotation moves anterio-posteriorly during flexion. The main motion of the ankle joint is in the sagittal plane (see Appendix), averaging 70 degrees of motion, of which 20 degrees is in dorsiflexion and 50 degrees is in plantarflexion.[2] However, as shown on Figure 2.5, during walking the range of motion is limited to 25 degrees, of which 10 degrees is in dorsiflexion and 15 degrees is in plantarflexion.[2, 21] Besides these

main motions in the sagittal plane, the ankle joint allows approximately five degrees of rotation in the transverse plane about the vertical axis. This rotation in the transverse plane is called adduction (external rotation) or abduction (internal rotation), depending on whether the foot rotates away from the mid-line body axis or towards it. These motions in the sagittal and transverse planes are coupled so that dorsiflexion-abduction and plantarflexion-adduction occur at the same time.

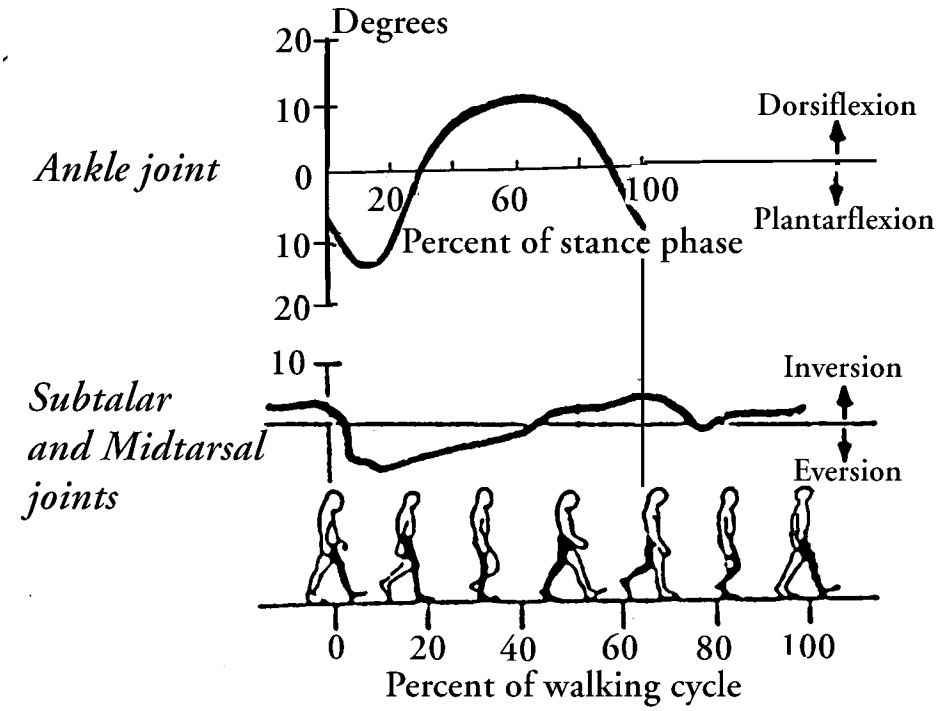

Figure 2.5 Range of motions during walking for the ankle, subtalar and midtarsal joints (adapted and combined from Pal[22] and Stauffer[21])

The subtalar joint, created by talo-calcaneal articulation, and the midtarsal joints, created by cubo-calcaneal and talo-navicular articulations (Figure 2.3), primarily allow rotary motions in the frontal plane. These rotary motions are called inversion and eversion. A loss of inversion and eversion due to disease results in disability, because the foot cannot adapt to walking on uneven surfaces.

The ankle, subtalar, and midtarsal joints move simultaneously so that when the foot dorsiflexes and abducts in the ankle joint, it everts in the other two joints, resulting in a complex motion called pronation. Conversely, when the foot plantarflexes and adducts, it also inverts. This combination of motions is called supination.

The relative motions among the joints of the foot gain significance when one of the joints is fused. Fusion, also called arthrodesis, of the subtalar joint transfers more rotation to the ankle joint. Arthrodesis of the ankle joint results in the loss of 50% of supination[23] and in subsequent higher stresses in the subtalar and midtarsal joints.[2] A fused subtalar joint may cause development of a ball-and-socket ankle joint as the foot tries to accommodate internal/external rotation.[24]

2.3 Axis of Motion of the Ankle Joint

The lower success rate of ankle implants compared to hip and knee implants may be related to an inability to restore the original kinematics of the ankle joint.[4, 23, 25-29] An understanding of ankle joint kinematics and determination of the ankle axis of rotation is a necessary preliminary step in the design and implantation of ankle prostheses.

Earlier studies on ankle joint kinematics considered the articular surfaces to be the only constraints and neglected the role of ligaments. Inman[30] for instance, assumed that the ankle joint rotated around one fixed axis. Anatomy textbooks refer to this axis as the empirical axis of the ankle joint and it has been used to position implants in many ankle designs.[4, 31-33] The location of the empirical ankle axis in the transverse plane can be defined in three approximately equivalent ways: 1) inclined 20°-30° with respect to the knee axis (Figure 2.6A) which is approximately perpendicular to the line of progression, 2) inclined at an average angle of 84° from the midline axis of the foot (Figure 2.6A) or, 3) passing through the centers of malleoli (Figure 2.6B).

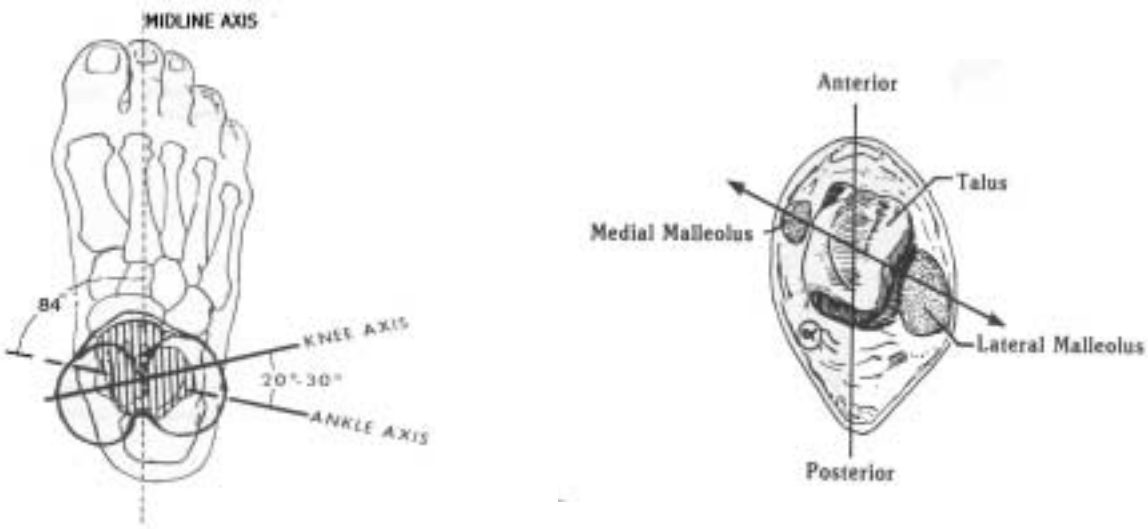

A B

Figure 2.6 Empirical ankle axis in the transversal plane. A) Ankle axis with respect to the ankle axis and midline of the foot (adapted from Mann[24]) B) Ankle axis passes though the centers of the malleoli[34]

In the frontal plane, the empirical ankle axis is at an angle of 80° to the centroidal longitudinal axis of the tibia (Figure 2.7) and passes just distal to the tips of the malleoli. As a result, this ankle axis can be determined clinically by placing fingers on the tips of malleoli. The tilt of the ankle joint axis in the frontal plane causes the foot to toe out (evert) in dorsiflexion and to toe in (invert) in plantarflexion.

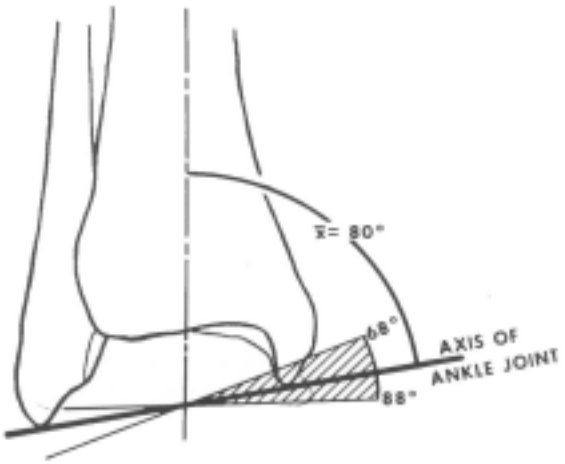

Figure 2.7 Empirical ankle axis in the frontal plane[24]

Prior to Inman, Barnett and Napier[35] and Hicks[36] described three distinct axes of ankle joint during flexion based on measurements of the curvature of the talar trochlea. In the neutral position (N), the axis was almost horizontal. In dorsiflexion (DF) and plantarflexion (PF), the axis was inclined upwards medially and laterally respectively (Figure 2.8). The change between these axes was reported to occur abruptly near the neutral position.

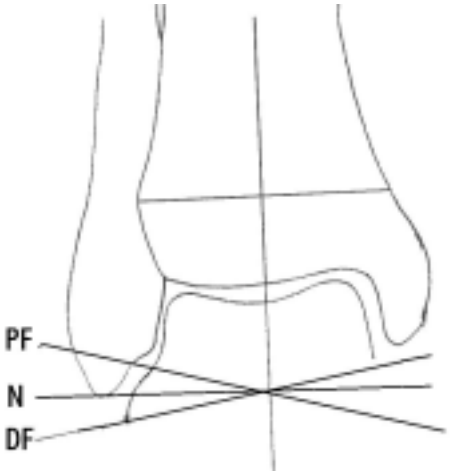

Figure 2.8 Three distinct ankle axes according to Barnett and Napier[35] and Hicks.[36] PF-plantarflexion, N-Neutral, DF-dorsiflexion. Adapted from Sarrafian[37]

Studies using more accurate techniques for tracking small movements in three dimensions[38-44] showed that the ankle joint axis changes continuously during movement. Lundberg et al.[41] analyzed the axes of eight subjects from 30° of dorsiflexion to 30° of plantarflexion in increments of 10°. The projection of the axis onto a frontal plane in neutral position was found to be just distal to the tips of the malleoli. This concurred with experiments by Inman.[19] The projected axis inclined upwards medially in dorsiflexion and upwards laterally in plantarflexion (Figure 2.9A). They noted, that while in some subjects the change of axes was gradual, in other subjects, there seemed to be two distinct axes, one in plantarflexion and one in dorsiflexion. These findings support the results of Barnett and Napier[35] and Hicks.[36] Furthermore, the axis in the transverse plane (Figure 2.6B) passed through the centers of the malleoli supporting experiments by Inman.[19] It should be noted that the axes from all experiments (dorsi/plantarflexion, supi/pronation

and ex/internal rotation) performed by Lundberg et al.[41-43] for any individual subject intersected in a small region of the trochlea. This small region seemed to create a hub around which the ankle joint had freedom to move. This could have an implication on the design of the talar component of an implant, especially a spherical type of an implant.

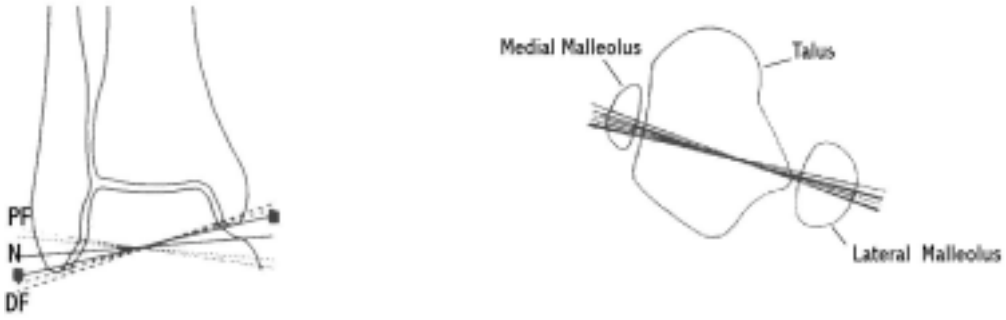

A B

Figure 2.9 Change of the ankle axis in ten increments of dorsi/plantaflexion according to Lundberg et al.[41] Projection of the axis onto A) transversal plane B) horizontal plane

A study by Leardini et al.[45] showed that in passive motion, the ankle joint motion was prescribed by both the articular surfaces and ligaments. They found a nearly isometric behavior of the most anterior fibers of calceneofibular (CaFi) and tibiocalceneal (TiCa) ligaments during flexion. Giannini et al.[26] stated, that in order to preserve the original kinematics after ankle arthroplasty, ankle implants had to either exactly replicate the original articulating surfaces (which none of the current prostheses do) or restore the function of the ligaments and the original kinematics. The latter case implied that the shape of an implant would be different from the shape of the original anatomical

articulating surfaces as long as the original kinematics were preserved. Leardini et al.[46] used a computer model to analyze shapes of ankle implants that would preserve original kinematics. For a two component design, the radii of the tibial component were set and the shape of the talar component was calculated satisfying CaFi and TiCa ligamentous isometry. The results showed that for tibial radii close to natural tibial arc radii (20-24mm), the radius of the talar component had to be slightly larger than the radius of the tibial component. This would create nonconformal surfaces and could increase wear.

2.4 Total Ankle Arthroplasty vs. Ankle Arthrodesis

Primary degenerative disease (primary osteoarthritis) of the ankle is relatively rare, compared to primary osteoarthritis of the knee and hip. Secondary osteoarthritis occurring in the ankle can be caused by many diseases such as rheumatoid arthritis, or by post traumatic arthrosis following ankle fractures and recurrent sprains[1] resulting in pain and decreased mobility. After nonsurgical procedures are exhausted and the patient's condition does not improve, several surgical options can be used.[1, 47] For the purpose of this work, only total ankle arthroplasty and ankle arthrodesis will be discussed.

The first total joint arthroplasty[48] is considered to be hip arthroplasty performed by Glück in 1890. Arthroplasty of the knee and shoulder followed shortly afterwards. It took almost 100 years until Buchholz (in the early 1970's) performed what is today considered to be the first total ankle arthroplasty.[1] Later, a modified version of this implant was used in Buchholz's own diseased ankle. In the mid-1970's, short-term reports on clinical performance of ankle implants showed promising results, with a success rate of 80% to 85%.[49] As a result, younger people active in outdoor activities

were included in the group of ankle implant recipients. However, five-year results revealed failure in 35% to 75% of cases and many surgeons concluded that total ankle arthroplasty should never be performed.[2] In 1998, Demetriades[47] stated that *"There also has been a report that showed little advantage, concerning pain relief and ankle motion, over ankle arthrodesis.[50] Because of these complications and the inability at present to show a significant advantage over other treatment modalities, most surgeons, with isolated exceptions, have abandoned the procedure."* It should be noted that any kind of generalization about the performance of an ankle implant depends on the particular implant used in the study. For example, a clinical study[51] of the Agility® ankle implant investigated in our study reported complete pain relief for 55% of patients and no case of severe pain. Currently, ankle implants are primarily used in older people. The advantages of ankle arthroplasty are substantial pain relief and retained mobility of patients. Potential disadvantages include aseptic loosening of the implants,[2, 4] subsidence of the implants into the cancellous bone,[25] and lateral talofibular joint impingement.[23] An ideal ankle arthroplasty would provide a pain-free ankle for normal daily activities, with at least 10 degrees of dorsiflexion and 20 degrees of plantarflexion.[1, 52] Minimal bone resection (for salvage arthrodesis) is required in case of failed ankle arthroplasty.[29] The implants must consist of biocompatible materials, should replace all three articulating surfaces of the ankle joint,[4] and must be inherently stable. According to Beuchel[25] *"the articulating surface geometry is the major inversion-eversion stabilizer with collateral ligaments playing an important secondary role."* The shape of the implant must reestablish the original kinematics; this will help ensure that the forces loading the

ankle after arthroplasty have the same direction and magnitude as in a healthy ankle.[4, 53] In order to eliminate loosening of implants, predominantly compressive stresses should be transferred to the bone eliminating shear and tensile stresses at the bone-implant interface.[25]

Ankle arthrodesis is a fusion of the ankle joint with removal of the articular surfaces. The first ankle arthrodesis was performed in 1878. Since then more than thirty different procedures have claimed to be optimal but none of them can guarantee successful results.[1] Ankle fusion is often performed when total ankle arthroplasty fails.[2, 29] Similar to ankle arthroplasty, ankle arthrodesis provides significant pain relief and stability of the ankle. The disadvantages of ankle arthrodesis are an unreliable fusion rate[1] and the long immobilization time required for fusion.[23] The decreased mobility results in limited ability to walk barefoot and on uneven surfaces. The fused ankle decreases supination by 50%[23] resulting in increased stresses in subtalar and midtarsal joints.[47, 54]

2.5 Ankle Joint Implants

Since no current ankle implant relies on hardware for physical connection, the stability of the ankle implant depends on two factors: the extrinsic stability provided by ligaments and the intrinsic stability provided by the design of the contacting surfaces of the implant. From the point of view of intrinsic stability, designs of the ankle implants can be divided into three categories according the amount of restriction on motion in planes other than the sagittal plane (plantar/dorsiflexion motion). The three categories are

referred to by some authors as constrained, semiconstrained, and nonconstrained (e.g. [1, 2, 53]), or as congruent, anatomic, and incongruent (e.g. [23, 25, 29]).

Constrained implants limit motion to the sagittal plane. They are typically spherical, spheroidal, conical, cylindrical or sliding-cylindrical in shape.[23] For example, one of the first clinically applied ankle implants was the Mayo[21] implant with long sliding cylindrical articular surfaces. The advantages of constrained implants are greater stability,[1, 25] elimination or minimization of impingement of the malleoli (distal ends of the tibia and fibula) against the talus,[1] and decreased wear of the UHMWPE insert because of larger contacting surfaces.[23, 25] A disadvantage of constrained implants is the transfer of greater torque into the bone-implant interface. During walking, the foot moves in the sagittal plane, frontal and transverse planes. As a result, torque is transferred to the bone-implant interface in constrained implants. This may result in aseptic loosening.[2, 23, 25] A study by Kitaoka et al.[55] on clinical performance of the Mayo constrained ankle implant used between 1974 and 1988 showed 61% failure rate after 15 years of in *vivo* use where failure rate was defined as the removal of the implant. Based on these results, constrained implants are no longer recommended.

Typical shapes of unconstrained implants are trochlear, bispherical, concave-convex, and convex-convex.[23] For example, in Irvin's[56] design, the spherical talar component articulates against a flat UHMWPE insert. Unconstrained implants tend to have a lower incidence of aseptic loosening but are unstable and incapable of transferring normal ankle loads.[25, 29] In addition, the wear characteristics of the UHMWPE insert

have been poor. Unconstrained designs have shown only slightly better short-term results than constrained designs.[26] No long-term results are published.[26]

Semi-constrained implants combine advantages of the constrained and unconstrained implants. They allow not only plantar/dorsiflexion motion but also some in/external rotation and lateral/medial motion. Giannini et al.[26] reviewed literature on all available ankle designs. From thirty-three original designs, only three are still in use: the Beuchel-Pappas Ultra Total Ankle (Endotec Inc., South Orange, NJ), the Scandinavian Total Ankle Replacement [STAR] (Linc Inc., Hamburg, Germany) and the Agility® (Depuy, Warsaw, Indiana) all belonging to the group of semi-constrained implants. Short-term clinical results are more encouraging than the results from earlier designs. However, the long-term results have yet to be determined.

The Agility® implant used in the current study is called a two component design because of two articular surfaces.[1, 26, 28] It consists of three parts: the metal talar component, the tibial metal tray, and the UHMWPE tibial insert. The UHMWPE insert and the talar component are counterformal cylinders. The original talar component of the Agility® implant, referred in our study as "Standard", is narrower than a talar component of similar constrained implants. It tapers posteriorly to mimic the natural shape of the talus. This shape permits internal/external rotation and iversion/inversion. The distal tibial and fibular fusion provides more space for the tibial tray and incorporates the fibula into weight bearing. The fusion is promoted by two titanium screws and no cement is used for implantation. The design relies on bony in-growth on the porous surfaces of the implants. At this time (3/1/2002) there is only one study of clinical results of the Agility®

implant available in the literature.[51] In eighty-five ankles available for the study there were two fractures of the tibial implant. Since the thickness of the tibial tray was increased in 1989, no fracture of the tibial tray has occurred. Radiolucent lines of up to two millimeters were found around the implants but did not progress after two years. Migration of the tibial and talar components was also measured and defined as five degrees of tilt which is the minimum that can be reliably detected. Seven talar components migrated with no association with a delayed union or non-union of the tibia-fibular syndesmosis. On the other hand, eight of twelve migrated tibial components were associated with a delayed union or non-union of the tibia-fibular syndesmosis.

2.6 Structure and Mechanical Properties of Bone

Bone is an anisotropic, heterogeneous and viscoelastic material. It provides support for the body against gravity, serves as a lever system for muscles, and protects internal organs.[57] Depending on shape, bone can be divided into three groups: long, short, and flat. In the leg and foot, only long and short bones are present. There are two kinds of bone: cortical (compact) and cancellous (trabecular, spongy), both of which are present in the ankle.

2.6.1 Cancellous and Cortical Bone

Cancellous bone is porous, composed of a network of trabecular plates and struts filled with fatty viscous fluid called marrow.[58] Cortical bone is dense, composed of regular, cylindrically shaped lamellae creating Haversian systems. The transition between these two forms of bone tissue is continuous with no clear border between

porous cortical bone and dense cancellous bone.[58] In 1892, Wolff[59] published a paper in which he postulated his "law of bone transformation" which is today called "Wolff's law". He stated that the cortical bone was nothing other than compressed cancellous bone. As a mathematical proof, he compared the density and distribution of principal stress trajectories of a crane to the structure of the cancellous bone in the proximal femur. He found that the trajectories of principal stresses were concentrated on the periphery of the crane, suggesting that cancellous bone transformed into cortical bone under the influence of high stresses. Moreover, he found overall visual correspondence between principal stress trajectories and the orientation of trabeculae of cancellous bone. He especially pointed out the 90-degree intersection of trabecular struts. Since then, numerous research studies have tried to prove or disapprove the validity of "Wolff's law" based on measurements of mechanical properties of cortical cone and individual trabecular struts. Some researchers support[60-64] the statement that the cortical and cancellous bone are made of the same material while others disagree with it.[65-67] A recent study by Pidaparti[68] showed that a nonorthogonal (60-degree) trabecular orientation reduced shear under multiaxial loading as seen in sinovial joints. This orientation of trabecular struts was observed in the greater trochanter of femur. According to Pidaparti, an orthogonal trabecular orientation minimized shear coupling under uniaxial loading in places such as tendon insertion.

Cancellous bone can be described in terms of structural and material properties. Structural properties are extrinsic properties of both the trabeculae and cavities and are important for global stress analysis at the macroscopic level. Measurements of structural

properties will be discussed in more detail in Section 5.4. Material properties are defined as intrinsic properties of the trabecular struts only.[58] A literature survey carried out by Rho et al.[67] showed that measurements of intrinsic Young's modulus of the trabeculae range from 0.76-20 GPa, possibly due to difficulties in preparing samples. This is in contrast with Young's moduli for cortical bone which are reported to be in a 20-22 GPa range along longitudinal axis of the long bone and 12-14 GPa transversely.[61] The intrinsic material properties can be used for microstructual stress analysis and estimation of bone adaptation at the implant-bone interface. However, at present, there is no experimental method capable of verifying stress/strain results at the microscopic level. The majority of microscopic level models have been verified against globally observed failure.[64, 69, 70]

2.6.2 Long and Short Bone

A long bone is distinguished by the presence of one much larger dimension. The fibula and the tibia belong to this group. The diaphysis or shaft corresponds to the large dimension of the long bone, expands into the metaphysis and ends with an epiphysis at both extremities (Figure 2.10).

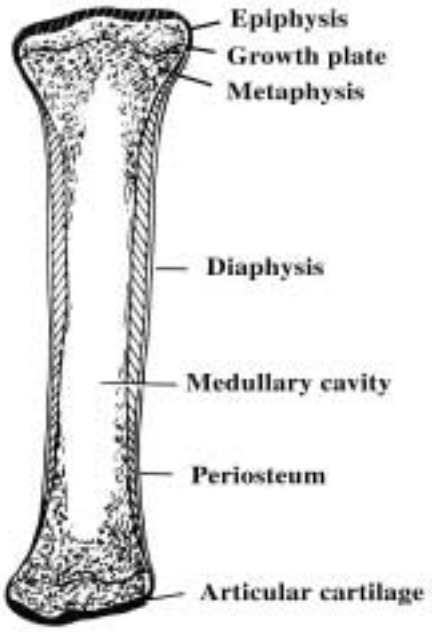

Figure 2.10 Structure of the long bone[71]

The articulating portions of the epiphysis are covered with cartilage, which has a coefficient of friction as low as μ=0.0026.[71] Except for the cartilage, the outside of the long bone is covered with a very thin layer of periosteum. The periosteum is responsible for circumferential remodeling of immature bone and for healing of injured bone.[72] Beneath the periosteum is cortical bone. Cortical bone is very thick in the diaphysis but becomes very thin in the metaphysis and epiphysis. The thick cortical bone of the diaphysis of the long bone has Haversian systems oriented predominantly in the longitudinal direction.[73] This orientation, along with the shape of the shaft's cross section, provides resistance to torsion, bending, and compression.[74] The medullary cavity of the diaphysis is filled with marrow, which contains a source of bone cells and

blood vessels. The epiphysis and methaphysis are filled with cancellous bone. The cancellous bone and the thinner cortical bone of the epiphysis and methaphysis allow deformation and dampen impact loading. Thus, resecting a portion of the epiphysis for insertion of implants reduces the capacity for absorption of impact and increases the force transmitted to the joints.[74]

Short bones are approximately equal in all dimensions. The talus is a short bone. Its main feature is a very thin shell of cortical bone surrounding cancellous bone. In the vicinity of the articular surfaces, the cortical bone is thicker[4] and plates of cancellous bone orient themselves to support the transmitted load.[22, 75] The same phenomenon can be observed in the metaphysis and diaphysis of a long bone. This is in accordance with Wolff's law and accounts for anisotropic, heterogeneous material properties.

2.6.3 Mechanical Properties of Cancellous Bone

Our FEM study is performed on the macroscopic level. Therefore, we need structural properties of cancellous bone that are combination of properties of trabecular struts and cavities filled with marrow. Bone provides structural support and, from this functional[76] standpoint, the compressive strength of the bone is superior to the tensile strength. Tensile loads are present in places such as ligament and tendon insertions, and in places of the bone that are loaded in bending and torsion. In the ankle joint during normal walking, the bone is loaded predominantly in compression. The shear strength may also play a significant role in fracture of cancellous bone during traumatic loads

which are not aligned with load during normal walking[77]. It will also be important at the bone-implant interface.[78, 79]

Measurements of mechanical properties of cancellous bone have shown scatter in the results similar to the measurements of intrinsic properties of trabecular struts mentioned in Section 2.6.1. These variations are caused by differences in anatomic position, load direction and sample preparation technique[80]. The three major potential limitations[81] in compressive tests are compliance of the testing machine, friction with the test platens and structural end-phenomena occurring when trabeculae nearest to the free surface become unstable. Tests characterizing shear and tensile properties of cancellous bone are even more demanding and only a few studies can be found in the literature.[80]

Experiments have demonstrated that the tensile and compressive Young's moduli of cancellous bone[82] are the same. Studies comparing the tensile and compressive strengths can be divided into three groups: a group that found the strengths to be equal,[83, 84] a group that found the tensile strength to be lower[85] and a group claiming that the tensile strength is higher[82] than the compressive strength. Keaveny et al.[86] developed a testing method that eliminated end artifacts and friction at the specimen-platen interface. Experiments on bovine cancellous bone[62] showed asymmetry in tensile and compressive yield strength, with the tensile strength thirty percent lower than the compressive strength. However, the difference between the tensile and compressive strengths increased with an increasing apparent density of cancellous bone, but with no difference at low densities. In contrast, even though asymmetric, both the compressive and the

tensile yield strains were homogeneous (independent of apparent density). The definition of yield and ultimate strains as used in the experiments is shown in Figure 2.11.

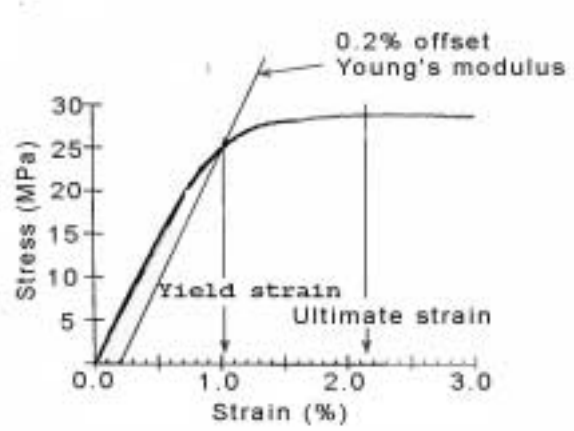

Figure 2.11 Definition of the cancellous bone failure parameters as used in Keaveny's[62] experiments. The ultimate strain was calculated as the lowest strain that occurred for the maximum stress

Keaveny et al.[87, 88] suggested that yield strain might be better a failure criteria than yield stress since it was homogeneous and therefore independent of the location of the bone. Moreover, they postulated that failure strains of cancellous bone are isotropic (independent of loading direction and trabecular orientation) supporting the findings of Turner.[89, 90] It should be emphasized that both groups performed experiments on bovine bone, which is more dense and uniform than human cancellous bone. Experiments by Kopperdahl and Keaveny[91] on human vertebral cancellous bone found compressive yield strains to be somewhat dependent on apparent density and anatomic location and tensile yield strains to be independent of both the apparent density and anatomic location.

Results also demonstrated that over a narrow range of high densities yield strains could be assumed to be constant. The latest study on dependence of yield strain of human cancellous bone on anatomic location by Morgan and Keavany[92] showed that the yield strain in both compression and tension differed between the anatomic locations but could be considered uniform within each location. The differences of yield strain across the location were small, at most twenty percent (Table 1), while the yield stress and modulus differed by a factor of eight and ten respectively. They concluded that inter-location differences are not due to testing or anisotropy artifacts as previously thought. They recommended using yield criteria, whether based on stress or strain, that would be specific to the anatomic location. It should be pointed out that all the tests by Keavany et al. were performed along the direction of the principal axis of cancellous bone and therefore, the results provided no information for different loading directions.

Fenech and Keaveny[93] showed that for uniaxial tensile or compressive load coupled with torsional loading around the same direction, minimum principal strain criterion accurately predicted failure in tension, but was less accurate in compression. In addition, experimental and finite element studies by Lotz et al.[94] and Silva et al.[95] found cancellous bone failure criteria based on strains to be more successful than failure criteria based on stress (more in Section 3.1.3). In contrast, a study by Keyak et al.[96] without experimental confirmation showed that strain-based failure theories performed more poorly.

Shear failure tests of cancellous bovine bone by Ford and Keaveny[79] showed that the ultimate and yield stresses depended on apparent densities while the ultimate and

yield strain were constant. Based on these results, they suggested that the mean failure strain values might be extrapolated to low density human bone.

Table 1 Mechanical properties of cancellous bone

Reference	Bone	ε_y (%)	ε_u (%)	E (MPa)*
Compression				
-Keaveny[62]	Bovine tibia	1.08	1.86	2380
-Morgan[92]	Human tibia	0.73	NR	1091
-Morgan[92]	Great. Trochanter	0.70	NR	622
-Morgan[92]	Human Vertebra	0.77	NR	344
-Morgan[92]	Femoral neck	0.83	NR	3230
-Fyhrie[97]	Human Vertebra	0.67	1.5	500
-Kopperdahl[91]	Human Vertebra	0.81	1.45	219
-Linde[81]	Knee	NR	2.0	408
Tension				
-Keaveny[62]	Bovine tibia	0.78	1.37	2630
-Morgan[92]	Human tibia	0.65	NR	1068
-Morgan[92]	Great. Trochanter	0.61	NR	597
-Morgan[92]	Human Vertebra	0.70	NR	349
-Kopperdahl[91]	Human Vertebra	0.78	1.59	301
Shear				
-Ford[79]	Bovina Tibia	1.35	4.24	G=349

*Average Young's modulus

It has been demonstrated that the post-yield behavior of cancellous bone is asymmetric, with different behavior in tension and compression.[62, 98, 99] In tension, cancellous bone fails in an almost brittle manner with little post-yield resistance against load (Figure 2.12). In compression, cancellous bone fails with pronounced strain softening and crushing.

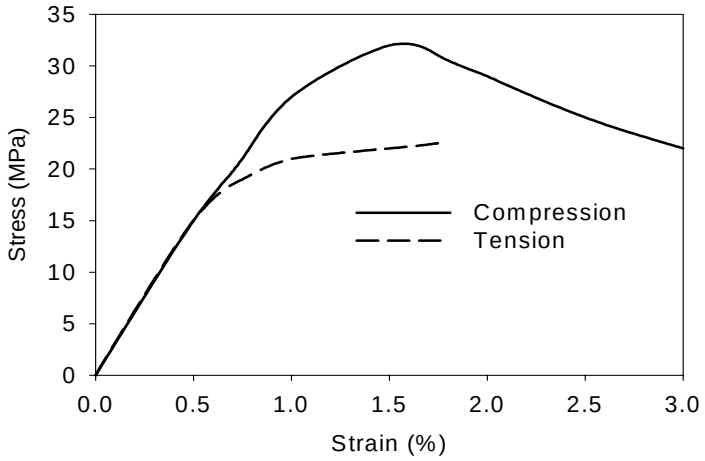

Figure 2.12 Typical stress-strain curve in tension and compression for cancellous bone (adapted from Keaveny et al.[62])

In summary, the mechanical properties of cancellous bone show:

- The same tensile and compressive Young's moduli

- Asymmetric yield strengths and strongly dependency on density

- Asymmetric yield strains with no dependency on density and loading direction

- Yield strains constant between anatomic locations

- Asymmetric post-yield behavior with brittle fracture in tension and strain softening in compression

2.6.3.1 Spatial Variation of Mechanical Properties in the Bones of the Ankle Joint

Studies by Jensen et al.[100] and Hvid et al.[101] measured spatial variation of mechanical properties of cancellous bone of the talus and the distal tibia. The two studies differed on the absolute values, but agreed on the pattern of distribution of the properties. The distal end of the tibia and the proximal half of the talus proved to be stronger antero-laterally (Figure 2.13), and the strength decreased with increasing distance from the ankle. This implied that the resection of more bone for an implant reduced the load that could be carried by the remaining bone. Jensen's[100] tests showed that the cancellous bone of the talus is 40% stronger than the cancellous bone in the distal tibia. Thus, a talar component with the same bone-implant interface area as a tibial implant would more readily resist the loads in the ankle joint.

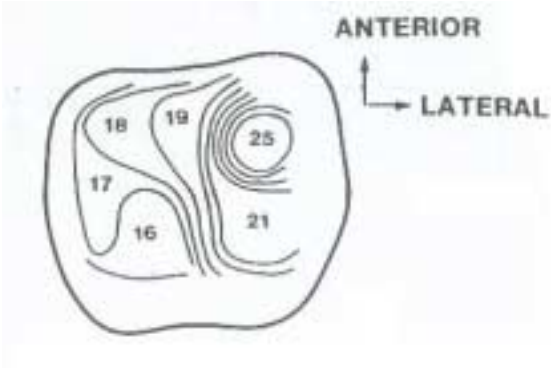

Figure 2.13 Mean ultimate strength profiles of the talus representing first 6 mm beneath the dome of the talus. Units in MPa[100]

The tests by Jensen et al.[100] were performed with specimens of 7.5 mm in diameter and 6 mm in depth. Linde et al.[81] proposed that such specimens are prone to structural end phenomenon (see Section 2.6.3) and would underestimate stiffness by 20-40 percent compared to specimens surrounded by bone.

2.6.3.2 Fatigue Strength of Cancellous Bone

Fatigue failure can occur at stress levels considerably lower than the static strength. Even though the fatigue failure of bone is not well understood, it is known to resemble the fatigue failure of composite materials in which a gradual loss of stiffness and strength occur over the loading period.[102] It is also well known that fatigue creates microfractures in cancellous bone[103] and it has been hypothesized that these microfractures trigger a remodeling response.[104] If the damage by microfracture exceeds the repair by remodeling, the bone will fracture, or as in case of implants, the implant will subside into cancellous bone.

While there have been many studies of the fatigue behavior of cortical bone (see, for example Caler and Carter[105]) only a few studies examined fatigue behavior of cancellous bone. Experiments by Choi and Goldstein[102] suggested that the fatigue strength of trabecular tissue (the intrinsic property of cancellous bone) was lower than the fatigue strength of cortical bone tissue. For our macroscopic level FEM study, the fatigue strength of cancellous bone is more important. Kempson[32] estimated, without experimental evidence, that the fatigue strength of cancellous bone was one third of the ultimate compressive strength. Since then, some studies[101, 106] used it as a "rule of thumb" for predicting implant subsidence. Similarity in fatigue behaviour between

cancellous and cortical bone was reported by Michel et al.[107] The results showed that the fatigue life was strongly dependent on the magnitude of the maximum strain applied in first cycle (Figure 2.14). Bovine cancellous bone failed in cyclic loading at loads below the yield strength. For a lifetime of one million cycles, one can estimate a failure strain of 1% which is approximately 40% of the original ultimate compressive yield of the study. It was hypothesized that cancellous bone at low cycle, high initial stress, will fail by creep and at high cycle, low initial strain, will fail by microcracking. In any *in vitro* study in general, the remodeling process that would accompany damage accumulation *in vivo* is not present. Moreover, all studies of fatigue properties of cancellous bone have been conducted with bovine bone which is more dense and structurally different than human cancellous bone.

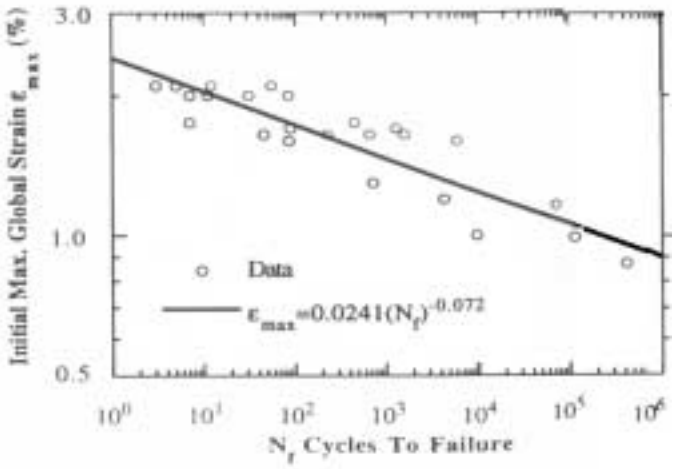

Figure 2.14 Fatigue curve for bovine cancellous bone[107]

2.6.4 Mechanical Properties of Cortical Bone

The study of static mechanical properties of human cortical bone by Reilly and Burstein[108] has been used as a reference in many papers. The experiments were carried out on diaphyseal cortical bone. As with cancellous bone, the tensile and compressive Young's moduli were shown to be the same while ultimate strengths were asymmetric. The mechanical properties are listed in Table 2

Table 2 Mechanical properties of diaphyseal cortical bone from experiments by Reilly and Burstein[108]

Mechanical property	Longitudinal	Transverse
E (MPa)	17,000	11,500
Ultimate strength (MPa)	133^{t}, 193^{c}	51^{t}, 133^{c}
Ultimate strain	3.1%	0.7%

t-tension

c-compression

The post-yield behavior of cortical bone (Figure 2.15) is also asymmetric. In tension, the behavior can be modeled as bilinear with a post-yield modulus of approximately E=0.8 GPa.[108] In compression, cortical bone behaves like an elasto-perfectly-plastic material.

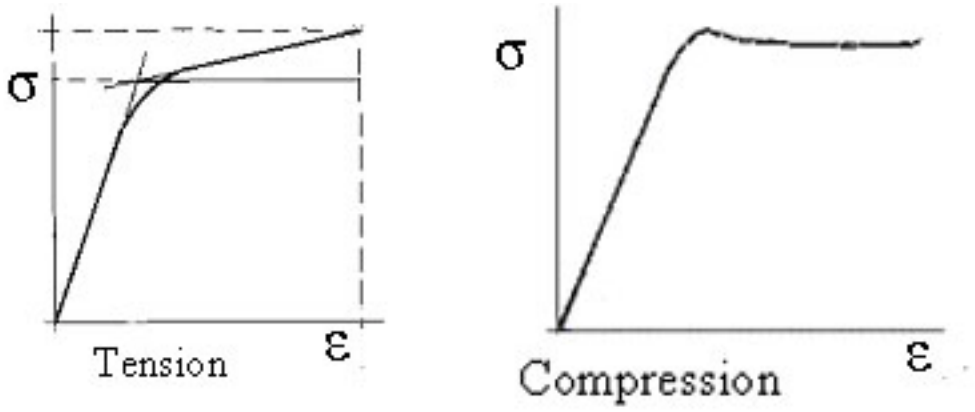

Figure 2.15 Stress-strain curve in tension and compression for cortical bone[108]

The material properties of thin metaphyseal cortical shells were investigated by Lotz et al.[109] who found a moderate decrease in mechanical properties compared to cortical diaphyseal bone. The difference between the metaphyseal and the diaphyseal bone was attributed to lower density of the mataphyseal bone. The material properties are listed in Table 3.

Table 3 Mechanical properties of metaphyseal cortical bone from experiments by Lotz et al.[109]

Mechanical property	Longitudinal	Transverse
E (MPa)	9,650	5,470
Ultimate strength (MPa)	100	50

3.0 LITERATURE REVIEW

The amount of published work found on the ankle arthroplasty reflects the fact that ankle arthroplasty is relatively new and less common than hip or knee arthroplasty. All known FEM models of the ankle joint and features from other models relevant to our study of stresses and strain of bones are discussed in Section 3.1. Loads carried by the ankle, necessary for FEM boundary conditions, are addressed in Section 3.2. The load carried by the fibula will be discussed in Section 3.3 and some aspects of UHMWPE including selected FEM simulations modeling stresses in the UHMWPE inserts are discussed in Section 3.4. Finally, analytical solutions for conformal cylindrical surfaces will be discussed in Section 3.6.

3.1 FEM Models Calculating Stresses and Strains in Bones

Compared to the number of FEM studies on prosthetic hip and knee, FEM calculations of a prosthetic ankle are few in number. For completeness, findings from some hip and knee models and models containing the intact ankle relevant to investigation of prosthetic ankle are included in the literature review.

3.1.1 Three-Dimensional FEM Models of Ankle Joint

The first FEM model of ankle joint bones found in the literature dates to 1983 and is three-dimensional. Calderale et al.[4] created two models, one for the talus and one for the tibia with implant. The two models were run separately under different loading conditions. The cortical bone of the talus was modeled with shell elements. They found

that the load applied on the top of the talar trochlea caused peak stresses only twenty per cent higher than average stresses. This confirmed their assumption that intact bone will distribute stresses evenly throughout the bone. Upon resection of the top of the talus, the stresses increased near the resected area. The directions of stresses on the resected areas of the talus indicated that the talar bone was displaced. They concluded that an ideal prosthesis should not disturb the natural distribution of stresses. The tibial model was loaded medial-laterally rather than along the longitudinal axis. They did not comment on this choice of loading and did not discuss the results. They stated, however, that the best design would include a long stem for the transfer of loads to the mid-diaphysis of the tibia. This conclusion followed from the fact that cancellous bone in the distal tibia is weak and cortical bone, once stripped of the cartilage, is weakened and tends to split.

Crowell[3] calculated stresses in the distal tibia and the tibial component of an implant. A compressive load of 3,430 N, the ankle force that a 70 kg person would experience during a normal walking cycle with a pain free ankle (five times body weight, Figure 3.4, page 45), was applied to the flat plate of the tibial component of the implant as a uniformly distributed pressure of 4.1 MPa. He found, that the von Mises stress in the bone was below the ultimate compressive strength of the bone and the stress in the implant was below the fatigue strength of the implant alloy. The smooth bone-implant interface was modeled with gap elements thus transferring only compressive loads while the porous bone-implant interface was modeled with spring elements. After several iterations, all spring elements with tensile stresses were changed to gap elements because bone ingrowth does not occur due to tensile stresses.[110] The Young's modulus of

cancellous and cortical bone of the tibia in the model decreased proximally. Since, at the time of the analysis, values of the Young's modulus of the distal tibia were not available, he chose material properties of the distal tibia to be between the values for femoral head reported by Brown and Fergusson[111] and the values for the proximal tibia given by Goldstein et al.[112] "*Because the contact area at the ankle is greater than the contact area at the hip and less than the contact area at the knee, it is reasonable to assume that the values of elastic modulus would be between the values reported for the femoral head and the proximal tibia*" was used to justify the choice of the material properties of the distal tibia. However, a comparison of material properties of different joints based on cross-sectional areas assumed that the forces transferred through the joints were equal. This is apparently not the case, because the ankle joint transfers higher loads than either the hip or knee.

Falsig et al.[5] created a model of the distal tibia with three implant designs: a polyethylene block not backed by metal, a polyethylene block backed by metal and a prosthesis with a long stem. The material properties of the cancellous bone were modeled as either homogeneous or heterogeneous. A modified von Mises criteria was used as a failure criteria in which three modes of failure were combined (compression, tension, shear). Since bone has a different strength in compression than in tension, this criterion might be useful for predicting failure of the bone in areas where tension and shear are not negligible, i.e. areas of bone further away from the joint and at the bone-implant interface. A single force of 2,100 N (three times 70 kg body weight) was applied to the articular surface of the tibial component of the implant. The results showed that a metal

backed polyethylene model would probably fail although it lowered compressive stresses compared to the nonbacked model. The stresses in the long stem bypassed the trabecular bone of the metaphysis, which would be equally unfavorable for the bone as high stresses and cause resorption. They therefore recommended a shorter stem. The model with heterogeneous material properties resulted in lower more evenly distributed stresses in the bone.

Genda et al.[8 1999] constructed a model of 14 bones and 59 ligaments of the foot to study load transmission in the foot. They used Rigid Body Spring Modeling, in which bones were modeled as rigid bodies and ligaments were represented by springs. Contact surfaces were created between rigid bodies of the bones to transfer loads. For example, the results showed that the subtalar joint and talonavicular joints transmitted 62% and 38% of the load respectively.

Ledoux et al.[13] created a model from 286 CT scan slices consisting of 26 bones including the distal tibia and fibula, 51 ligaments and plantar soft tissue. The 3-D cartilage (articular) surfaces were created separately and attached to the volumes of the bones. Eigenvectors of principal moments of inertia were used to describe the relative position and angles of the bones of the foot. However no stress analysis was completed.

Other areas of ankle research concentrated on ankle injuries in car crashes[11, 12, 14] and stress analysis of ankle-foot orthosis.[113] They did not add information pertaining to our model and will not be reviewed.

3.1.2 Two-Dimensional FEM Models of Ankle

Oonishi et al.[7] carried out a stress analysis for an intact and prosthetic ankle joint under various types of loadings. They found similar distributions of principal stresses in the bones under a vertical load in both cases.

Lewis and Austin[6] performed a comparative stress analysis of the ankle in neutral position with and without an implant and reported an experimental fatigue strength of the cancellous bone. The load used in the study was 2,590 N which was considered to be the load that a person of 80 kg would experience postoperatively during a normal walking cycle (3.3 times body weight, Figure 3.4, page 45). The strength of the implant was found to be adequate for the loads experienced during normal walking (more in Section 3.5). They reported a change in the magnitude of stresses in both the cortical and the cancellous bone after implantation of a prosthesis. They compared the first principal stress, which is usually tensile, to the ultimate compressive strength of the bone. In addition, the reported fatigue strength of the cancellous bone from the experiments was higher than the ultimate compressive strength, which is physically impossible.

DeGioia[9 1992] used two models, one of the sagittal plane and one of the frontal plane, to calculate contact stresses in the ankle joint. The highest contact stress was located on the medial and anterior portions of the tibiotalar articulating surfaces. The fibula was found to carry between 6-16% of the load.

Giddings et al.[10] developed a FEM model of the foot that included some ligaments and the plantar fascia. The study aimed to create a model of the calcaneus without knowledge of the applied loads and joint pressures. The load was applied at the

base of calcaneus and at the metatarsal heads based on ground reaction force experiments and the analysis was carried out in discrete increments of 20% of the stance phase of walking and running. In the calcaneus, they visually verified the trajectories of principal stresses with orientation of trabeculae and found good correspondence. Even though there were variations in stress magnitudes for running and walking, the directions of principal stresses were unchanged. The predicted contact forces in the talocalceneal joint were 5.4 times body weight for walking and 7.9 times body weight for running.

3.1.3 Other FEM Models

Due to the limited number of FEM models of ankle and prosthetic ankle, the scope of literature was widened to include FEM studies of prosthetic hip and knee with direct implications to our model. The focus was to review FEM models comparing computational predictions with either clinical or experimental data.

Cheal et al.[114] studied the influence of the position of a tibial tray of a knee implant on stresses in the cancellous bone. They found that an implant without cortical bone contact produced only slightly higher stresses than an implant resting on cortical bone. Moreover, an undersized implant could lead to resorption of the adjacent unloaded cortical bone.

Taylor et al.[106] developed a FEM model of the femur assigning elastic-perfectly plastic material properties to cancellous bone . Plasticity occurred when compressive stresses reached ultimate compressive strength which was expressed as a function of Young's modulus. They found a relationship between the stresses in cancellous bone and

the subsidence rate of some types of femoral implants after two years of clinical use. Since subsidence is related to aseptic loosening, they stated that the initial stresses in the cancellous bone could be used to predict clinical performance of an implant. In addition, they experimented with a lower Young's modulus of cancellous bone to simulate material properties of a diseased bone. They found that the reduction of the Young's modulus did not alter the distribution of stresses, but did lower the threshold level at which failure occurred.

Ford et al.[77] investigated the fracture risk of the femur. The material properties of the bone were isotropic and non-homogeneous based on density data measured by quantitative computed tomography (QCT). The materials were modeled as elasto-perfectly plastic. To account for asymmetric tensile and compressive strengths, the model was first run with linear material properties. Elements with the larger tensile principal stress were assigned strength based on 0.8% yield strain (see Table 1). Elements with largest compressive stresses were assigned strength based on 1% yield strain. This resulted in maximum values of 144 and 180 MPa for tension and compression, respectively, which compared well with Reilly's[108] experiments (see Section 2.6.4). Failure was defined as 3% tensile strain in cortical bone. Even though the results predicted trends similar to experiments, the overall strength of the femur was underpredicted by 100%.

Lotz et al. tested the correspondence between linear[98] and nonlinear[94] FEM models and in vitro strain gage data of femur. The material properties of cortical bone in both models were anisotropic and homogeneous and divided to three regions: diaphyseal,

metaphyseal and a so called “reduced” zone. The reduced zone was a region where elements were too thick to model as a thin cortical shell. The material properties in this zone were reduced to one third of the metaphyseal material properties. The cancellous bone material properties were based on QCT measurements arranged in 10 groups in increments of density. In the nonlinear model, cortical bone was represented as an isotropic bilinear material with a reduced post-yield modulus. Cancellous bone was represented by a material law originally developed for concrete which could model brittle post-yield behavior in tension and strain softening and crushing in compression (Section 2.6.3). The results of the linear model predicted yield and ultimate behavior well. However, the results of surface stresses correlated poorly with strain gage data. The best correspondence was achieved with the calculated von Mises strain which was within 8% of the experimental results. The nonlinear model provided more detailed information about events leading to fracture. However, the nonlinear analysis only performed as well as the linear analysis for prediction of bone fracture. They suggested the use of linear analysis with strain based failure criteria.

3.2 Forces Loading the Ankle

Forces transmitted across the ankle joint are a combination of external and internal forces. The external forces are the forces produced by the body contacting the ground. These ground reaction forces (GRF) can be measured experimentally during gait using a force platform. An example of a GRF measurement performed by Giddings et al.[10] (Figure 3.1) showed that a person during walking will develop a compressive GRF of 1.2 times body weight (bw).

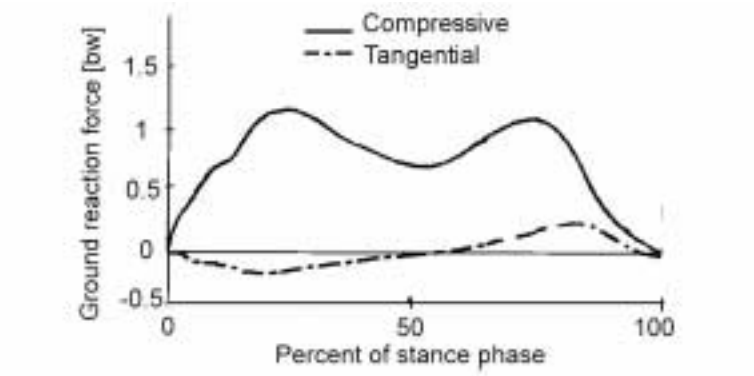

Figure 3.1 Experimentally measured compressive and tangential ground reaction forces by Giddings[10]

The internal forces are produced by muscles and ligaments and multiply the external forces. These internal forces are not completely understood. Their *in vivo* determination is difficult and, therefore, all reviewed work on the determination of internal forces in the ankle is based on computational methods.

A force analysis based on a simplified model of ankle joint on Figure 3.2 can illuminate the multiplication phenomenon of the internal forces. The foot in this example is in contact with the ground with the heel is slightly raised, transferring 1.2 times bw to the metatarsal bones. This load must be equilibrated by the Achilles tendon. For a typical ratio a/b=0.5, the Achilles tendon must exert force of 2.4 times bw which leads to an ankle joint reaction force of 3.6 times bw.

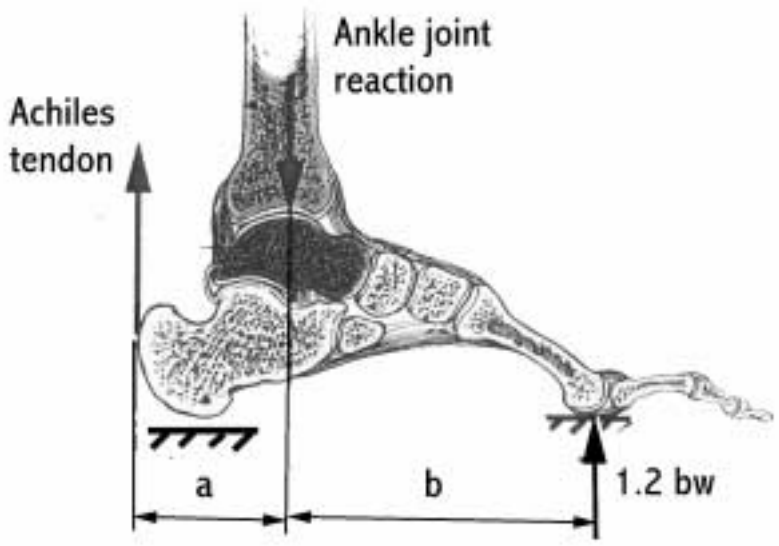

Figure 3.2 The foot in contact with the ground with the heal raised slightly

Numerous biomechanical models have been developed to calculate internal forces in the muscles and joints of the foot.[10, 21, 115-117] All, but the model developed by Seireg and Arkvikar, use GRF as the input for their model, as in the simplified model on Figure 3.2. Seireg and Arkvikar[115] created a three-dimensional model of the lower extremity. The load was applied to each foot from above and varied from zero at heel strike to 1 times bw at the beginning of one-legged stance. The calculated maximum compressive force (force in Z direction) was 5.2 times bw (Figure 3.3). The maximum anterior-posterior tangential force (force in X direction) was two times bw and the medial-lateral tangential force (force in Y direction) was one times bw.

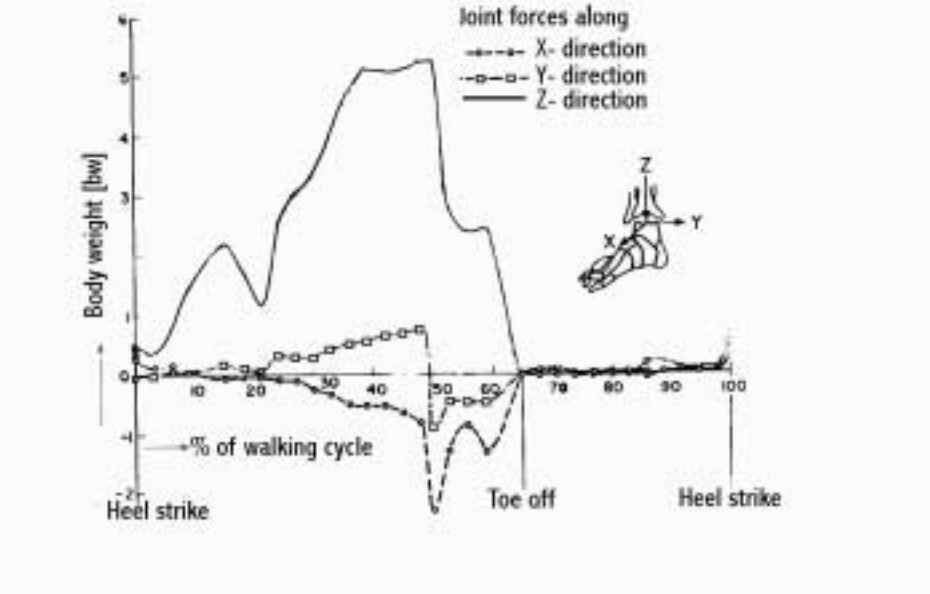

Figure 3.3 Components of reaction forces at the ankle joint as determined by Seireg and Arkvikar[115]

Staufer et al.[21] developed a two-dimensional model of an ankle joint in the sagittal plane. They studied reaction forces in the ankle in a group of normal subjects and patients with disabled ankle joints before and after TAA. They found that during the stance phase of gait, the maximum compressive force developed in the ankle joint was five times body weight for normal uninjured people (Figure 3.4). Prior to ankle arthroplasty, the maximum compressive force in the ankle joint was three times body weight and did not increase significantly at one year postoperatively, even among people reporting good surgical results. Moreover, postoperatively, the anterior-posterior tangential forces reached only one half of the original preoperative value of 0.8 times bw.

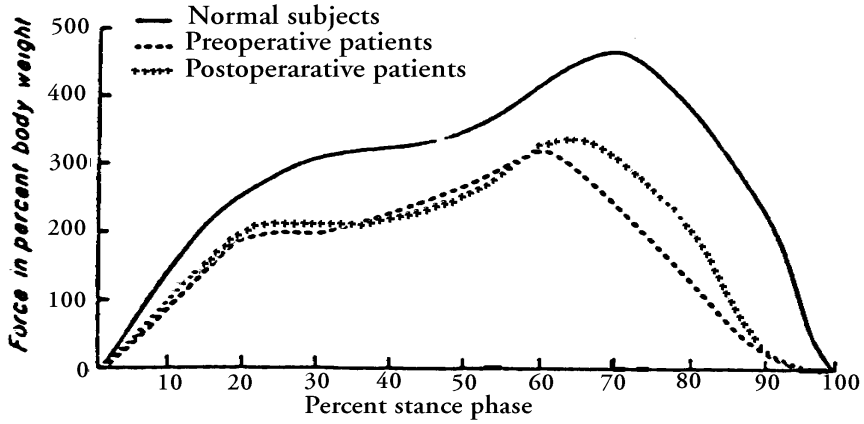

Figure 3.4 Compressive force at the ankle joint during stance phase of gait (Stauffer [21])

Procter and Paul[116], using a three dimensional analysis, determined the average maximum compressive forces in the ankle joint to be 3.9 times bw. They also reported a maximum of 40 N·m torque due to in/external rotation of the foot.

Komistek et al.[117] calculated reaction forces in the ankle joint using Kane's method of. They found maximum ankle joint reaction forces of only 1.3 times bw. It should be noted that the shape of the curve of the reaction forces more closely resembled the shape of ground reaction forces (Figure 3.1) than a shape of reaction forces of the ankle obtained from other models (Figure 3.3 and Figure 3.4).

A finite element study by Giddings et al.[10] (described in Section 3.1.2) showed that the contact, and thus compressive, forces in the talocalceneal joint reached 5.4 times bw. The model did not include the talotibial joint (the actual ankle joint), but similar compressive loads can be expected in that joint because of their proximity and because of similar orientation with respect to the load.

3.3 Load Bearing Capacity of the Fibula

Until the early 1970's it was generally believed that all load on the foot was transferred through the tibiotalar articulation. The fibula was believed only to stabilize the ankle. In 1971, Lambert[118] measured the load carrying capacity of the fibula using strain gages (SG). He determined that the fibula carried one sixth (17%) of the total load (Table 4). Takebe[119] however, claimed that 17% percent was an overestimation. He measured the weight-bearing of the fibula by a direct method of inserting force transducers (FT) into the resected portions of the two bones. His results showed that the fibula carried only 6.4% of the total load.

Table 4 Weight-bearing capacity of the fibula as a percentage of the total load

Data from [118-121]

Property	Lambert	Wang	Takebe	Goh
Applied load (kg)	68	60**	60	235
Method	SG	SG	FT	FT
Normal position	17%	11%	6.4%	7.12%
Plantarflexion	N.A.	N.A.	2.3% (15º)*	4% (40º)*
Dorsiflexion	N.A.	23% (15º)*	10.4% (15º)*	11% (25º)*
Inversion	N.A.	5% (10º)*	2.4% (N.A.)*	3.7% ("full")*
Eversion	N.A.	17% (10º)*	10.4% (N.A.)*	13% ("full")*

SG- Strain gage
FT- Force transducer

* The angle of position at which the values were obtained.
** The weight-bearing values linearly interpolated between the given data.

Two more reports on the weight-bearing of the fibula were be found[120, 121] and are arranged into Table 4 together with the experiments of Lambert and Takebe. The SG method gives consistently higher measured results than the FT method. From Table 4, it can also be seen that the fibula carries more load in dorsiflexion and eversion and less load in plantarflexion and inversion than in the neutral position.

The results of Wang et al.[121] showed that a higher portion of the load is carried by the fibula when higher the loads are transmitted through the leg (Figure 3.5). Moreover, when the tibia and fibula were connected proximally and distally screws, the percentage of the load carried by the fibula in the neutral position increased from 17% to 25% (at the 1500 N load, Figure 3.5). This could have an implication for loading conditions in our model because of the tibio-fibular syndesmosis fusion.

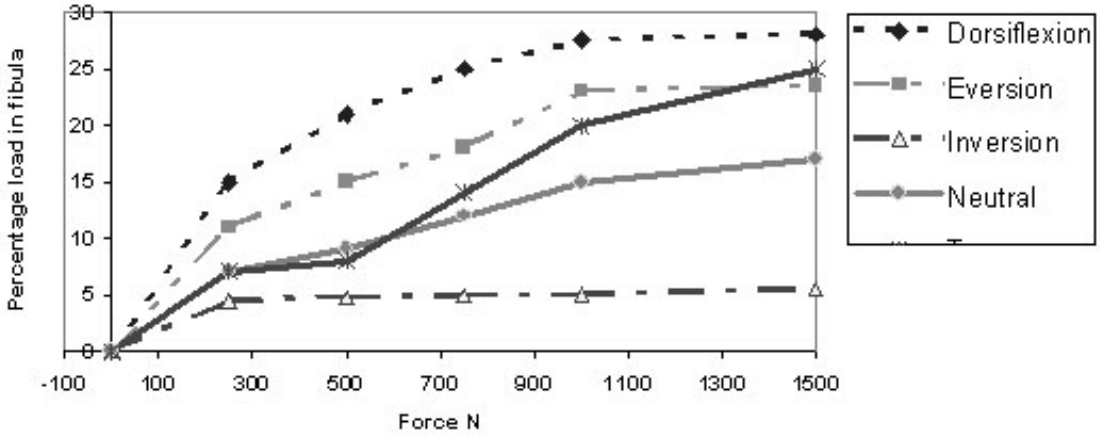

Figure 3.5 Percentage of the total load taken by fibula (adapted from Wang[121])

3.4 Ultra-High-Molecular-Weight Polyethylene

Ultra-high-molecular-weight polyethylene (UHMWPE) is the current "gold standard" in bearing materials of total joint arthroplasty. It is a biocompatible and low friction. As a highly nonlinear material, it will elongate significantly before failure, compensating for low mechanical properties. The major problem with UHMWPE has been wear. Even though the bulk UHMWPE is biocompatible, wear particles are believed to be responsible for osteolysis, resorption at the bone-implant interface and subsequent aseptic loosening of implants.[122-124]

3.4.1 Mechanical Properties and Wear Characteristics of UHMWPE

Modeling macroscopic yielding and plastic flow of UHMWPE can be described by a true stress-strain relationship. In true stress-strain, the compressive and tensile behaviors of UHMWPE up to the point of macroscopic yielding (discussed in the paragraph below) are almost identical.[125] A number of FEM models have used classical von Mises failure theory to simulate the true stress-strain behavior of UHMWPE.[15, 126-132] The von Mises criterion is based on the deviatoric stress tensor and is thereby independent of hydrostatic pressure and open in 3-D stress space. The total strain is a sum of elastic and plastic strain. Based on the assumption of independence of hydrostatic pressure, the plastic deformation must be incompressible. Incompressibility in plastic deformation was confirmed in experiments by Kitagawa et al.[133] and Kurtz et al.[125] The results by Kurtz et al.[125] also showed that von Mises criterion over- predicts permanent strains by up to 225%. Some other theories have been developed for modeling of plastic

deformation of UHMWPE and are reviewed in the article by Bergstrom et al.[134] They include the Arruda-Boyce model, the Bergstrom-Boyce model, the Hassan-Boyce model and a new Hybrid model. These models to our knowledge have not been used in FEM modeling yet. According to the article[134], all models including von Mises perform well for monotonic loading which is the type of loading used in our study.

UHMWPE is a semi-crystalline polymer consisting of crystalline regions and amorphous phase. The crystalline regions are grouped into cells to form lamellae.[135] The lamellae made of folded polyethylene chains are arranged into formations called spherulities. The inelastic response of polyethylene starts at low true strains of 0.02.[125] This offset yield strain is attributed to deformation of the amorphous phase with no plasticity induced in lamellae. With increasing load, stresses from the amorphous phase are transmitted to lamellae through "tie chains" and inter-crystalline links.[136] At a true strain of approximately 0.17, the lamellae undergo irrecoverable plastic deformation associated with the macroscopic yielding of polyethylene. Nucleation of microvoids with subsequent coalescence of these microvoids in the amorphous region leads to final failure of the polyethylene at true strains of approximately 1.5. FEM studies show that strains in nonconformal geometries of knee liners can reach values of 0.12,[127, 137] close to the strains causing permanent deformation of lamellae. Conformal geometries of hip liners typically reach strains of 0.01[137] well below the yield limit of the amorphous phase.

Three mechanisms of wear have been observed in retrieved orthopaedic implants: abrasive, adhesive and fatigue wear. Abrasive wear occurs when a hard foreign body particle is trapped between articulating surfaces. Adhesive wear occurs when asperities of

polyethylene surface are sheared off by the contacting metallic surface. This is possible only with boundary lubricating film under starved lubrication.[138] Fatigue wear is divided into two groups: pitting and delamination, depending on the origin and direction of propagation of micro-cracks. These micro-cracks are driven by shear stresses which depend strongly on the conformity of the articulating surfaces. Delamination is a type of fatigue wear in which micro-cracks start below the surface and propagate parallel to the surface. This is due to shear stresses in nonconformal geometries in which the maximum shear stresses are below the surface.[139] Pitting is defined as wear in which micro-cracks start on the surface and propagate perpendicular to the surface. This type of wear occurs in both conformal and nonconformal geometries. Propagation of these micro-cracks is associated with cyclic tensile-compressive stresses at the edges[139] and residual tensile stresses due to plastic deformation.[126] The results of Pruitt et al.[140] showed that fatigue cracks can propagate even during completely compressive loading cycle. This phenomenon is also associated with residual tensile stresses created at the notch of a damaged zone.

The most dominant mode of failure of nonconformal geometries in knee implants is pitting and delamination.[124, 132, 141] Conformal geometries represented by hip implants exhibit polished surfaces.[124] Polishing (burnishing) is a hybrid of abrasion and fatigue wear mechanisms. The wear rate of conformal geometries is much smaller than the wear rate of nonconformal geometries. However, conformal surfaces create small, submicron size particles that are believed to trigger more pronounced adverse bone reaction than large size particles.[142]

Recently, three new paradigms of polyethylene wear have been proposed by Edidin and Kurtz.[124] The first tenet is that wear occurs on a microscopic scale. The burnished surface of hip implants shows evidence that a number of modes of wear (abrasive, delamination, pitting) can occur at the same time. The second tenet emphasizes the importance of kinematics. It has been shown that the complex three-dimensional kinematics of hip implants produces more wear than the kinematics of knee implants that are constrained much or less to one plane.[143] The third tenet emphasizes the fact that a cyclicly induced plasticity damage layer is a precursor of wear.

3.4.2 The Effect of Thickness on Stresses of UHMWPE

The effect of thickness of the polyethylene on contact pressure was investigated by Bartel et al.[139, 144] Based on an axisymmetric solution of a rigid spherical indentor, Bartel et al.[144] suggested minimum thickness of 4 mm for nearly conformal surfaces and minimum thickness of 6 mm for nonconformal surfaces. A more complex analysis describing contact surfaces in two perpendicular planes[139] suggested that the thickness of the polyethylene be 8-10 mm. On the other hand, fully conformal surfaces did not benefit from increased thickness.[144] This later result is in agreement with retrieval study done by Psychoyios et al.[145] who reported that fully conformal knee bearings 3.5 mm thick wore with the same rate as 11.5 mm thick bearings. There is evidence that the wear rates varied by order of magnitude while surface contact pressures differed very little.[124] It was suggested that wear of polyethylene depends more on nonlinear deformation mechanics[124] and on kinematics[124, 143] than contact pressure which depends primarily

on elastic properties of the material.[124] For ductile materials, contact pressure cannot be directly related to the yield of the material. No data has been found in the literature studying the effect of the polyethylene thickness on von Mises stress. Although a study by Komvopoulus et al.[146] found that increased thickness of hard protective layers decreased von Mises stresses in the softer substrate. However, the polyethylene is softer than the metal tray underneath it and the results from the above study may not apply.

3.5 FEM Models of UHMWPE

Only two papers[6, 15] were found analyzing stresses in the polyethylene inserts of ankle implants. Lewis and Austin[6] investigated stress distribution of stresses in a 2-D model of a generic implant (see Section 3.1.2). The UHMWPE was modeled as linear elastic material and the model was loaded with 2,590 N. They found maximum von Mises stresses of 2.8 MPa, which are below the reported fatigue strength of 6 MPa.

Mciff[15] investigated stresses in 3-D models of two ankle joint implants, the Agility® implant and the STAR implant. The UHMWPE was modeled as nonlinear elasto-plastic material. The models were loaded with 3,650 N and included coefficient of friction. The effect of combined axial, shear and torsional loads was examined. The talar component was rotated to simulate dorsi-plantar flexion. Both models predicted stresses above a yield limit of 20 MPa. In the case of the Agility® implant, point and edge loading was evident and inclusion of friction increased stresses by 50%.

Bartel et al.[139] analyzed stresses in 3-D models of conformal hip implants and nonconformal knee implants (the results of the analytical solution are presented in Section 3.4.2). The load used in the models was 3,000 N. Contact stresses of models with

material properties similar to the polyethylene in our model reached 18 MPa for hip implants and 40 MPa for knee implants. The maximum principal stress was located on the surface. The maximum shear stresses of knee implants and hip implants reached 9 MPa and 7 MPa respectively. The difference between the maximum shear stresses of the designs was smaller than the differences among other components of stresses. For hip implants, the maximum shear stresses always occurred on the surface while the shear stresses in knee implants peaked one to two millimeters below the surface.

A similar study was preformed on eight knee designs.[127] Contact pressures varied from 40-60 MPa while von Mises stress fluctuated from 23-28 MPa. The biggest variation was in von Mises strain (0.04-0.1) which can be explained by the relatively flat region of the nonlinear stress-strain relationship in polyethylene.

Kuster et al.[132] investigated the effect of conformity and load on stresses of polyethylene employing a parametric 2-D plane strain FEM model. Increasing loads increased stresses linearly for all conformity ratios. Change of conformity ratio from 0.95 to 0.99 caused a significant increase of the contact area, lowering both the contact pressure and von Mises stress. They found stresses to be more dependent on conformity than on increased load.

3.6 Analytical Solutions of Conformal Cylindrical Surfaces

Nonconformal contact of two bodies is defined as contact that occurs over an area significantly smaller than the dimensions of the contacting surfaces. This problem was first successfully solved by Hertz.[147] The assumptions made in this theory are as follows: (1) the contact is nonconformal with elliptical contacting areas; (2) each body is

represented by a semi-infinite medium; (3) strains are small and (4) the surfaces are frictionless.[148] Our study is primarily aimed at the computer simulation of conformal surfaces. Conformal surfaces differ from the assumption made in Hertzian theory because the contact area is of the same magnitude as the dimensions of the contacting bodies. Also, the assumption of a semi-infinite medium is violated because the thickness of the polyethylene insert is finite and relatively thin.

Analytical solutions to Hertzian contact of two contacting cylinders are available in the literature.[148, 149] but analytical solutions to conformal geometries are more difficult to find. Persson[150] used stress functions to approximate a circular disc contacting an infinite plate with a circular hole.[148] Kalker[151] solved a non-Hertzian contact problem for a long cylinder and an elastic half space and determined the shape of the contact area except in the regions near the edges. Some other analytical solutions for two conformal cylinders can be found in the literature, however, all of them assume semi-infinite or infinite media.

More recent solutions use numerical techniques to solve contact problems for a variety of shapes. These numerical solutions discretize the indenter shape in 3-D space while the indented body is semi-infinite. Two such solutions of indenting cylinders[152, 153] show stress concentrations at the edges due to the finite length of cylinders. To reduce the stress concentrations, the axial profile of the cylinder should be either barreled[148] or crowned.[153] This barreling or crowning may be difficult to manufacture and works only for the design load. For example, to decrease stress concentrations at the edges, a cylinder of 11 mm diameter would have to have crown drop of 9 μm.[153] Recently, a 2-D

analytical solution[154] has been proposed for calculating stress concentrations due to edges on the flat profiles of some knee implants. This analytical solution could be used instead of the earlier mentioned numerical solutions to calculate the stress concentrations of cylinders of finite length.

4.0 MODEL DESCRIPTION

This section describes development of the three-dimensional (3-D) FEM model of the ankle joint and implant. Section 4.3.1 describes the contact elements and parameters of the 3-D FEM model and includes the contact parameters and settings used for contact elements in 2-D FEM models.

4.1 Development of the Solid Models of the Bones

A human cadaveric lower leg specimen was cross-sectioned to create a solid model of three bones; the distal thirds of the tibia and fibula and the proximal half of the body of the talus. The talar dome (trochlea) is removed during surgery for insertion of the talar component and was not included in our model. Gross inspection revealed no degenerative disease of the cadaveric foot. A procedure of slicing the bone with a band saw and scanning of cross sections was chosen due to cost effectiveness. Previous experiments with creating FEM models by slicing showed that all bones must be present to preserve the original positions of the bones with respect to each other. The specimen was stripped of soft tissues except for the ligaments holding the tibia, fibula and talus in place. The neutral position .(Figure 4.1) was achieved in the following procedure:

1. the longitudinal axis of the tibia (Z axis of the model) was set perpendicular to the plantar surfaces of the foot,
2. the Y axis was aligned with the middle axis of the foot (see Figure 2.6)
3. the proximal end of the fibula was moved posteriorly[34].

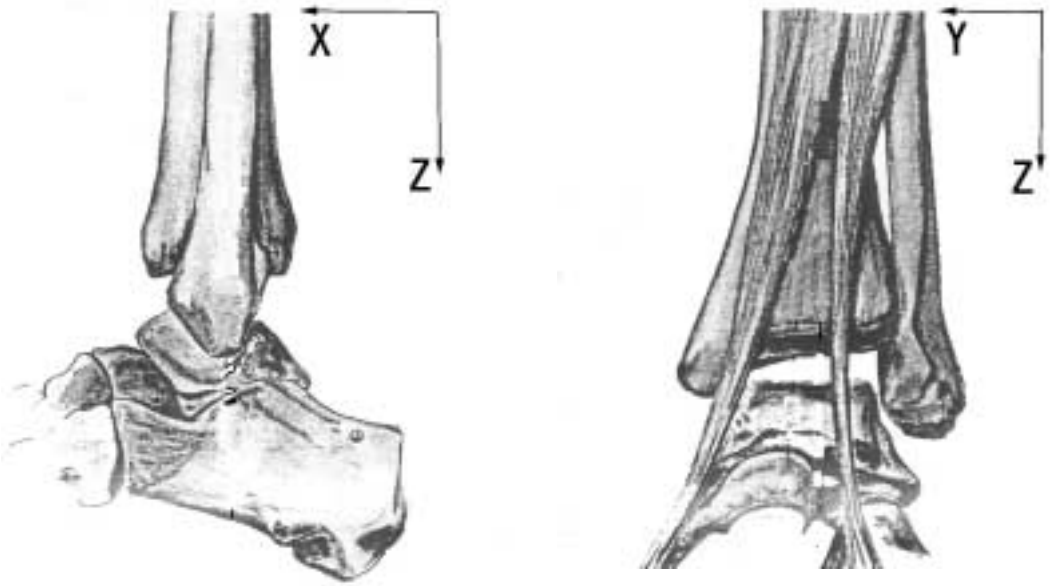

Figure 4.1 Alignment of bone axes in the FEM model

The position of the fibula was checked for compliance with the criterion needed to create smooth surfaces. That is, from the standpoint of creating smooth surfaces in ANSYS5.5 using the ASKIN command, the alignment of spline endpoints between slices was important. This phenomenon was also observed by Greening[155] who referred to the unevenness of the surfaces as "rumples". In order to have spline endpoints of the slices aligned along the whole Z axis, the lines L1 and L2 (Figure 4.2) had to be at a constant distance from Y axis throughout the model. This was easily achieved for wide slices and the fairly straight shaft of the tibia. However, the position of the fibula had to be checked so that there was a constant distance Y for all cross sections.

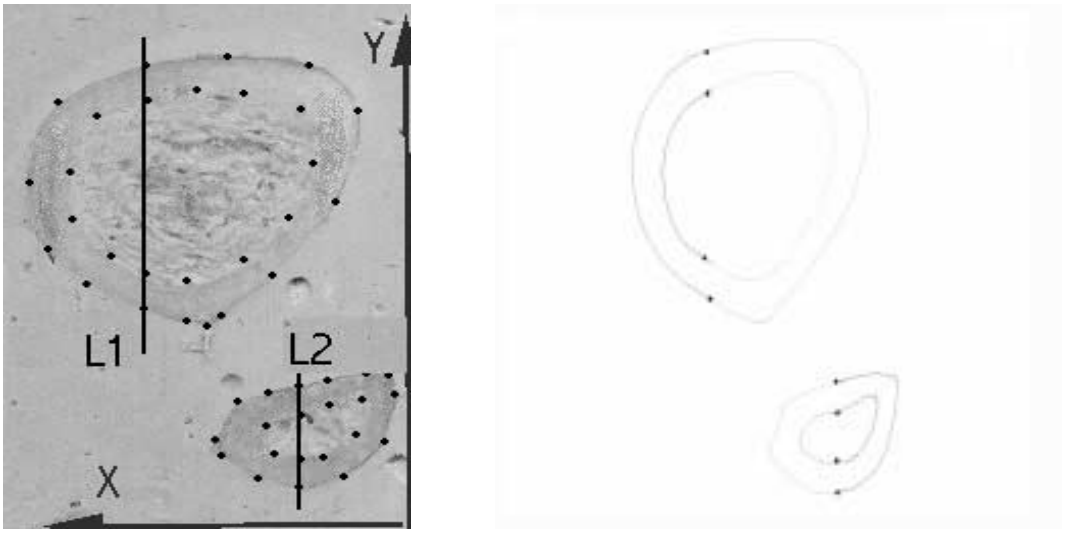

A B

Figure 4.2 A cross sectional slice of the tibia and fibula. A) Edge detection in Scion Image. B) splines put through the detected points in ANSYS5.5

Once the specimen was aligned in the mold, epoxy resin was poured in, making sure that cavities underneath the specimen were filled. The specimen was then sectioned on a band saw using a blade with 18 teeth per inch. Previous experience showed, that the regions near the joint had to be sliced very thin, preferably as thin as one mm. However, thin slices of bone had a tendency to fall out of the surrounding matrix, making optical scanning difficult. Instead, it was decided to cut off a thin slice and scan the remaining bone instead of the slice. Since bones were sliced from the bottom of the foot, this procedure allowed us to measure the Z coordinate of the slice after the cut was made. Twenty-nine cross sectional slices were scanned (Figure 4.3).

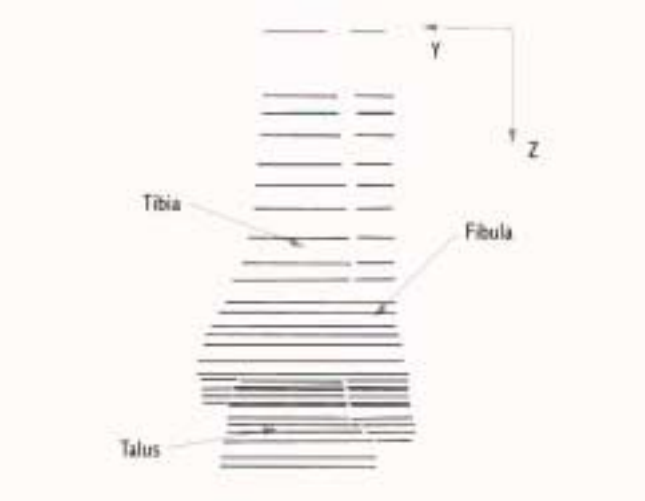

Figure 4.3 Cross sectional slices used in the model. The regions around the ankle joint were sliced in one mm increments

The scanned slices were then imported into Scion Image (Scion Corporation, Maryland, USA). Lines L1 and L2 (Figure 4.2A), at constant distances for all slices, were drawn. Edges of the cortical and cancellous bone were detected manually and recorded as X-Y coordinates for each particular slice*. Only the outside cortical surface was detected for the portions of the bones with thin cortical bone (more in Section 4.2). All data was then transferred into MATLAB (Mathworks Inc., Natick, Massachusetts). A MATLAB program translated the data into ANSYS Parametric Design Language (APDL) of ANSYS5.5 (Ansys Inc. Southpoint, PA) FEM program. Creating models in

* Previous experience showed, that using many detection points (appr. more than 15 for one spline) to capture an "exact" shape of the cross section failed in Boolean operations when the implants were inserted into the bones. The number of detected points as shown on Figure 4.2A proved to be sufficient to capture the cross sectional geometry and avoid problems with Boolean operations.

APDL allowed small changes in the model to be made by adjusting a parameter in a particular command rather than by recreating the entire model. The detected edge points were converted to keypoints. Splines were generated through the keypoints to create 'ribs'. At least two splines per slice were necessary to create a surface as described below. The splines had to start and end at the same distance from the Y axis as discussed earlier (Figure 4.2B). Areas were created by skinning the 'ribs' using the ASKIN command. Two areas were created at the bottom and top of the skinned surfaces to create volumes. Since the tibio-fibular syndesmosis is fused, no articular surfaces between the tibia and fibula were created. In addition, the trochlear surface of the body of the talus (dome) was not modeled since it is resected during the surgery. The amount of the dome resection was equal to the height of the talar component.

For simply connected volumes, the procedure described in the above paragraph could be completed automatically without manual intervention. However, the medial malleolus was not simply connected to the rest of the shaft because of a sudden increase of cross sectional area. A simplified approach was used to create the medial malleolus. In this particular ankle arthroplasty, one third of the medial malloelus is cut off for implant insertion. Instead of creating a thin medial malleolus that would be difficult to connect to the wide shaft, we created a medial malleolus as wide as the shaft of the distal tibia. Then, most of the bone was resected and only two thirds of the original volume of the medial malleolus remained.

4.2 Assembly of the Models

Two different talar component designs were studied: one standard shape and one proposed new design. The “Standard” shape has been used clinically and the model was created in-house together with the tibial component and UHMWPE insert. The new shape will be referred to in our study as “Modified” (Figure 4.4). This implant has a base (flange) with posterior and anterior edges of equal width. The articulating surface became almost rectangular compared to the original trapezoidal shape. The “Modified” talar component was provided as IGES files from DePuy company, Warsaw, Indiana. It had to be fixed in ANSYS as the translated geometry contained many small areas that would be difficult to mesh with elements.

Figure 4.4 “Standard” and the “Modified” Shapes of the talar component

The whole model was first assembled with the "Standard" shape ankle implant. The talus and the talar component from the "Standard" talar shape model were then deleted and the "Modified" shape of the talar implant was inserted and aligned with the UHMWPE insert. The talus was inserted and positioned to get the best possible fit with the "Modified" talar component.

The assembly of the "Standard" talar implant model was performed in accordance the surgical guidelines of the DePuy Company.[31] Two thirds of the lateral and medial malleolae were left intact, the rest was resected for the tibial component. We simulated in-growth of the bones into the implant by leaving an overlapp of approximately one mm of bone on each side of the implant (Figure 4.5). This recess was then removed by Boolean operations with the implant, allowing the interface between the bone and implant to be fully bonded. According to surgical guidelines[31], the tibial component should be "*flush both anteriorly and posteriorly. Occasionally, the very posterior aspect of the tibial component will not seat completely*". This was in contradiction with our observation. As can be seen in Figure 4.5, the 20° incline of the anterior wall of the tibial tray left a significant amount of cortical and cancellous bone uncovered. The potential misalignment was discussed with Dr. Stephen Conti, clinical collaborator, University of Pittsburgh Medical Center. He advised that the anteriorly inserted implant be pushed in until the anterior lip of the tibial tray was flush with the cortical bone of the tibia. He also noted that the anterior wall of the implant was not flush with the cortex of the tibia.

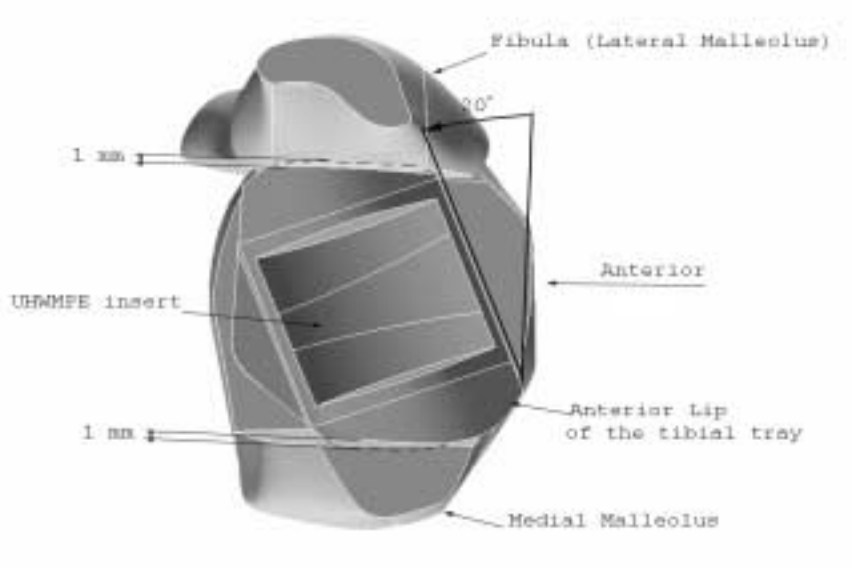

Figure 4.5 Alignment of the tibial tray with the fused tibia and fibula

. The tracks for insertion of the implant were not cut for both, the tibial and talar components. Instead, the implant components were perfectly bonded to the bones allowing no sliding at the bone-implant interface. The tibia and fibula were fused. Two titanium screws of a three millimeter diameter are used surgically to promote the fusion. Instead of creating volumes for screws, it was decided to use beam elements. A screw approximated by beam elements must have nodes aligned along a line. To create a line, the volumes of the tibia and fibula were cut in two perpendicular planes for each of the screws. The first screw was placed one centimeter above the top of the tibial tray. The second screw was placed one centimeter above the first screw (more about meshing the screws in Section 4.3).

Finally, the talar component was positioned into the UHMWPE insert. When aligned with the UHMWPE insert, the talar component was rotated 20º laterally from the midline of the foot (Figure 4.6) to approximate orientation of the empirical ankle axis in the transverse plane (Figure 2.6A, page 10). The volume of the talus was inserted last. The talar component was overhung posteriorly and did not comply with the instructions in the surgical guidelines.[31] The talus was moved two millimeters posteriorly to improve the fit. It was our assumption that this also occurs surgically, i.e., surgeons position implants to get the best fit, even though the original position of the bones was not preserved. This may require soft tissue balancing and possible tendon lengthening.

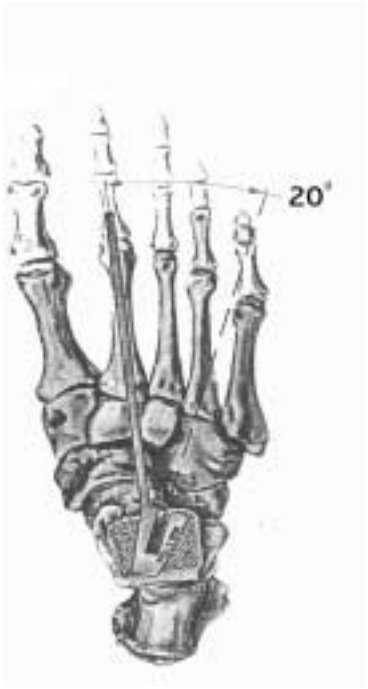

A, B,

Figure 4.6 Position of the "Standard" talar component A) according to surgical guidelines[31] B) in our model

4.3 Meshing of the Model

This section deals with meshing of the model that is common to both the polyethylene stress analysis and bone stress simulations. Complicated volumes in the model prevented us from meshing the model with hexahedral elements. The next best available option was tetrahedral elements with quadratic displacement functions (Solid92). Long bones like the tibia and fibula are distinguished by thick cortical bone in the midshaft, thinning continuously towards the epiphysis (Figure 2.10, page 22). The thickness of the cortical bone of the specimen decreased from approximately four millimeters in the midshaft to less than one millimeter in the epiphysis. To create a complete volume of cortical bone would require a very large number of Solid92 elements making the model unfeasible. Moreover, small sharp volumes could create a problem in Boolean operations. We therefore decided to use shell elements in the distal parts of the tibia and fibula where the thickness of cortical bone was one millimeter or less. Only the volume defined by the outside contours of the bones was created and was overlaid with shell elements (Figure 4.7). The Shell91 element was chosen for its ability to locate nodes on the top surface (Keyopt(11)=2), thereby offsetting the thickness towards the inside of the volume. Shell elements, compared to solid elements, have extra rotational degrees of freedom that will be activated by underlying cancellous bone. The main role of these shell elements in our model was to transfer the proper portion of the load to the lower part of the model. Since the transition between the solid and shell elements is far removed from the area of interest, any artifacts will be negligible and will not affect the results. In addition, the tibial tray and surrounding bones were not a part of the current study. The

proximal part of the tibia and fibula with thicker cortical bone had separate volumes for cortical and cancellous bone and were meshed with Solid92 elements.

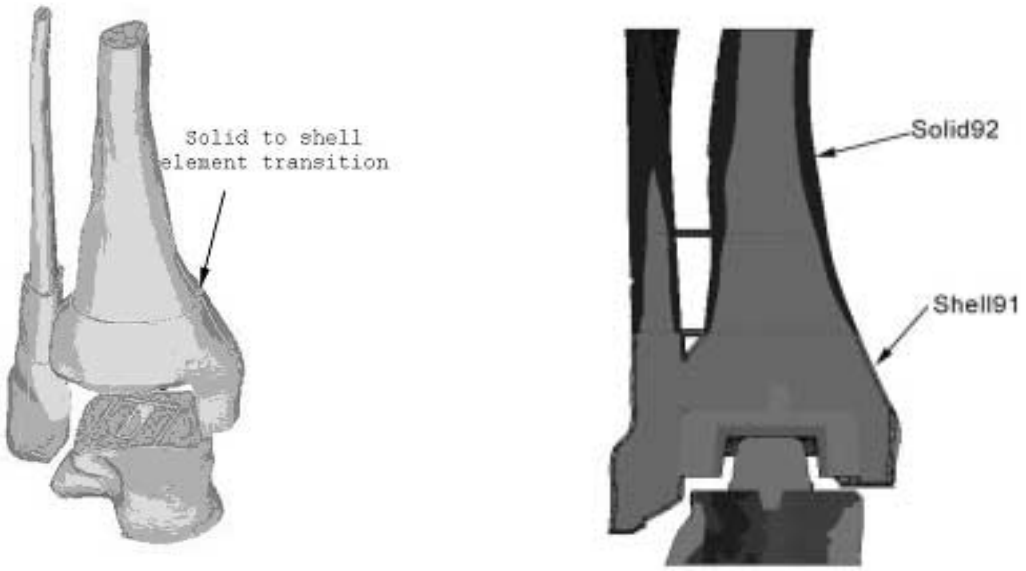

A, B,

Figure 4.7 A) Volumes of the cancellous bone. B) Cross-sectional view of the finite element model. The upper part of the fibula is tilted backwards coming out of the cross-sectional view

The talus was the only bone in our model for which a detailed stress analysis was desired. Therefore, a separate volume for cortical bone of one-millimeter thickness was created and meshed with solid elements.

The two screws that promote the fusion were created after the tibia and fibula were meshed. Nodes lying on the lines that were created as described Section 4.2 were selected and meshed with beam elements (Figure 4.7).

4.3.1 Contact Elements

Contact elements are used to satisfy the impenetrability condition. Total impenetrability cannot be achieved numerically in a reasonable amount of CPU time and a specific tolerance of penetration must be specified (FTOLN factor discussed below). The two most common methods for satisfying contact compatibility are:

1. Penalty method. With the penalty method, springs are put into the contact interface. The higher the contact stiffness (k) the less penetration. However, a high value of (k) may lead to convergence difficulties because the stiffness matrix [K] becomes ill conditioned. The stiffness matrix [K] is only modified not enlarged. There is an option in ANSYS to run the model only with this method.

2. Lagrange multiplier method. This method adds an extra degree of freedom (contact pressure) to satisfy the impenetrability condition. This extra degree of freedom enlarges the stiffness matrix [K]. ANSYS did not provide this method until the release of the latest version of ANSYS6.0.

ANSYS combines these two methods as a method called the augmented Lagrangian method. During the first series of iterations, the penalty method is used to enforce the impenetrability. After achieving equilibrium, the penetration tolerance is checked. Then, the Lagrange multiplier method is introduced, and if necessary, the contact pressure is increased. This method requires two real constants, FKN and FTOLN, to be adjusted depending on the materials coming into the contact and on the type of the problem being solved. Positive values of all discussed contact constants (FKN, FTOLN, PMIN, PMAX, ICONT) are interpreted by ANSYS as scaling factors while negative

values are interpreted as absolute values. ANSYS uses the depth of the underlying elements as the reference value for scaling.

FKN- Normal stiffness factor. A smaller value provides faster convergence but more penetration. The default value FKN=1 is suitable for bulk deformation while a smaller value (0.01-0.1) is recommended for problems in which bending is dominant.

FTOLN- Tolerance factor in the direction normal to the surface. It is used only with the augmented Lagrangian method to check if the penetration tolerance is less than FTOLN*depth of the underlying solid elements. The default value is FTOLN=0.1. Lowering this parameter will improve the appearance of the contact stresses but can cause an excessive number of iterations or non-convergence.

The augmented Lagrangian method is less sensitive to the selection of the FKN than the penalty method and is recommended for general use. The penalty method should be used with highly distorted elements and high coefficients of friction or if the augmented Lagrangian method does not converge.

The general approach in the use of the contact factors can be described as follows:

a) Decide whether the problem is dominated by bulk or bending deformation.

b) Run the model with lower FKN and a default FTOLN.

c) Check the penetration and overall convergence. If the penetration is too high, increase the FKN. Keep increasing the FKN until the problem does not converge or converges very slowly.

d) Take the FKN from the last acceptable run. Run this model with smaller FTOLN to see if the contact pressure contours have smoother appearance and check the

overall increase of time for convergence. Lowering FTOLN could increase computational time significantly.

The above steps were used in our FEM models, employing the augmented Lagrangian method. For the 3-D models, values of FKN=10 and FTOLN=0.01 yielded an acceptable penetration within a reasonable number of iterations. According to the ANSYS manual, increasing FKN by one hundred times may increase contact pressure only by 5%. However, the solution times could become prohibitively large.[156]

Experimentation with contact parameters of the 2-D FEM models showed convergence of results for normal stiffness FKN=1 and penetration parameter FTOLN=0.01.

In the 3-D models, there were two regions where flexible-to-flexible, surface-to-surface contact elements were used. One region was the interface between the talar component and the UHMWPE insert. The other region was areas of a possible contact between the rounded edges around the base of the talar component and the talus and contact areas on the beveled edge and the talus. These contact elements use “target surfaces” modeled with TARGE170 elements and “contact surfaces” modeled with CONTA174 elements. The contact elements were constrained from penetrating the target surface. This rule designated the stiffer material to be the target surface. In our model, the areas on the talar component were meshed with the TARGE170 elements. The interior surfaces of the UHMWPE insert as well as portions of the talus were meshed with the CONTA174 elements. These surface-to-surface contact elements overlay the underlying 3-D SOLID92 elements.

4.3.1.1 Adjustment of Initial Penetration

In a static analysis, any part of the model not initially connected and with no applied displacement constraints can experience rigid body motion (zero stiffness) before the contact is established. The upper part of our model (the fused tibia and fibula, tibial tray, UHMWPE insert) was loaded by forces but was not constrained in the direction of the load. Even though the model was created in a "just touching" position, small gaps or penetrations existed between the bodies due to numerical round-off in the finite element mesh.

There are many ways to establish the initial contact and the method used in our model will be described. ANSYS will physically move a target surface into initial contact if either PMIN or PMAX real constants are specified. This is an iterative process with a maximum up to 20 iterations to establish the initial contact. If the initial penetration is larger than PMAX, ANSYS moves the contacting surfaces to reduce the penetration. If the initial penetration is smaller than PMIN (and within a "pinball" region), ANSYS moves contacting surfaces to ensure the contact. The "pinball" region is defined as a sphere of two times the depth of the underlaying elements. It determines the contact status between the target and contact surfaces. We used PMAX=0.2 and PMIN=0.001 to establish the initial contact for 3-D FEM models. For the 2-D models values of PMIN and PMAX of 0.01 and 0.001 respectively were used.

Initially, after adjusting all these parameters there was a problem in the results of contact pressure distribution in 2-D FEM models. The contact pressure experienced an unexpected jump at the end of the contact area. To eliminate this problem, the ICONT

(initial contact closure constant) variable was set to 1e-7. This constant should be much smaller than the provided default value if other constants (FTOLN, PMIN, PMAX) for stabilizing the initial contact are used.

4.4 Material Properties Used in the Model

Cortical bone was modeled as a homogeneous isotropic material. The thick cortical bone of the tibial and fibular shaft was assigned a Young's modulus of E=17,960 MPa representing diaphyseal cortical bone as in the work of Lewis and Austin.[6] This corresponded well with experiments preformed by Reilly and Burstein[108] (see Table 2). Observations of architecture of cancellous bone in the talus[22] indicated that the plates of trabeculae in the head of the talus were running vertically and parallel to the applied load. This implied that the thin cortical shell was oriented longitudinally with respect to our applied load. For this reason, a longitudinal Young's modulus of metaphyseal bone E=9,650 MPa was chosen based on measurements by Lotz et al.[109] (see Table 3). This material property was assigned to the volume one millimeter thick and three millimeters wide surrounding the resected areas of the talar dome (Figure 4.8). The two three-millimeter-wide volumes immediately below the talar component meshed with cancellous and cortical bone elements contained 44,870 nodes (more in Section 7.0). To save computational time, the size of cortical bone (and cancellous as well) elements increased distally. To compensate for the increased thickness of the cortical bone, a reduced zone with decreased Young's modulus of metaphyseal bone in the distal section of the talus was created in a manner similar to Lotz et al.[98] (Section 3.1.3). The Young's modulus of metaphyseal bone in this reduced zone was one fifth of the original value.

The thin cortical bone in the tibia and fibula modeled with SHELL91 elements was also assigned Young's modulus of metaphyseal bone of 9,650 MPa.

Table 5 Material properties used in the model

Material	E (MPa)	ν	Yield criteria	Failure criteria
-Cortical diaphyseal bone [6]	17,580	0.3	NA*	NA*
-Cortical metaphyseal bone [109]	9,650	0.3	σ_y=100 MPa	ε_u=3%[108]
-Cortical reduced	9,650/5	0.3	σ_y=100/5 MPa	ε_u=3%[108]
-Cancellous homogeneous [6]	280	0.3	NA*	NA*
-Cancellous heterogeneous [100]	500-850	0.3	ε_y=0.8%[86, 91, 92, 97]	ε_u=1.5%[86, 91, 97]
-Cobalt-Chrome Alloy[6]	193,000	0.29	NA*	NA*
-Titanium alloy [6]	110,000	0.33	NA*	NA*
-Polyethylene [157]	557**	0.46	σ_y=10.86 MPa	

*Not part of the current study
**Nonlinear material properties

Cancellous bone of the tibia and talus was assigned a Young's modulus of 280 MPa.[6] For the study of talar stresses, the talus was assigned heterogeneous material properties based on experiments by Jensen et al.[100] (Section 2.6.3.1). Due to the large number of cancellous bone elements in the submodel (more than twenty thousand), it was impractical to assign different material properties to each element. Instead, a group of eight material properties with an increment of 50 MPa of Young's modulus was created. The Young's moduli reported by Jensen et al.[100] were increased by 30% to minimize experimental error.[81] The resulting Young's moduli of the talus were in the range of 500-850 MPa.

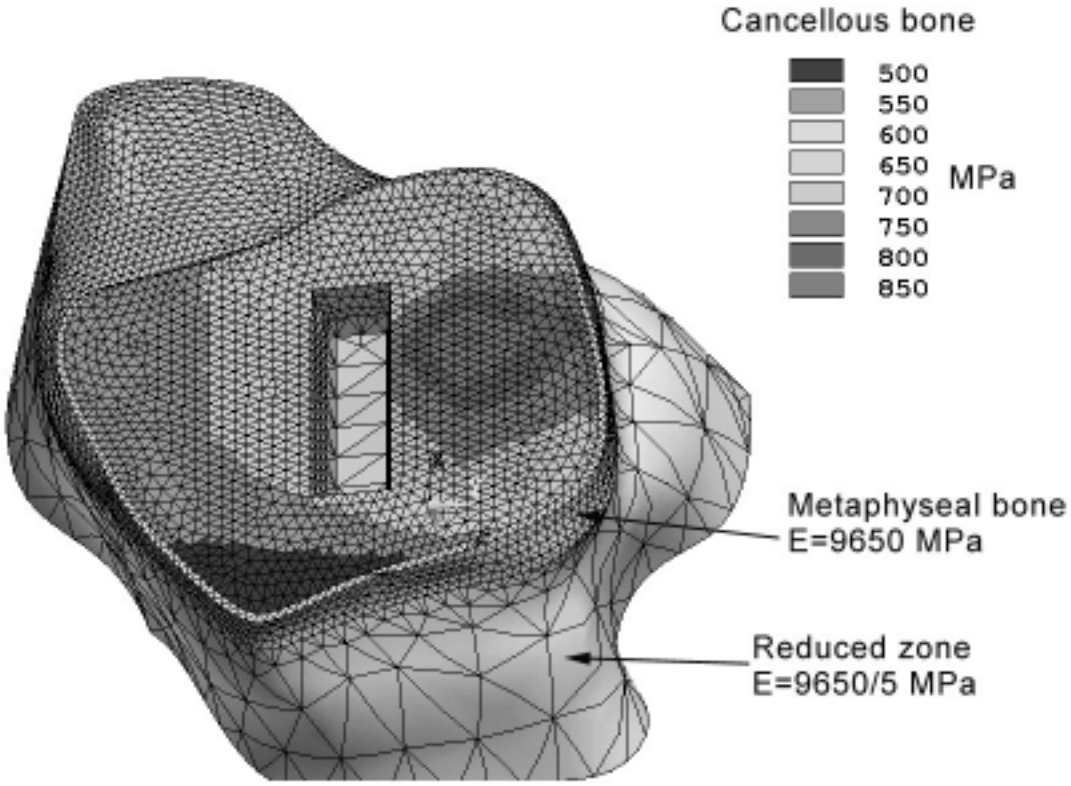

Figure 4.8 Heterogeneous material properties of the talus

The investigated talar bone was expected to be loaded predominantly in compression. It has been shown that in compression, cortical bone can be approximated as an elasto-perfectly plastic material[108] (Figure 2.15). Cancellous bone under compression behaves like a damaging material[63] (Figure 2.12) with pronounced strain softening. To avoid computational difficulties, it was decided to use an elasto-perfectly plastic material model for both cortical and cancellous bone. The elasto-perfectly plastic material properties for cancellous and cortical bone were used only for investigation of talar stresses. The yield stress of the cancellous bone varied with the modulus, based on

the hypothesis that yield strain could be considered constant across anatomic locations.[92] A yield strain of 0.8% was chosen based on the data from various anatomical locations in the human body (see Table 1). This resulted in yield stresses in the range 3.6-6.8 MPa. The yield stress of 100 MPa of the thin cortical bone was used according to experiments by Lotz et al.[109] (Table 3).

The material properties of the polyethylene were taken from work of DeHeer.[157] The Young's modulus of the linear portion of the graph (Figure 4.9) was 557 MPa with a yield stress of 10.86 MPa. The values of total true stress-strain are listed in Table 6. The material properties of cobalt-chrome talar component and titanium alloy for two screws and the tibial tray were based on earlier work of Lewis and Austin.[6]

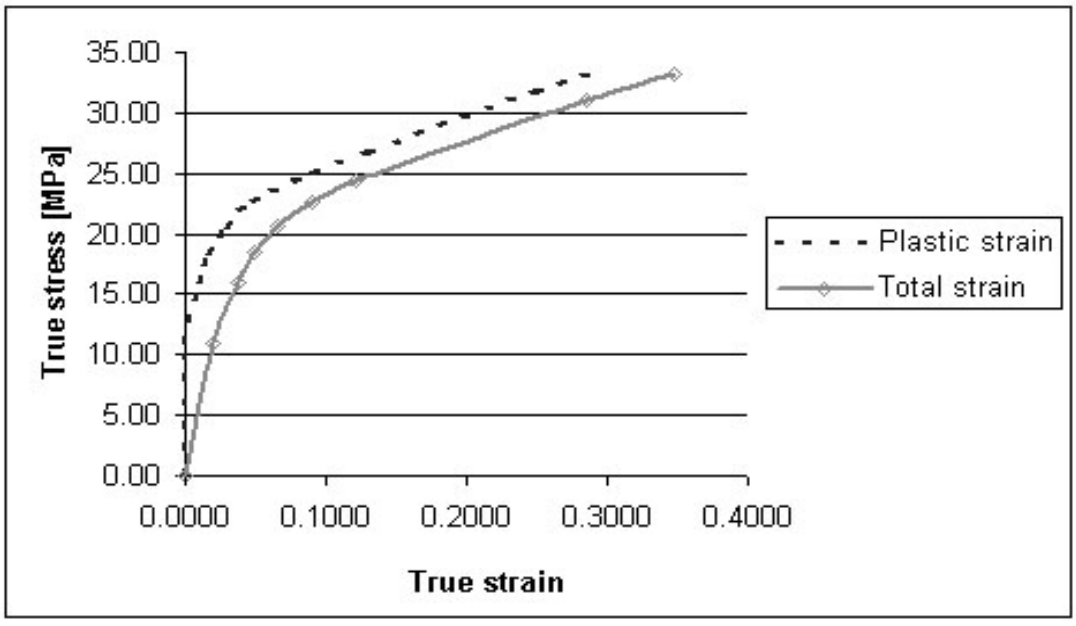

Figure 4.9 Compressive true strain- true stress for UHMWPE[157]

Table 6 Values of the total true stress-strain of the UHMWPE used in our model

True strain	True stress (MPa)
0.0195	10.86
0.0377	15.95
0.0494	18.40
0.0663	20.65
0.0897	22.70
0.1216	24.44
0.2853	31.12
0.3477	33.12

4.5 Loads Applied to the Models

Five times a body weight[21, 115] of 68 kg was to be applied to the tibia and fibula. The load was distributed between the fibula and tibia. The literature review (Section 3.2) revealed no conclusive results about the weight-bearing of the fibula due to the difference between the measurements taken with strain gages or force transducers. Moreover, the weight-bearing of the fibula resting on the implant had not yet been determined experimentally. Since we were unsure of the load applied to the fibula, we used the FEM model to calculate the portion of the load carried by the fibula. Thus, the distal end of the fibula and tibia were constrained. The talar component and the talus were omitted from calculations and a load of the five times body weight of 68 kg was applied as a pressure upwards to the UHMWPE insert. The distal ends of the fibula and tibia were constrained. Structural surface effect elements SURF154 were used to apply a pressure on projected area of the contact between the talar component and the UHMWPE insert. This simulated

parabolic contact pressure in the saggital plane. In the frontal plane the contact pressure was assumed to be constant. The reversed reaction forces from the constrained ends of the tibia and fibula were used in a later step as loading boundary conditions.

5.0 ANALYTICAL SOLUTION OF TWO COUNTERFORMAL CYLINDERS

An analytical solution for the stresses in two contacting counterformal cylindrical bodies is derived based on the analytical solution of indenting spheres proposed by Bartel et al.[144] The cylinder of radius r_c is a rigid body representing the metal component of the implant (Figure 5.1). The contact occurs along the inside radius r_i of the polyethylene. The outside surface of radius r_o is typically backed by a metallic plate and therefore can be considered constrained. The rigid cylinder is pushed down by load w acting over length L along the plane of symmetry $\theta=0^\circ$. The load will displace the inside surface of the polyethylene in the radial direction by an amount of $b(\theta)$. The surface displacement $b(\theta)$ varies from zero at the end of the contact at $\theta=\theta_{max}$ to the maximum value of Δ at $\theta=0^\circ$ and is symmetric about the plane of symmetry.

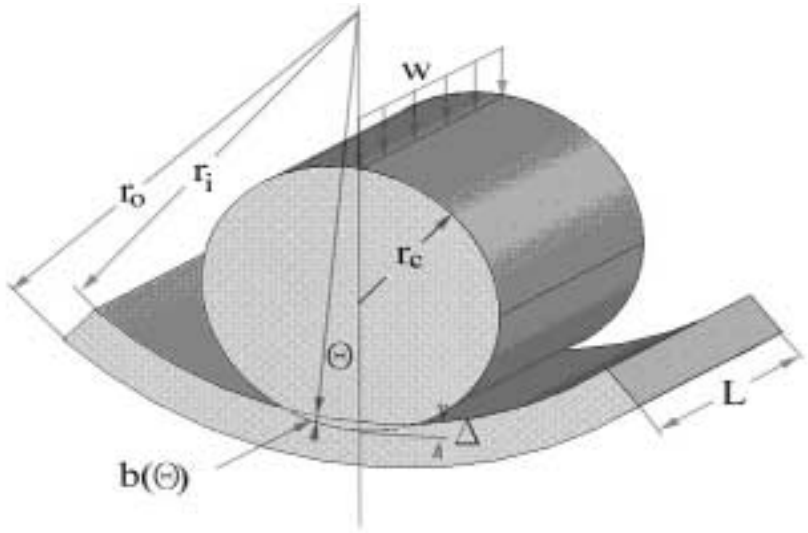

Figure 5.1 Problem statement for contact of two counterformal cylinders

The problem is solved by applying the prescribed displacement boundary conditions b(θ) from the rigid cylinder on the elastic body of the polyethylene. The assumptions are: (1) the radial displacement u_r is much larger than the angular displacement u_θ; (2) the derivatives of quantities with respect to the coordinate θ can be neglected and (3) plane strain conditions can be assumed for cross-sections away from the ends, i.e. the displacements u_z can be neglected. The plane strain condition makes the displacements u_r and u_θ independent of the z coordinate. The problem becomes one of plane strain for a thick cylinder with prescribed displacement boundary conditions. The strain-displacement equations in cylindrical coordinates yield

$$\varepsilon_{rr} = \frac{\partial u_r}{\partial r}, \quad \varepsilon_{\theta\theta} = \frac{1}{r} u_r \tag{1}$$

The constitutive equation, in index notation, is

$$\sigma_{ij} = 2\mu\varepsilon_{ij} + \lambda\varepsilon_{kl}\delta_{ij} \tag{2}$$

where

$$\lambda = \frac{E\upsilon}{(1+\upsilon)(1-2\upsilon)}, \quad \mu = \frac{E}{2(1+\upsilon)} \tag{3}$$

are Lame's constants, E is Young's modulus and υ is Poisson's ratio.

Substituting Eq. (1) into Eq. (2) and expressing Eq. (2) as components yields

$$\sigma_{rr} = (2\mu + \lambda)\frac{\partial u_r}{\partial r} + \frac{\lambda}{r} u_r \tag{4}$$

$$\sigma_{\theta\theta} = \lambda\frac{\partial u_r}{\partial r} + \frac{1}{r}(2\mu + \lambda)u_r \tag{5}$$

with other components of the stress tensor equal to zero. However, the assumption of plane strain creates stress component σ_{zz} in the longitudinal direction. Since the shear stress components are zero, the σ_{rr} and $\sigma_{\theta\theta}$ are the principal stresses, and we can write

$$\sigma_{zz} = \upsilon(\sigma_{rr} + \sigma_{\theta\theta}) \tag{6}$$

The equations of equilibrium reduce to the single equation

$$\frac{\partial \sigma_{rr}}{\partial r} + \frac{1}{r}(\sigma_{rr} - \sigma_{\theta\theta}) = 0 \tag{7}$$

Substituting Egs. (4) and (5) into Eg. (7) yields the equilibrium equation

$$\frac{\partial^2 u_r}{\partial r^2} + \frac{1}{r}\frac{\partial u_r}{\partial r} - \frac{1}{r^2} u_r = 0 \tag{8}$$

The general solution of Eq. (8) is taken to be of the form

$$u_r = Ar + \frac{B}{r} \tag{9}$$

where A and B are constants to be determined from boundary conditions. Based on the assumptions made earlier the displacement boundary conditions can be written as

$$u_r(r_o) = 0\,, \quad u_r(r_i) = b(\theta) \tag{10}$$

Substituting these boundary conditions into Eg. (9), leads to

$$A = \frac{b(\theta)}{r_i\left[1-(r_o / r_i)^2\right]}, \qquad B = \frac{-b(\theta) r_o^2}{r_i\left[1-(r_o / r_i)^2\right]} \tag{11}$$

The stress components can now be expressed as

$$\sigma_{rr} = \frac{2b(\theta)}{r_i\left[1-(r_o / r_i)^2\right]}\left\{\mu\left[1+(r_o / r)^2\right] + \lambda\right\} \tag{12}$$

$$\sigma_{\theta\theta} = \frac{2b(\theta)}{r_i\left[1-(r_o / r_i)^2\right]}\left\{\mu\left[1-(r_o / r)^2\right] + \lambda\right\} \tag{13}$$

$$\sigma_{zz} = \frac{4\upsilon b(\theta)}{r_i\left[1-(r_o / r_i)^2\right]}(\mu + \lambda) \tag{14}$$

The relationship between the prescribed boundary condition b(θ) and the geometry of the model was derived by Bartel as

$$r_c^2 = [r_i + b(\theta)]^2 + (r_i - r_c + \Delta)^2 - 2[r_i + b(\theta)](r_i - r_c + \Delta)\cos(\theta) \tag{15}$$

Solving for b(θ) produces

$$b(\theta) = \left[\cos(\theta) + \sqrt{\left(\frac{r_c}{(r_i - r_c + \Delta}\right)^2 - \sin^2(\theta)}\right](r_i - r_c + \Delta) - r_i \tag{16}$$

The end of the contact region between the two cylinders occurs at angle θ_{max}, which can be determined from Eq. (15) by setting b(θ)=0

$$\theta_{\max} = \cos^{-1}\left[\frac{r_i^2 - r_c^2 + (r_i - r_c + \Delta)^2}{2r_i(r_i - r_c + \Delta)}\right] \tag{17}$$

The equilibrium of forces in the vertical direction gives a relationship between the total applied force P and the contact pressure σ_{rr} in the form

$$P = 2\int_0^{\theta_{\max}} \sigma_{rr}[r_i + b(\theta)]\cos(\theta)d\theta \tag{18}$$

where P is the force per unit length

$$P = \frac{w}{L} \tag{19}$$

The von Mises stress in terms of principal stresses can be calculated from the following equation:

$$\sigma_{vm} = \sqrt{0.5*[(\sigma_{rr} - \sigma_{\theta\theta})^2 + (\sigma_{\theta\theta} - \sigma_{zz})^2 + (\sigma_{rr} - \sigma_{zz})^2]} \tag{20}$$

The equations are solved in two steps. First, the maximum surface displacement Δ is estimated and the equilibrium Eq. (18) is solved iteratively for σ_{rr} ($r=r_i$). Then, the components of stresses are found from Eqs. (12-14). If the calculated maximum contact angle θ_{max} is larger than the actual angle due to the geometry of the elastic cylinder, the algorithm is altered as follows. The quantity θ_{max} is not calculated by Eq. (17), and instead is set as a constant based on the geometry. Then, the contact pressure and $b(\theta)$ at θ_{max} are not zero and can be calculated.

5.1 Analytical Solution Comparison to FEM

The analytical solution was compared to a geometrically identical two-dimensional FEM model. Only fully conformal and almost conformal geometries were investigated, relevant to the research of conformal ankle implants. The conformity ratio was defined as the ratio of the radius of the cylinder to the radius of the polyethylene insert. The fully conformal case consisted of equal radii of 20.193 mm with a conformity ratio of 1. The almost conformal case had the radius of polyethylene insert increased by 0.076 mm similar to the Agility® ankle implant, giving a conformity ratio of 0.996. The polyethylene was modeled as 3 mm thick, which is the minimum thickness of the polyethylene in the sagittal plane. The width L=8.6 mm was calculated as the average width of the trapezoidal "Standard" implant. Surface to surface contact elements with no friction were placed between the rigid indentor and cylindrical polyethylene. The values of the contact parameters are given in Sections 4.3.1 and 4.3.1.1. A load of five times body weight[21, 115] of 68 kg was applied to the rigid indentor. The model used plane strain

conditions which were expected to prevail in the middle of the sagittal plane. A Young's modulus of 557 MPa was used, representing the linear part of the nonlinear material curve presented by DeHeer[157] (Table 5).

The results and behavior of the analytical solution were evaluated on the contact and von Mises stresses with varying Poisson's ratio. For fully conformal surfaces, (Figure 5.2) the analytical and FEM solution gave closely matching results. The contact pressure proved to be independent of Poisson's ratio. The von Mises stress, on the other hand, was strongly dependent on Poisson's ratio.

For almost conformal surfaces, the contact pressure from the analytical solution was predicted well for Poisson's ratios of 0 and 0.3 (Figure 5.3). For a Poisson's ratio of 0.46, the contact pressure calculated by the analytical solution was 7% higher at a smaller contact angles. Similar results were obtained for the von Mises stress. The results of the von Mises stress were almost identical for low Poisson's ratios. For a Poisson's ratio of 0.46, the maximum von Mises stress at $\theta=0^{\circ}$ from the analytical solution was lower by 20% than that of the FEM model.

The von Mises stress distribution in the cylindrical body was compared next. Nodal coordinates of the FEM model were transferred into MATLAB (*vget command) and Equations 12-14 were evaluated at these nodal points. Results were then transferred back to ANSYS (*vput command) for postprocessing. The distribution of the von Mises stress in both models throughout the profile was similar for lower Poisson's ratios (Figure 5.4). There was a slight difference in the stress distribution at the end of the contact

region. For a Poisson's ratio of 0.46, there was a significant difference not only in the magnitude but also in the distribution of the von Mises stress (Figure 5.5).

Finally, we examined the effect of polyethylene thickness on contact pressure. The results showed (Figure 5.6) that fully conformal surfaces did not benefit from increased thickness. For almost conformal surfaces, there was almost no change in contact pressure for a thickness greater than 4 mm.

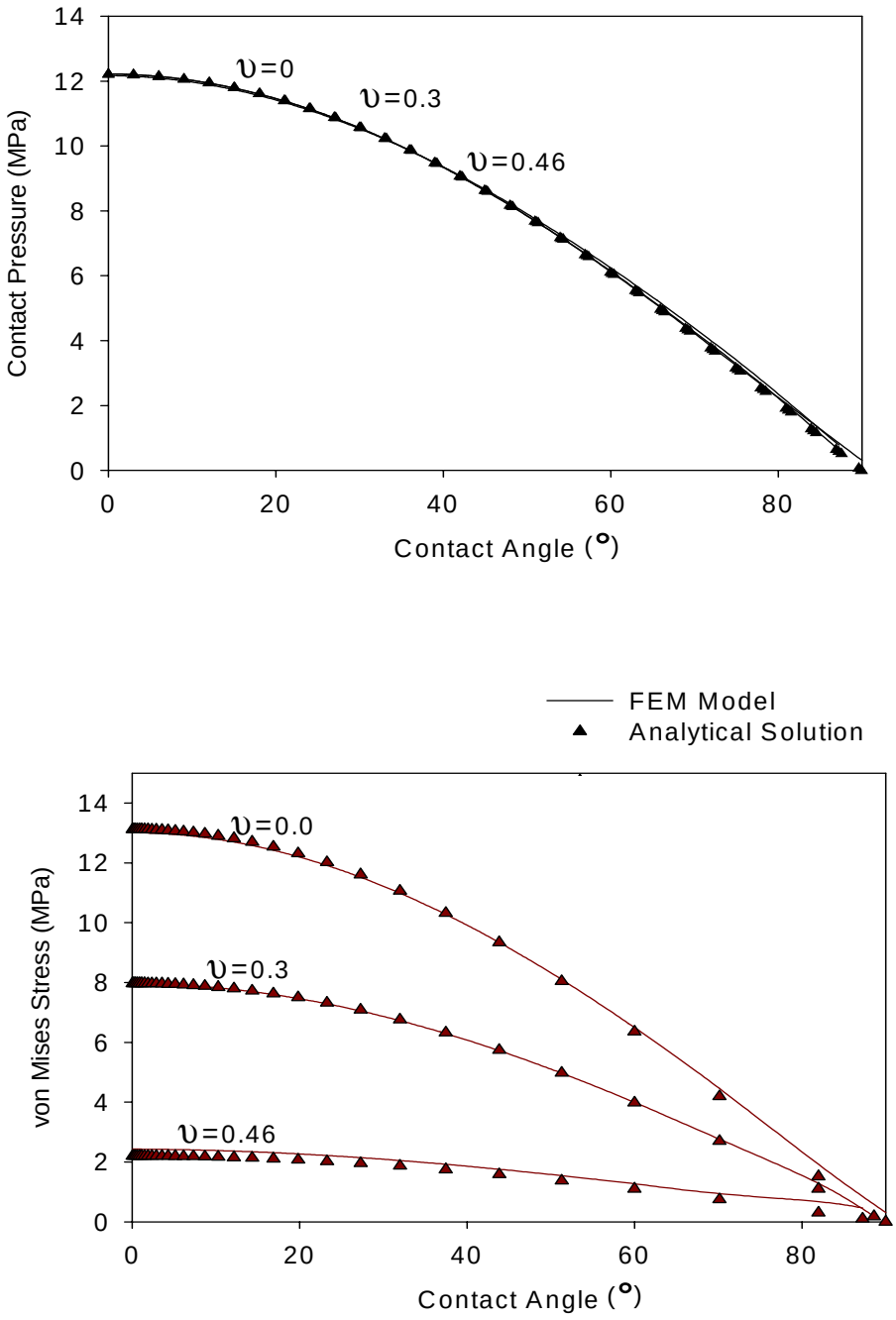

Figure 5.2 Contact pressure (top) and von Mises stress (bottom) as a function of the Poisson's ratio for fully conformal surfaces

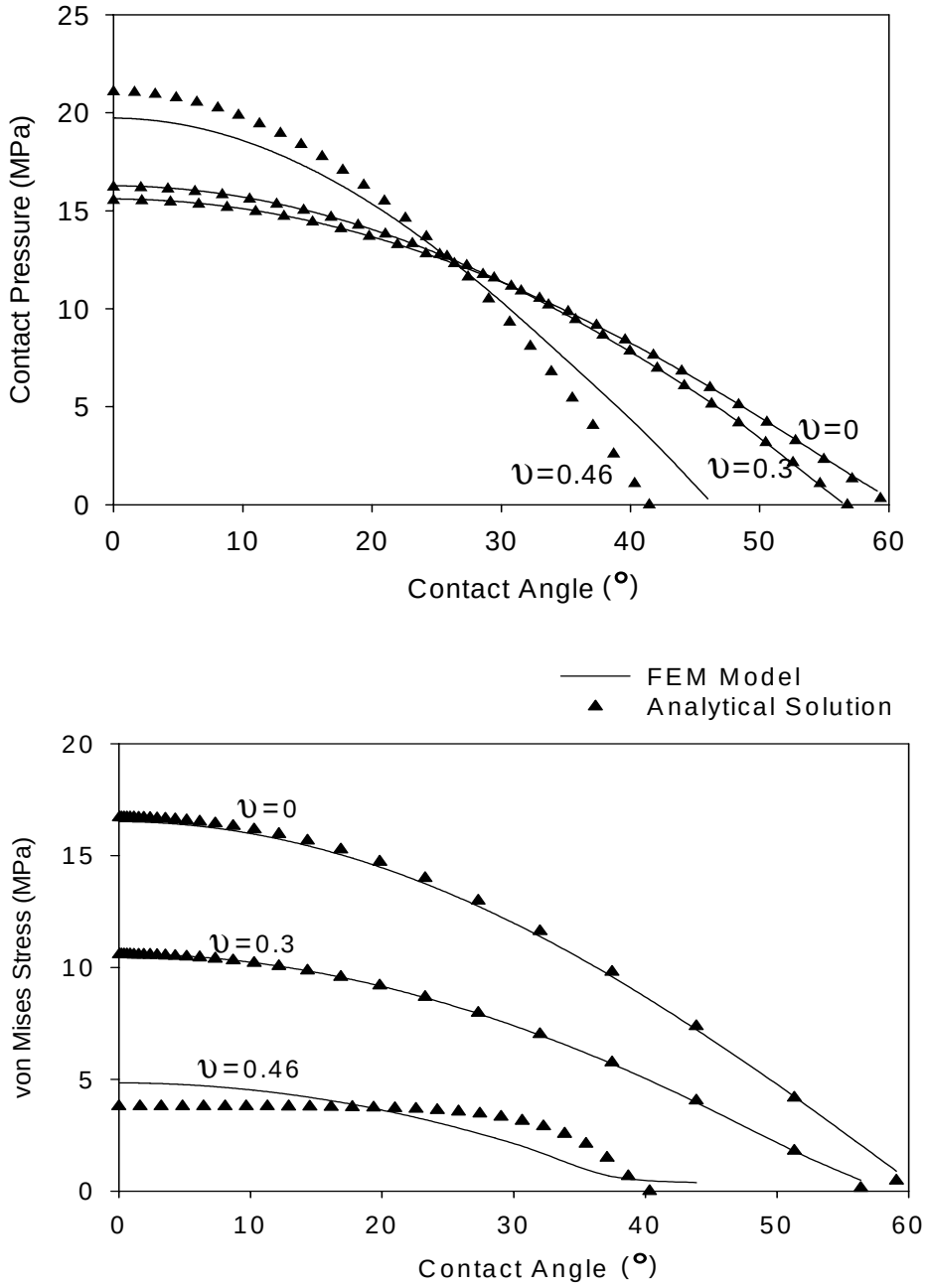

Figure 5.3 Contact pressure (top) and von Mises stress (bottom) as a function of the Poisson's ratio for almost conformal surfaces

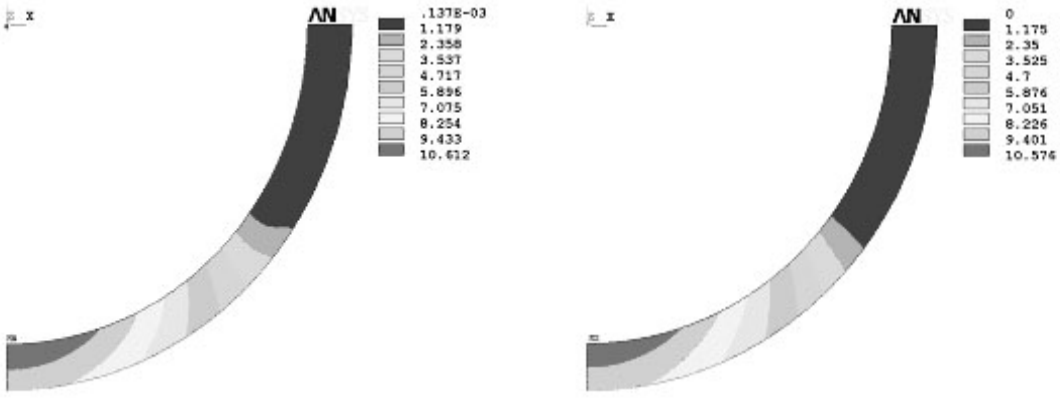

FEM Model Analytical Solution

Figure 5.4 von Mises stress for almost conformal surfaces and the Poisson's ratio of 0.3

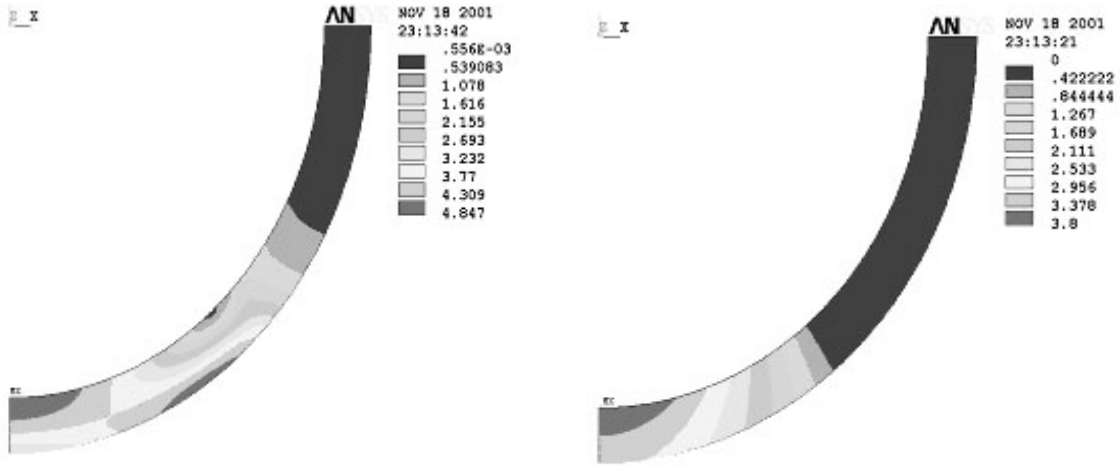

FEM Model Analytical Solution

Figure 5.5 von Mises stress for almost conformal surfaces and the Poisson's ratio of 0.46

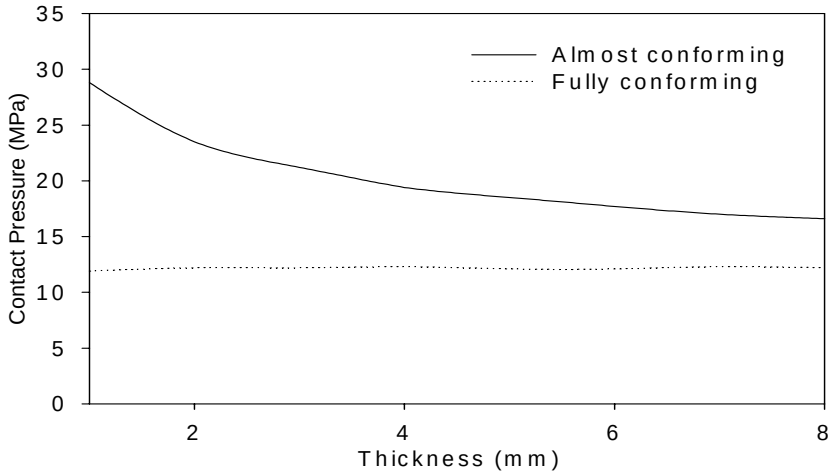

Figure 5.6 Dependence of the contact pressure on the thickness of the polyethylene insert. Results from analytical solution for the Poisson's ratio of 0.46

5.2 Discussion of Results of the Analytical Solution

The analytical solution of the indenting cylinder was compared with a two-dimensional FEM model for highly conformal surfaces. For the fully conformal surfaces, results matched closely for both the contact pressure and for the von Mises stress. It was evident that the contact pressure was not a function of Poisson's ratio. The von Mises stress decreased with increasing Poisson's ratio. Further investigation of other stress components revealed that the circumferential component of stress $\sigma_{\theta\theta}$ increased with increasing incompressibility (Figure 5.7). This in turn increased the longitudinal component of stress $\sigma_{zz.}$ However, the increase of these two components of stresses decreased the relative difference between principal stresses (increased the hydrostatic pressure) leading to a decrease of the von Mises stress (see Equation 20).

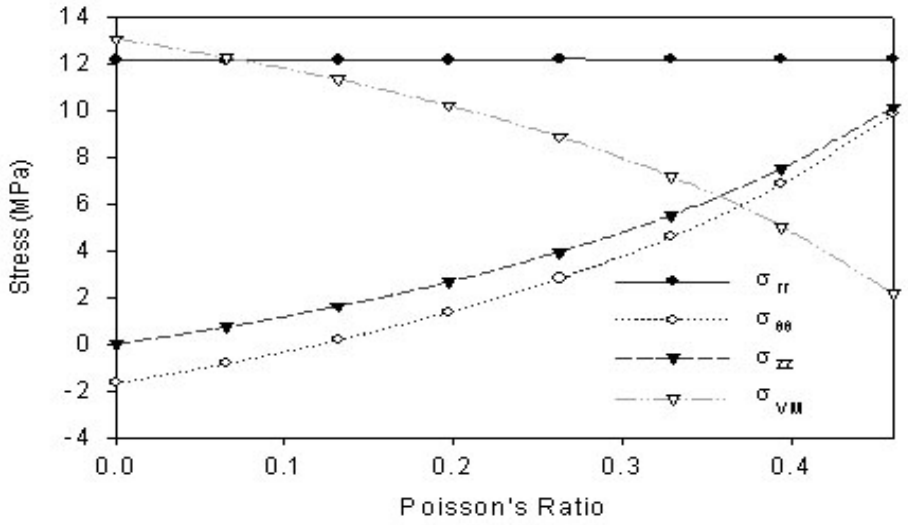

Figure 5.7 Components of stress for fully conformal surfaces from the analytical solution as a function of Poisson's ratio. The stress components are plotted with reversed signs to be consistent with notation that the contact pressure σ_{rr} be positive

For the almost conformal surfaces, the results of the contact pressure and von Mises stress matched well for Poisson's ratios of 0 and 0.3 (Figure 5.3). For the higher Poisson's ratio of 0.46, the peak contact pressure from the analytical solution was 7% higher than that of the FEM model. Similar results were obtained by Li et al.[158] who compared Bartel's[144] analytical solution of an indenting sphere (among other solutions) with a FEM model. On the other hand, the peak von Mises stress from the analytical solution was lower by 20%. The difference between the analytical solution and FEM model can be explained by the absence of the shear stresses that are neglected in the

analytical solution but become dominant in the FEM model (Figure 5.8). As stated by Li et al.[158] when Poisson's ratio approaches 0.5 and the material becomes incompressible, the shear stresses become dominant. However, as we saw in the case of fully conformal surfaces, the incompressibility itself does not directly increase shear stresses. This was proven by the fact that our analytical solution corresponded well to the FEM solution even for almost incompressible case of Poisson's ratio 0.46. Thus, the combined incompressibility with slight nonconformity caused the rise in shear stresses. As the conformity ratio decreased, the shear stresses became dominant for lower Poisson's ratios.

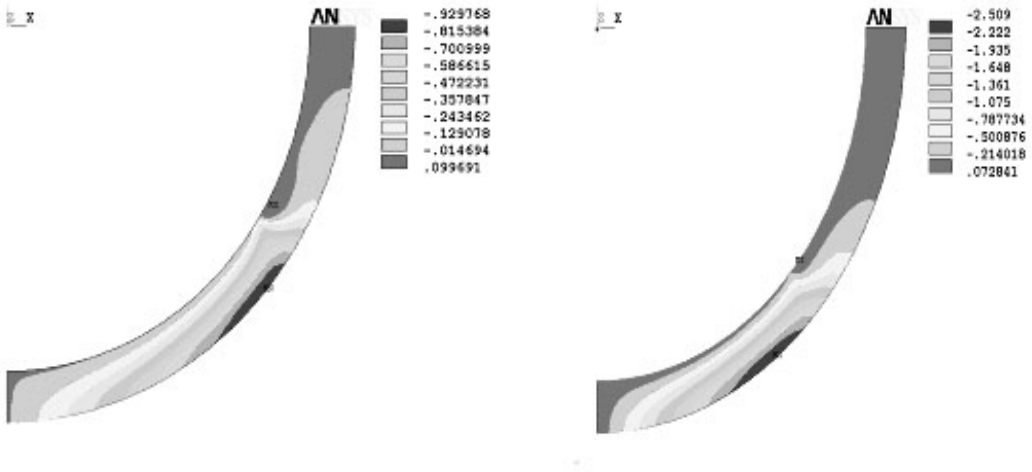

a, Poisson's ratio=0.3 b, Poisson's ratio=0.46

Figure 5.8 Shear stress from the FEM model for an almost conformal geometry for Poisson's ratios of 0.3 and 0.46

From Figure 5.3 (top), it follows that the rigid surface penetrates less into the elastic body as the material becomes less compressible, creating smaller contact areas

(angles) and higher contact stresses. The von Mises stress (Figure 5.3, bottom) showed a higher degree of dependence on the Poisson's ratio in comparison to the contact pressure. The distribution of the von Mises stress across the cross-section (Figure 5.4) was almost identical for both models, with the exception of the stresses at the end of the contact region. The stresses on the surface at the end of the contact region abruptly changed from a compressive contact pressure inside of the contact region to tensile on the free surface. These tensile stresses are not predicted by the elasticity solution.[144]

Similar to fully conformal surfaces, for almost conformal surfaces with higher Poisson's ratio, the contact pressure increased while the von Mises stress decreased. Unlike fully the conformal surfaces, all components of stress increase with increasing Poisson's ratio in almost conformal surfaces. The contact pressure was nearly constant for lower Poisson's ratios and increased slower than the other two stress components (Figure 5.9). As a result, even though the components of stresses grew in absolute value, the relative difference between them decreased, leading to the decreased von Mises stress.

The conformity ratio of the almost conformal surfaces was 0.996. It may seem that this small difference between the fully conformal and almost conformal surfaces should make little difference in the stresses. However, based on the results of Kuster et al.[132] the change of conformity ratio from 0.99 to 1* increased contact area by 135%. The analytical solution predicted that an implant made with the a clearance of 0.076 mm

---

* The contact area for conformity ratio 1 was calculated based on geometry. The contact area for conformity ratio of 0.99 was read from Figure 3 for 3000 N load

would experience a 72% higher contact pressure and von Mises stress in comparison to fully conformal surfaces. Another way of considering these results is that if the wear of articulating surfaces causes full conformity, then the contact pressure and the von Mises stress will decrease by 42%. It remains to be seen if similar results would be obtained from three-dimensional FEM model.

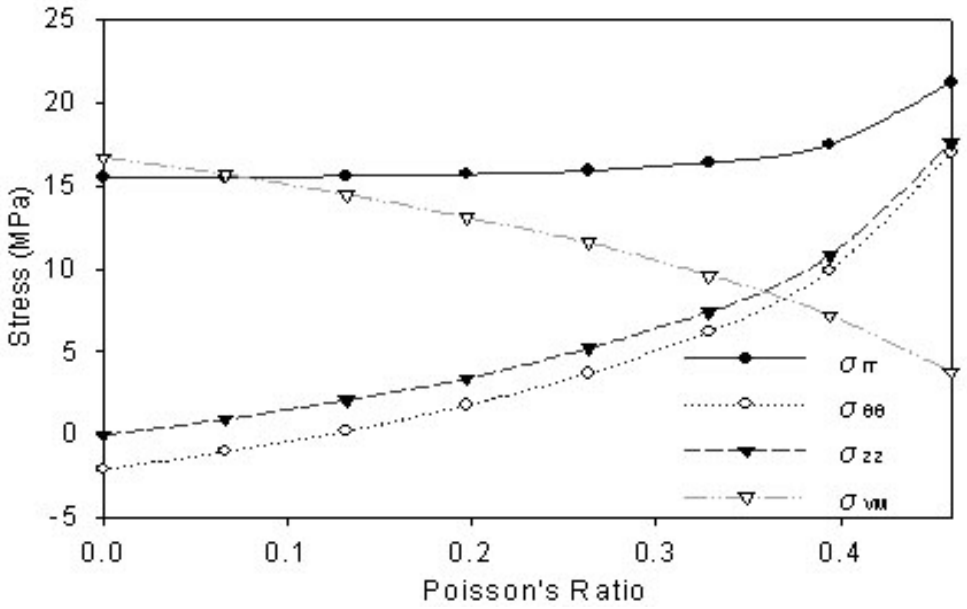

Figure 5.9 Components of stress for almost conformal surfaces from the analytical solution as a function of Poisson's ratio.

6.0 STRESS ANALYSIS OF THE UHMWPE INSERT

Two goals were determined for static stress analysis of the polyethylene inserts used in TAA. Firstly, we investigated the stresses in the polyethylene insert that arise from articulating with two different shapes of the talar component, the "Standard" and the "Modified". The "Standard" implant was also investigated at different dorsi-plantar flexion angles. For this study the talar component was rotated from 20 degrees plantar-flexion to 20 degrees dorsiflexion in increments of 10 degrees. Even though the forces loading the ankle change during gait, we decided to use a constant force of five times body weight to simulate stair climbing. The analysis was static. Secondly, we analyzed the effect of polyethylene component thickness on polyethylene stresses. To achieve these goals we used three different models. The first model was a three-dimensional (3-D) FEM model of the implants including bones. This model served as a benchmark for other models. The second model was the analytical solution of counterformal cylinders. The third model was a two-dimensional cross-sectional FEM model of the polyethylene insert. This technique has been frequently used for modeling behavior of polyethylene in knee implants[126, 128-130, 159-161] These two-dimensional models assume that plane strain conditions prevail. The main reason for including the two simplified models was to determine how these techniques compare to a three-dimensional model.

6.1 Three-Dimensional FEM Model

The 3-D model as described in Section 4.0 was adjusted for the calculation of stresses in the polyethylene insert. For the lower portion of the model below the UHMWPE insert only the top portion of the talar component was needed and talus was not included in the model. The talar component of the implant which is three orders of magnitude stiffer than the polyethylene insert was modeled with rigid contact elements and was fully constrained. Elasto-plastic material properties were used for the three- and two-dimensional FEM models unless otherwise stated. The model was run in two stages. First, the full model was analyzed with loads on the top of the tibia and fibula as described in Section 4.5. The size of polyethylene elements in the contacting areas and the talar rigid surface were 1 mm and 0.5 mm, respectively, resulting in a total of 41,597 elements. From experience and from the literature review, it was expected that the model had to be refined for results to converge. Because refining the full model would increase the solution time prohibitively a submodeling technique was employed. The submodeling FEM technique refines the areas of interest in the coarse model while the rest of the coarse model is deleted. The loads are transferred to the submodel from the coarse model by displacements determined from areas at the boundary between the submodel and the coarse model. This technique is also called the cut boundary displacement method. It works under the assumption that the cut boundaries are far away from the areas of interest. The areas along the bone-implant interface were selected for cut boundary conditions (Figure 6.1).

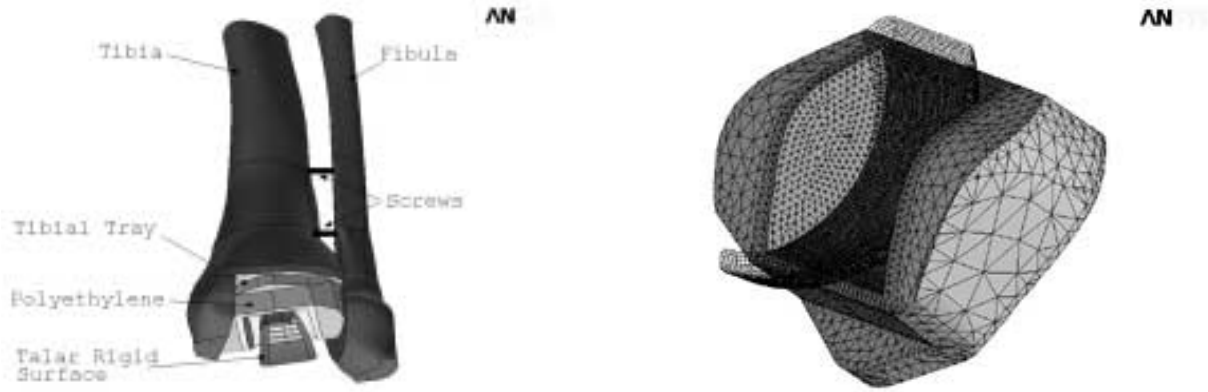

Figure 6.1 Full solid model (right) and FEM submodel (left) for calculating stresses in the UHWMPE insert

The convergence study was performed on the submodel. The size of elements in the talar component was held constant at 0.25 mm while the element size in the articulating surfaces of the polyethylene was varied. Change from an element size of 2 mm to an element size of 0.5 mm caused change in the stresses in the sagittal plane of less than 1% (Table 7). The stresses at the lateral and medial edges changed less than 10%. It should be noted that the stresses at the edges for an element size of 2 mm were not pronounced and almost equal to the stresses in the sagittal plane (Table 7). An element size of 0.5 mm for polyethylene and of 0.25 mm for the talar rigid surface were used in our submodel and corresponded to the converged size of elements used in a 3-D FEM model by Bartel et al.[127] and to the converged 2-D FEM model by Rawlinson et al.[154] This mesh resulted in 56,119 elements and 75,090 nodes. Even though the number of nodes in the submodel increased, the actual solution time decreased from 29 hours for the full model to 18 hours for the submodel. This was due to the fact that the submodel

was displacement driven, requiring fewer iterations than a force driven contact problem (see Section 4.3.1.1).

Table 7 Convergence study on the submodel of the "Standard" talar component. The size of the talar rigid surface was kept constant at 0.25 mm

Element size	Edges		Sagittal plane	
	VM* (MPa)	CP** (MPa)	VM* (MPa)	CP** (MPa)
2	11.9***	25.2***	11.0	23.2
1	13.9	41.6	11.8	25.0
0.5	12.5	38.4	11.9	25.3

*VM- von Mises stress
**CP – Contact pressure
*** The stress concentrations at the edges were not pronounced

6.1.1 Two-Dimensional Cross-Sectional FEM Model

A two-dimensional FEM model of the polyethylene cross-section (Figure 6.2) in a plane strain condition was created to see if this approach provided results comparable to the three-dimensional FEM model. The parameters of the model were the same as those used in the 2-D FEM model for validation of the analytical solution (Section 5.1). The total force applied to the 3-D FEM model was divided by 8.6 mm for the "Standard" talar component and by 15 mm for the "Modified" talar component. These are the average widths of the contacting surfaces of the talar components without the radii of the medial and lateral edges.

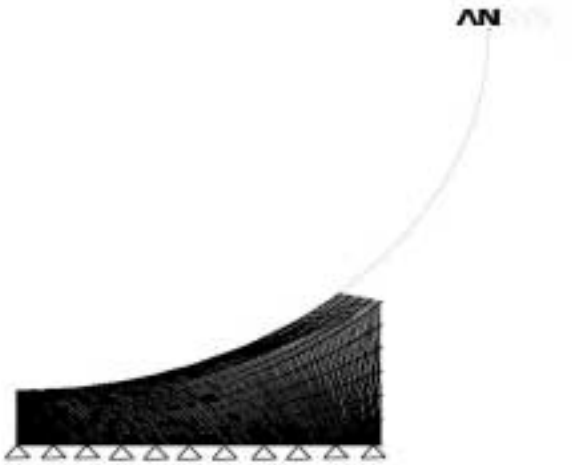

Figure 6.2 Two-dimensional cross-sectional FEM model of the polyethylene insert

6.2 Results of the UHMWPE Stress Analysis

This section will be present the results for the polyethylene component stress analysis for the "Standard" and the "Modified" shapes of the talar component (Figure 4.4). The graphs in the frontal and sagittal planes passed through geometrical center of the polyethylene insert. The results in the sagittal plane were gathered from three different models to examine if any of the two-dimensional models (analytical solution and the cross-sectional 2-D FEM model) would be a good approximation of the three-dimensional model. The data from frontal plane were obtained only from the 3-D FEM model. The models were labeled in the following way:

1. Analytical solution- Analytical solution of two counterformal cylinders
2. 3-D FEM -Three-dimensional model of the implants and bones
3. 2-D FEM - Two-dimensional model of the three-dimensional model

As expected for conformal surfaces, the largest von Mises stress in all of the models was on the surface. Thus, all the results, unless stated otherwise, are taken from the articular surface of the polyethylene insert.

The difference between modeling the polyethylene as an elastic or elasto-plastic material for the "Standard" model was investigated first (Figure 6.3). The frontal plane was selected for demonstration of the results because it can show the stresses due to the lateral and medial edges of the talar components. It was determined that the contact pressure was predominantly a function of the linear material properties. The peak von Mises stress, in the middle of the sagittal plane, decreased from 13 MPa to 11.8 MPa when the nonlinear material properties were used. The decrease was relatively small since the stresses were only slightly above the yield strength of 10.86 MPa. The von Mises stress at the edges decreased more significantly. A three-dimensional pressure and von Mises stress distribution is presented on Figure 6.4.

The talar component of the "Standard" implant is much wider anteriorly than posteriorly, creating an asymmetric distribution of results from the 3-D FEM model (Figure 6.5). This could not be modeled with the two-dimensional models. The contact pressure at the center of contact was over-predicted by the 2-D FEM model by 24% and under predicted by the analytical solution by 20%. The contact angle was predicted much better by the 2-D FEM model than by the analytical solution. The von Mises stress was predicted very well by the 2-D FEM and very poorly by the analytical solution, underestimating the 3-D FEM model by 70%. The elasto-plastic material properties helped to smooth out both the contact pressure and von Mises stress of the 3-D model.

The “Modified” talar component is almost as wide posteriorly as anteriorly creating more symmetrical results in the sagittal plane. For this reason only results from one half of the plane are plotted (Figure 6.6). The contact pressure and von Mises stress are underestimated by the 2-D FEM model. The analytical solution predicted contact pressure fairly well but the von Mises stress was again underestimated by 70%.

The two talar component designs were compared in the frontal plane (Figure 6.7). The enlarged contact area of the “Modified” implant decreased the average contact pressure and the average von Mises stress by 21%. The average von Mises stress even fell below the yield limit of 10.86 MPa in the polyethylene articulating with the “Modified” talar component. However, the peak stresses at the edges remained relatively unchanged.

The differences in the von Mises stress distribution through the thickness of the polyethylene are shown in Figure 6.8. The “Modified” talar component caused yielding of the polyethylene only at the edges. The “Standard” talar component yielded the polyethylene up to the half of the thickness in the middle and through the thickness along the edges. The maximum von Mises stress was on the surfaces for both of the talar components.

Finally, the stresses in the polyethylene in the “Standard” talar model were examined at different plantar-dorsi flexion angles (Figure 6.9). Since the talar component is narrower posteriorly, this led to an increase of the contact area as the foot goes from plantar to dorsiflexion. The only significant change in results was in a contact pressure decrease at the edges.

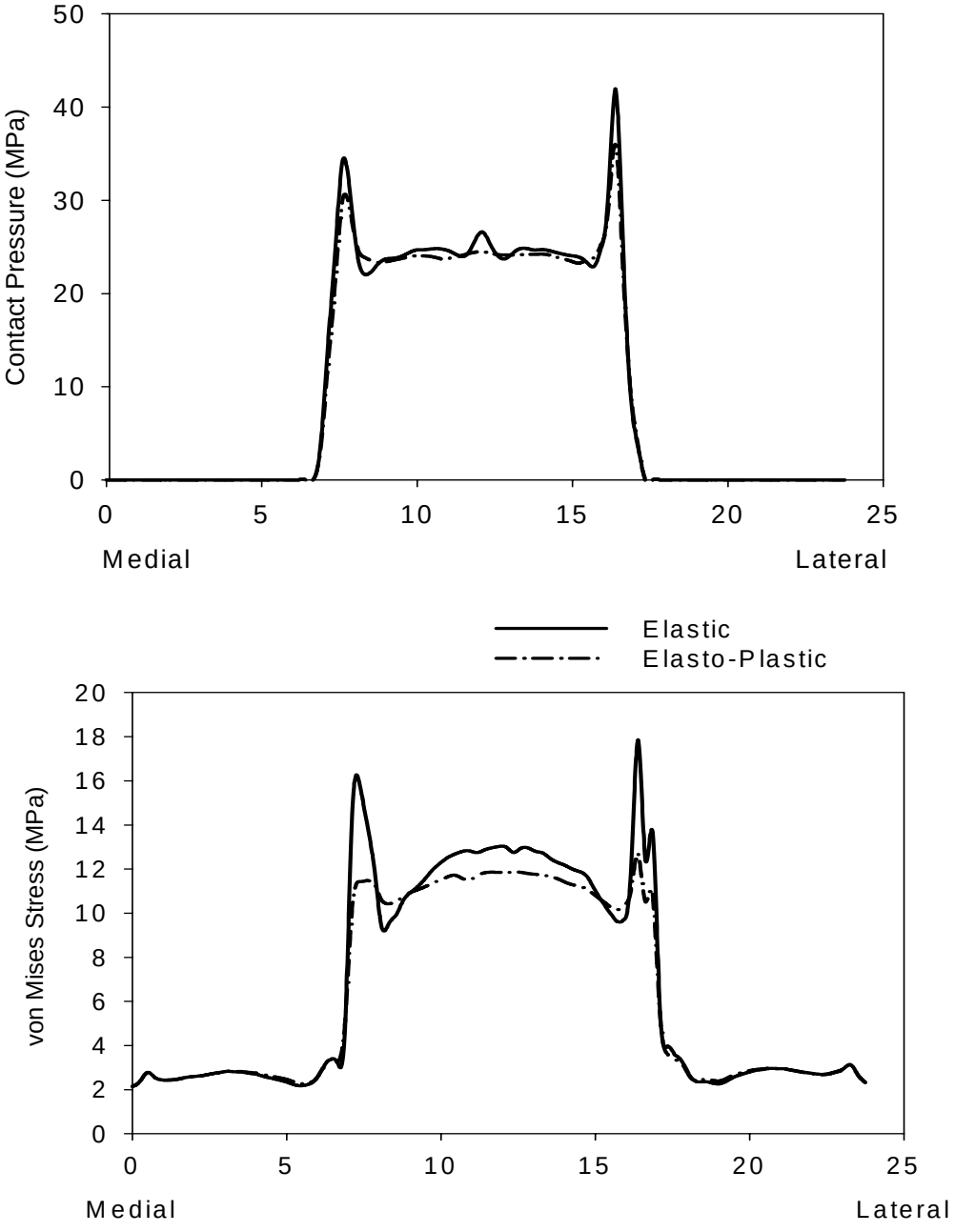

Figure 6.3 Contact pressure (top) and von Mises stress (bottom) on the surface of the polyethylene for "Standard" talar component. Frontal plane

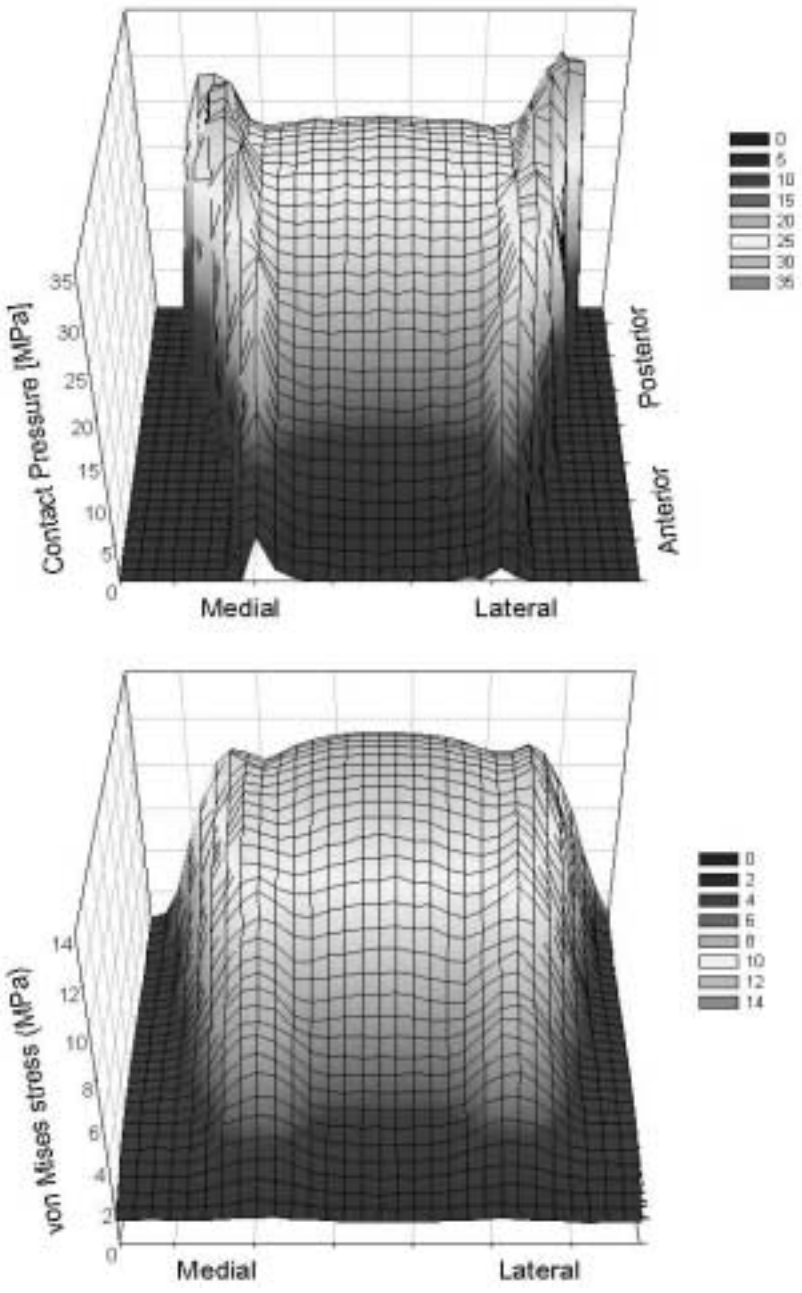

Figure 6.4 Three-dimensional distribution of the contact pressure (top) and von Mises stress (bottom) on the surface of the polyethylene. “Standard” talar component

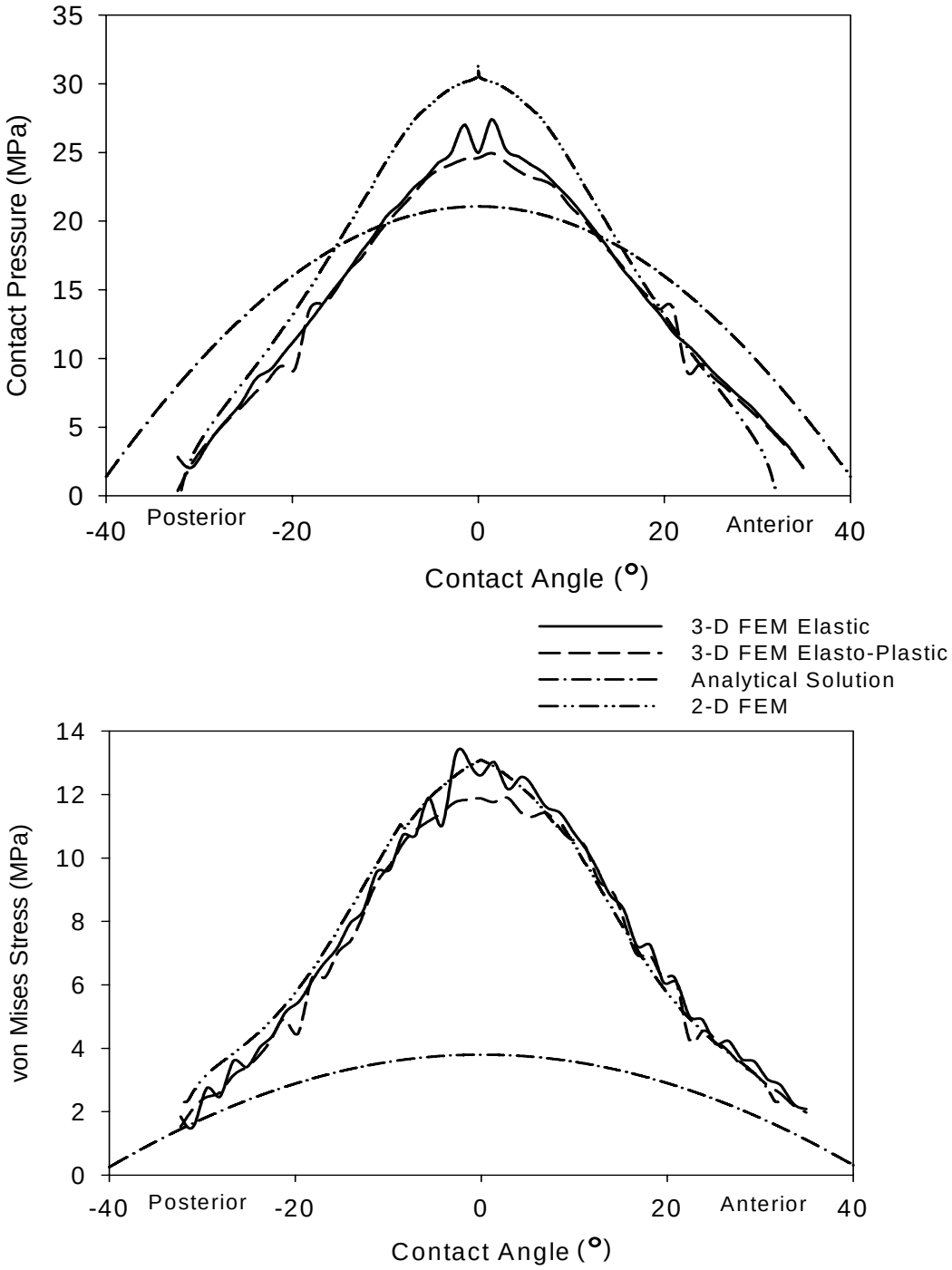

Figure 6.5 Contact pressure (top) and von Mises stress (bottom) on the surface of the polyethylene insert with the "Standard" talar component in the sagittal plane

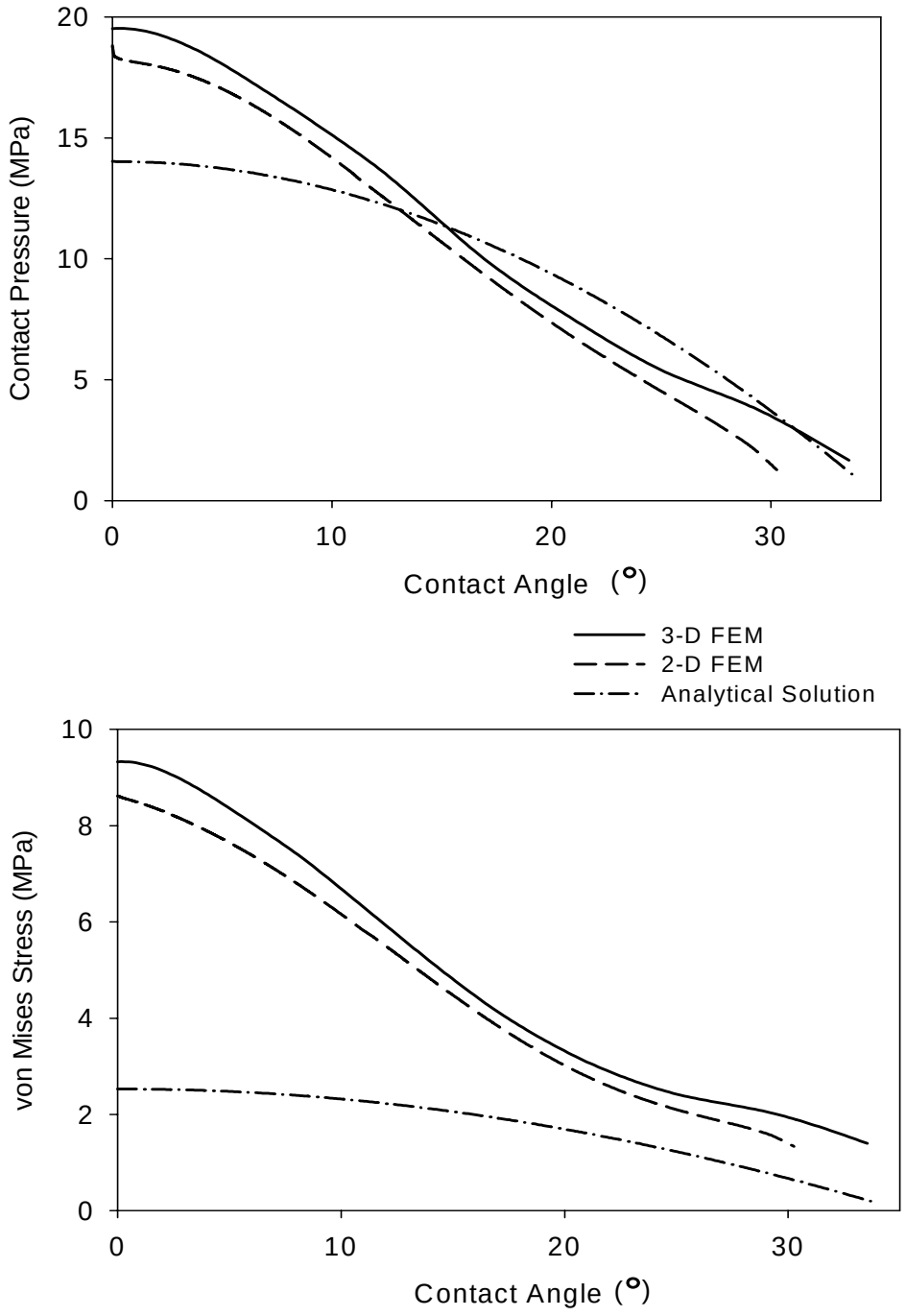

Figure 6.6 Contact pressure (top) and von Mises stress (bottom) on the surface of the polyethylene insert with the "Modified" talar component in the Sagittal plane

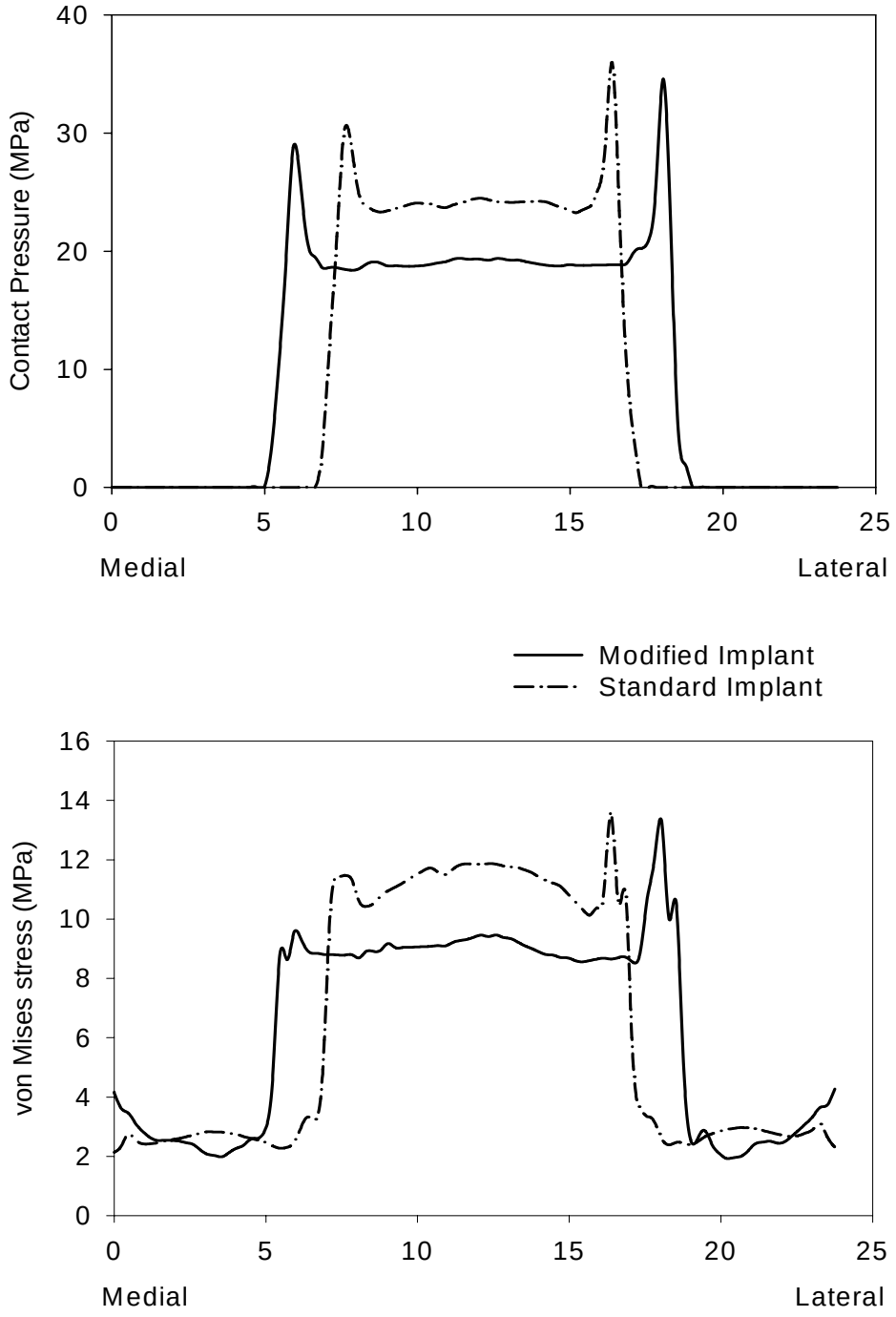

Figure 6.7 Contact pressure (top) and von Mises stress (bottom) on the surface of the polyethylene insert with the "Standard" and the "Modified" shapes in the frontal plane

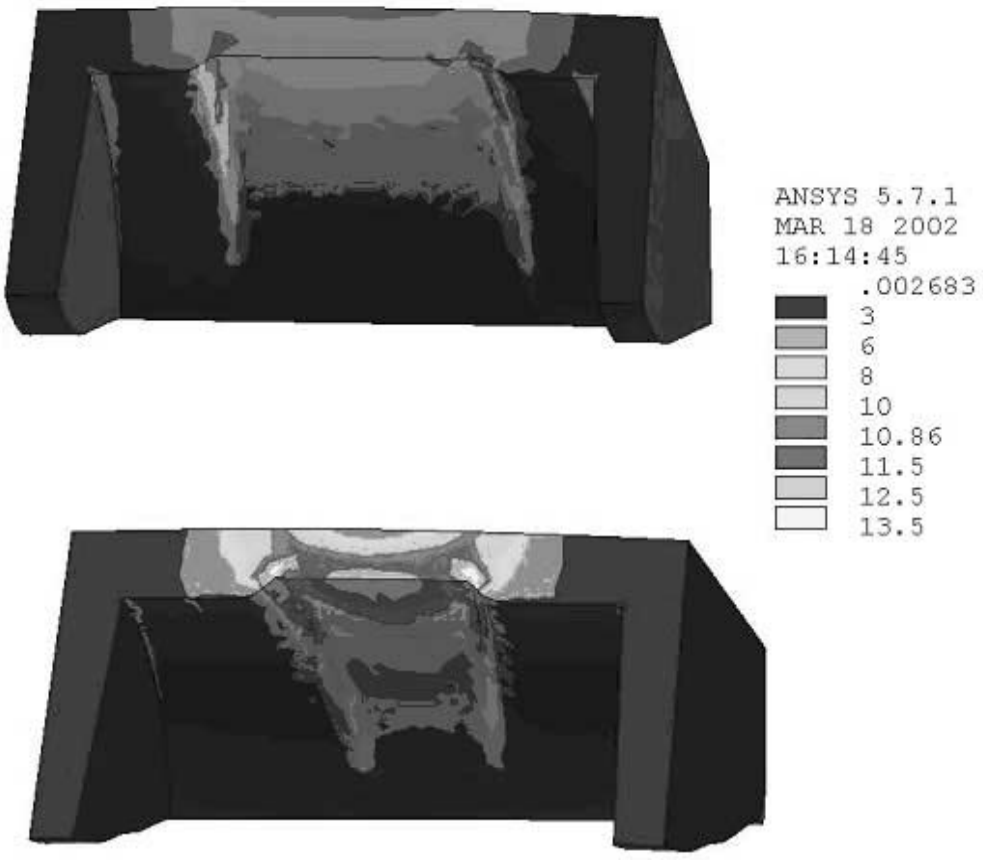

Figure 6.8 Through the thickness view of the von Mises stress of the polyethylene insert articulating with “Modified” (top) and “Standard” (bottom) talar component.

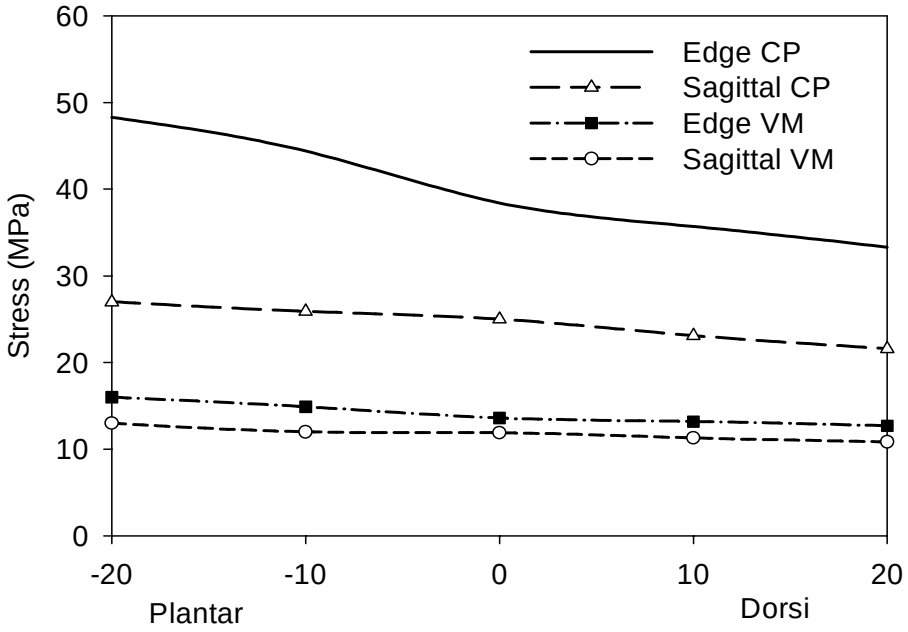

Figure 6.9 Peak contact pressure (CP) and von Mises stress (VM) at the edges and in the middle of the sagittal plane for the "Standard" implant at different dorsi-plantar flexion angles

6.2.1 Results of the Effect of the Polyethylene Thickness

"Standard" talar component. The 3-D FEM model predicted a sharp decrease of contact pressure for the first two additional millimeters of the thickness (Figure 6.10, top). The contact pressure decreased from 25 MPa to 13 MPa. An additional increase of thickness would not greatly reduce the contact pressure. The 2-D models also predicted decreasing contact pressure with increased thickness but with less decrease. The von Mises stress in the 2-D FEM model agreed with the 3-D FEM model only for the thinner

polyethylene insert. The 3-D model predicted a sharp decrease of von Mises stress while the 2-D models indicated a slight increase of von Mises stress with increased thickness.

"Modified" talar component. The decrease of contact pressure with increasing thickness was not as large as it was for the "Standard" talar component (Figure 6.11). The contact pressure of the 2-D FEM model matched the results of the 3-D FEM model very closely, both predicting contact pressure drop of 25% if the thickness increased to 8 mm. The analytical solution under-predicted contact pressure consistently by about 5 MPa. This time, the increase of von Mises stress was also predicted by the 3-D model but the increase was not as sharp as predicted by the 2-D FEM model.

Finally, we studied the effect of increased polyethylene thickness on polyethylene stresses due to the lateral and medial edges of the two talar components (Figure 6.12). These results could be obtained only from the 3-D FEM model. The highest reported value at the edge (either lateral or medial edge) from nodal solution was recorded. For comparison we also included curves of von Mises stress and contact pressure from the sagittal plane. Stresses at the edge had the same tendency as stresses in the sagittal plane. There is an apparently wider variation between the values at the edges and the average stress in the middle for the "Modified" talar component than for the "Standard" talar component. For the "Modified" implant, the contact pressure on the edge was on average 20 MPa higher than contact pressure in the sagittal plane while for the "Standard" talar component it was only 17 MPa. Similarly for von Mises stress, the stresses at the edge of the "Modified" implant were 4.5 MPa higher than the sagittal stress, while in the "Standard" implant edge stresses were higher on average by 3.6 MPa .

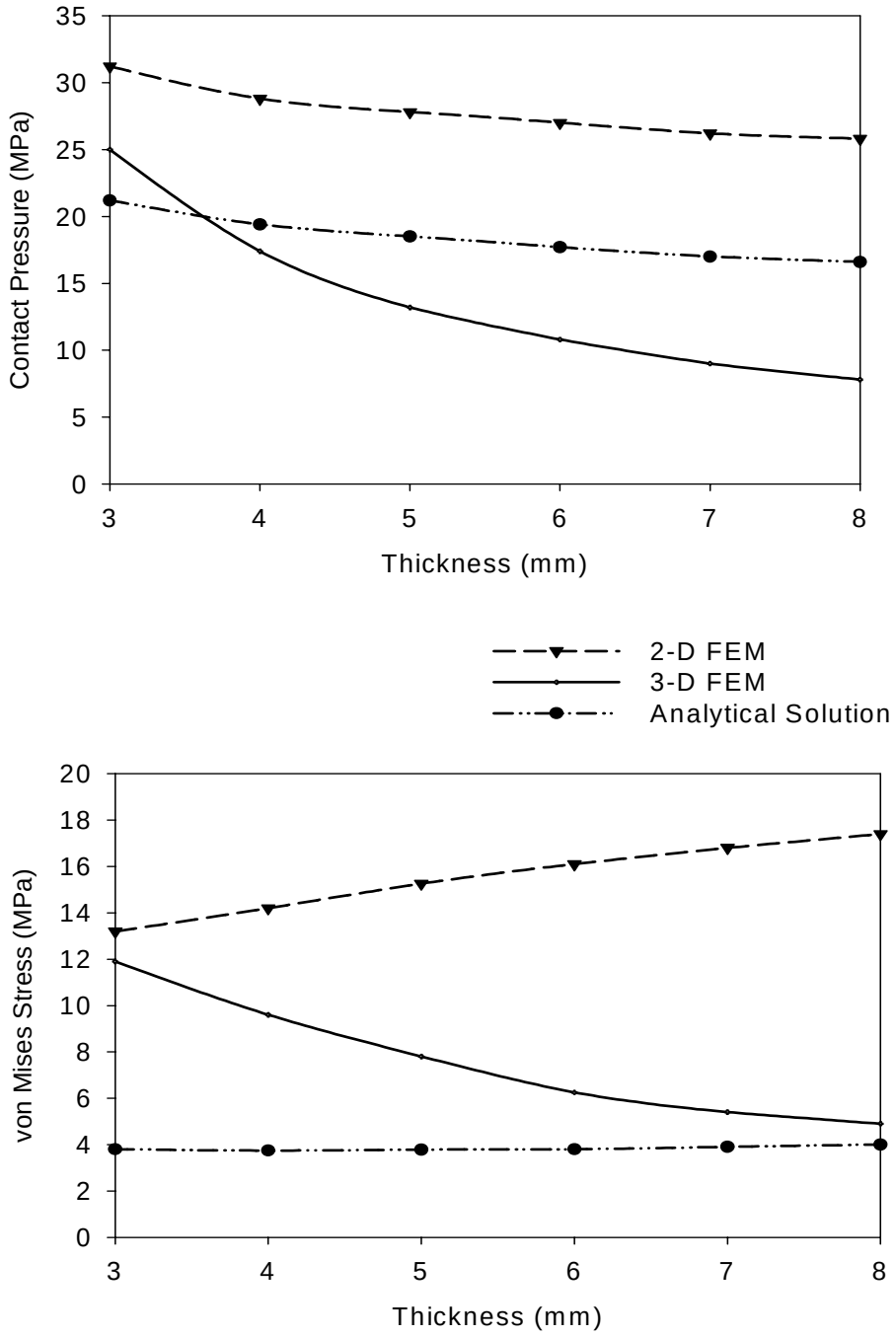

Figure 6.10 Contact Pressure (top) and von Mises stress (bottom) of the polyethylene insert articulating with the "Standard" talar component

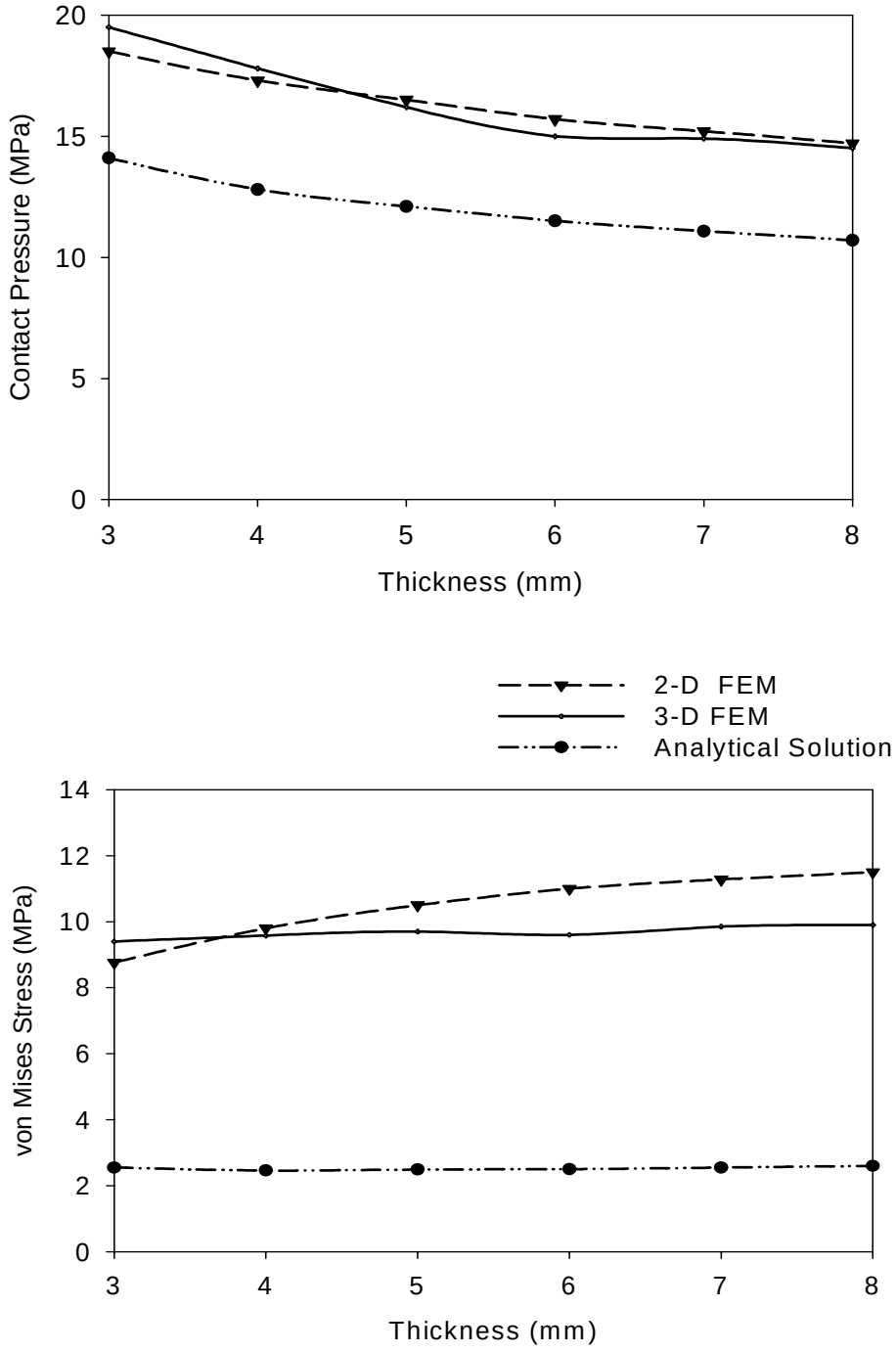

Figure 6.11 Contact Pressure (top) and von Mises stress (bottom) of the polyethylene insert articulating with the "Modified" talar component

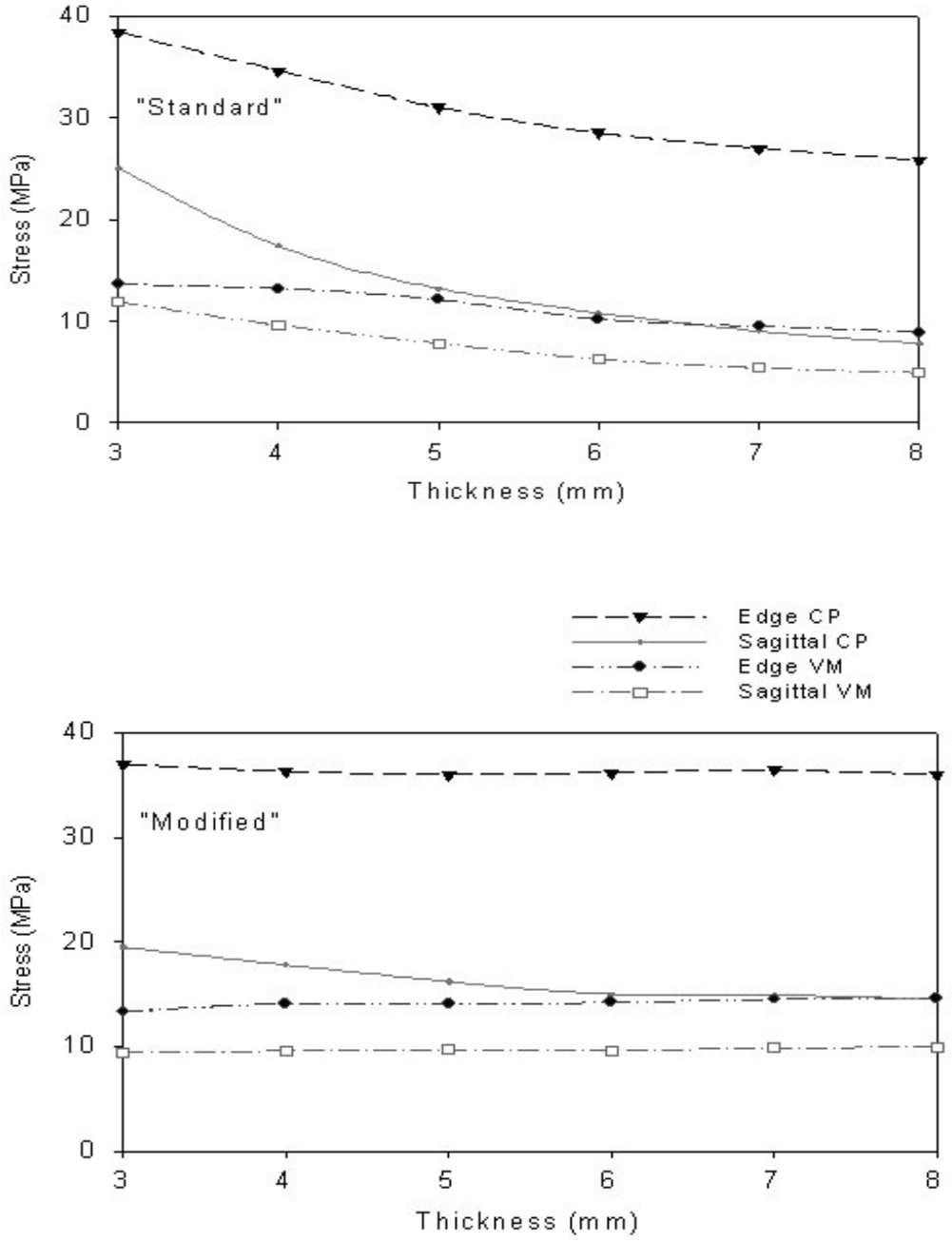

Figure 6.12 Peak contact pressure (CP) and von Mises stress (VM) at the edges and in the middle of the sagittal plane of the polyethylene for the two shapes of the talar implant from the 3-D FEM model

6.3 Discussion of Results

A stress analysis of the polyethylene insert of ankle implants due to two different talar component designs was performed. The ankle implant employed in the study is almost congruent in the sagittal plane and flat-on-flat with round edges in the frontal plane. Surface damage in the articulating surfaces of implants has been related to contact pressure. However, contact pressure is insufficient in explaining particular modes of failure. The conformal geometries of hip implants show polished surfaces which indicate a combination of abrasive wear and fatigue wear mechanisms. The fatigue mechanism is driven predominantly by pitting in which cracks start and propagate from the surface. The cause of the origin and propagation of these surface cracks in conformal geometries is cyclic tensile-compressive stress at the edges[139] and residual tensile stresses due to plastic deformation.[126] It was shown[134] that for monotonic loading as in our study, the von Mises failure criteria performed well for predicting elasto-plastic behavior of the polyethylene. Moreover, asymmetric failure criteria were not needed because the polyethylene, unlike cancellous bone, has the same true stress-strain behavior in tension as in compression.

As expected for conformal geometries, the von Mises stress for both of the talar components was on the surface of the polyethylene (Figure 6.8). The “Standard” talar component caused plastic deformation through half of the thickness across the center of the talar component. The plasticity at the edges spread through the entire thickness. The “Modified” talar component induced plasticity only along the edges (Figure 6.8, Figure 6.7). The “Standard” implant could potentially wear the polyethylene in a way similar to

of knee components[162] The curved-on-flat experiment induced plasticity in the center and at the edges resulting in extensive pitting and cracking at the edges and cracking in the center. The "Modified" component design seemed to correlate to the flat-on-flat experimental wear geometry[162] with the potential of decreased wear in the center in later stages of in vivo use and localized cracks to the edge.

Widening the talar component from an average of 8.6 mm to an average of 15 mm increased the contact area in the neutral position by 28%. This led to a decrease of both the contact pressure and the von Mises stress by 21%. However, the contact pressure at the edges stayed relatively unchanged. The stress concentrations at the edges can be explained as follows: the particles in the center of contacting areas are surrounded by other particles and experience the same displacements. At the edge the same displacement has to be achieved by load from only one side (the inside). This results in increased pressure at the edge and leads to an increased width of the contact area. The increased width of the contact area is demonstrated from Figure 6.8 in which the contact pressure (represented by von Mises stress on this Figure) extends below the contact area of the cylindrical body in a leg-like shape. Increasing the radius of the indenting talar component will not eliminate the edge stress concentrations. A significant reduction of the stress concentrations is possible by barreling[148] or crowning[153] of the profile in the frontal plane. This is difficult to manufacture and works only for the design load. One other possibility of eliminating the edge stress concentrations would be to make the profile in the frontal plane to be curved-on-curved type.[154] This would, however, restrict the motion of the implant to the sagittal plane, making the implant highly constrained.

A stress analysis of various knee implants[127] found contact pressures between 40-62 MPa and von Mises stresses of 23-28 MPa for a load of 3000 N. The contact pressure and maximum shear stress of hip implants[139] were found to be 15-18 MPa and 5-7 MPa respectively. Based on these representative samples, the magnitudes of the average contact pressure and von Mises stress of the ankle implant are closer to the values found in conformal hip implants than to the values of nonconformal knee implants. The stresses at the edge are lower than those found in most of the knee implants. In our study, the von Mises stress reached between 9-12 MPa in the middle of the sagittal plane and 13.6 MPa along the edges. The contact pressure in the middle of the sagittal plane was between 20-25 MPa and reached 35 MPa along the edges. The stress at the edge corresponds to strain of 0.03 which would induce plastic deformation of the amorphous phase (Section 3.4.1). Macroscopic yielding, in which lamellae undergo irrecoverable plastic deformation, does not occur until the true strain reaches 0.17.

Even though the increased width decreased stresses in the polyethylene, there are some negative aspects of the increased width. Increased width decreases the internal/external rotation and inversion/eversion. Historically, wide implants have had a tendency to loosen due stresses from over-constraints and are not recommended for use.[163] Moreover, experiments by Wang et al.[141] demonstrated that the wear rate actually increased in wider cylinders. They proposed that starved lubrication condition was dominating the wear mechanism in the articulating surfaces.

The thickness of the polyethylene has been shown to influence the contact pressure between the articulating surfaces.[139, 144] While there is only a slight reduction in

contact pressure in conformal surfaces, nonconformal surfaces will benefit from a significant lowering of contact pressure due to the increased polyethylene thickness. We investigated the effect of increased polyethylene component thickness on the contact pressure and the von Mises stress. There is a general belief that the von Mises stress will increase with increased contact pressure (and vice versa). However, as we saw when we validated the analytical solution (Section 5.2) this is not always true. We showed that with increasing Poisson's ratio the contact pressure increased while the von Mises stress decreased (Figure 5.9). Similarly, this relationship was observed for increased thickness using two-dimensional models (Figure 6.10 and Figure 6.11). According to these models, the contact pressure would decrease with increased thickness of the polyethylene while the von Mises stress would increase. This trend was observed for both talar components using the two-dimensional models. The explanation of this phenomenon is similar to the explanation provided in the analysis of the stresses due to the change of Poisson's ratio (Section 5.2): with increasing thickness the contact pressure, circumferential and longitudinal components of stress decrease. However, the relative difference between these stresses increases, leading to increased von Mises stress. The results of the 2-D FEM model closely matched results of the 3-D FEM model for the "Modified" implant but there was a quantitative difference between the results for the "Standard" model (Figure 6.10). The von Mises stress from the 3-D FEM model showed the opposite trend with stresses decreasing with thickness. The difference in predictions of the 2-D and 3-D models was due to violation the plane strain conditions. That is, the "Standard" talar component of an average width of 8.6 mm was not wide enough to induce plane strain

conditions. The violation of plane strain conditions was investigated in both of the models for two polyethylene thicknesses. The smaller the difference between the minimum and maximum values of the longitudinal strain the more the plane strain conditions were satisfied (Figure 6.13). The variation of the longitudinal strain was much larger in the “Standard” talar component model than in the “Modified” talar component implant. The condition of plane strain is likely to be violated in the “Modified” talar for thickness of more than 5 mm (Figure 6.11 von Mises stress). These results indicate that there is a certain ratio of the width of the cylinder and thickness of the polyethylene for which the assumption of plane strain conditions are not satisfied and thus simplified 2-D models in plane strain conditions should not be used. Otherwise, the results from 2-D models may provide results that are qualitatively and quantitatively different from a 3-D model. Therefore, we do not recommend 2-D models for analyzing knee component implant designs unless the knee implant design is wide and fully conformal in the frontal plane.

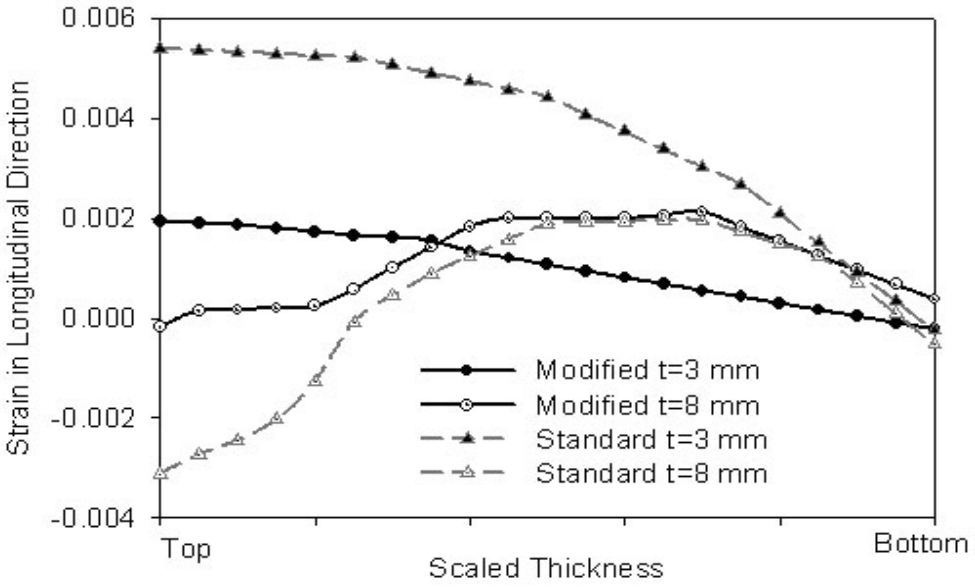

Figure 6.13 Variation of strain in longitudinal direction. Variation from zero indicates that the plane strain conditions were not satisfied

Based on the 3-D FEM model, the most significant relief of both the contact pressure and von Mises stress was achieved with a thickness of 5 mm. The contact pressure decreased by 47% and von Mises stress decreased by 34% compared to 3 mm thick polyethylene (Figure 6.10). A similar decrease of contact pressure was obtained in analysis of nonconformal knee implants.[139, 144] This may suggest that even though the "Standard" talar component is conformal in the sagittal plane, the narrow width in the frontal plane makes it behave as a nonconformal implant. The "Modified" implant, on the other hand, behaved as expected from conformal surfaces, e.g., increased thickness led to

only a slight decrease of contact pressure. The von Mises stress remained relatively unchanged.

The performance of the two 2-D models was compared with the 3-D FEM model. The maximum possible contact angle calculated from the geometry was 43 degrees. The analytical solution predicted a contact angle of 44 degrees, thus no modification for calculating of θ_{max} was necessary. The cylinder in the analytical solution was constrained along the outside radius. This proved to be much stiffer than the real geometry of the implant. As seen from Figure 6.2, the side of the polyethylene insert was not constrained. When the load is applied to the rigid indentor the side can displace resulting in smaller contact angle and higher contact pressure (Figure 6.5). The shape of the cross-section proved to be even more important for calculation of the von Mises stress. The von Mises stress from the analytical solution grossly under-predicted the results of both the 2-D FEM model and the 3-D FEM model. Adjusting the results of the analytical solution to account for elasto-plastic material properties would not change the contact pressure and would decrease the von Mises stress which was already low compared to the other models. This conclusion was drawn based on results of Figure 6.3 where we showed that the contact pressure was primarily a function of elastic properties[164] and was not very sensitive to elasto-plastic material properties.[154]

In a recent paper[154], a new analytical solution was proposed for investigation of contact pressure at the edges of knee implants in the frontal plane. It was stated that a 3-D FEM model would be necessary to investigate "effects of sagittal conformity, component thickness and tibial width" on stresses at the edges. Our FEM study can provide answers

to some of these questions, namely, how the stresses on the edge are effected by polyethylene thickness and by the width of the talar component. As stated earlier, a wider implant decreased stresses in the sagittal plane, however, the peak stresses on the edge were relatively unchanged. This indicates that an increased width increases stresses concentrations at the edges (Figure 6.7). The increased thickness kept the ratio of stresses in the sagittal plane to stresses at the edge approximately constant (Figure 6.12). Moreover, the stresses on the edge followed the tendency of stresses in the sagittal plane.

7.0 ANALYSIS OF STRESSES IN THE TALUS

A design modification of talar component of the Agility® ankle implant has recently been proposed. The original talar component, labeled "Standard" in our study, narrowed posteriorly to mimic the natural shape of the talus (Figure 4.4). To minimize posterior subsidence into the talus, the interface area between the implant and the talus was increased by adding a rectangular base. This talar component was labeled "Modified" in our study. The main focus of this part of the study was to investigate how this revision changed stresses and strains in the talus. Moreover, the "Standard" model was analyzed in dorsi-plantar flexion to investigate the change of stresses and strains during gait.

Based on the initial analysis of convergence it was determined that a three-dimensional model with nonlinear material properties would require seven days to solve. To reduce the computational time, the modeling progressed in three stages. In the first stage, a three-dimensional model was run with elastic material properties of the polyethylene and heterogeneous but elastic material properties of the talus. The forces were applied to the top of the tibia and fibula as described in Section 4.5. The talar volume was meshed with an element size of four millimeters. A course mesh was created on the articulating surfaces between the polyethylene and talar component to speed up the convergence (element size 2 of Table 7). This model still contained 72,492 nodes and 48,104 elements ("Modified" model, Figure 7.1) and took 44 hours to solve.

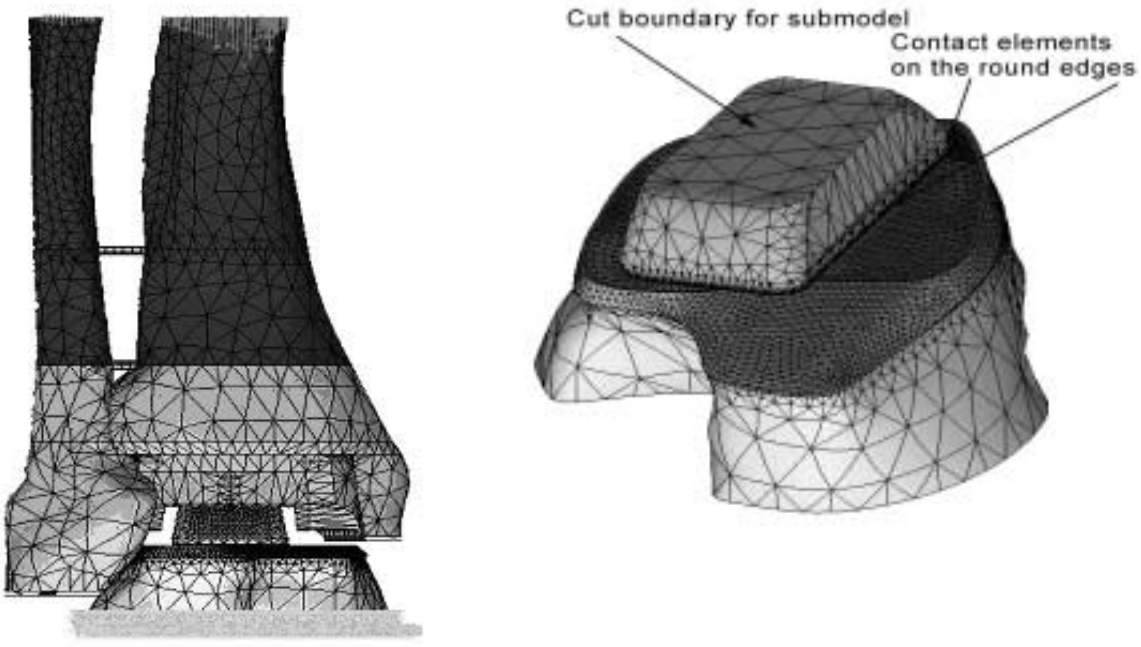

Figure 7.1 3-D FEM model (left) and submodel (right) for analysis of stresses in the talus

In the second stage, a submodel was created with refined elements with a length of one milimeter for the cancellous bone around the talar component. Cut boundary conditions were selected just below the interface of the polyethylene insert and the talar component to eliminate this contact pair. Another contact pair was defined along the round edges of the base (Figure 7.1). These round edges could potentially contact the talus. This contact pair did not require as many iterations to converge because the rest of the talar component was attached to the volume of the talus. The material properties of cancellous bone of the talus were changed to elasto-plastic and heterogeneous. This submodel (for the "Modified" implant) contained 79,163 nodes and 57,182 elements from which 44,870 nodes were in cancellous bone extending three millimeters beneath

the implant. The submodel was loaded by displacements from cut boundaries, decreasing the solution time to five hours. Since we changed material properties from elastic to elasto-plastic between the full model and submodel, the resulting reaction forces in the submodel were smaller than the total force applied to the full model. This was due to the fact that the full model with elastic properties was stiffer with smaller displacements than the submodel with elasto-plastic material properties.

The third stage of calculations corrected this by scaling the applied displacements in the cut boundary areas and rerunning the submodel. The reaction forces were checked again and agreed well with the originally applied force. Another convergence study of mesh refinement was not carried out. However, the size element of one millimeter of the cancellous and cortical bone in the vicinity of the talar component was identical to a converged element size in the study by Perrillo-Marcone.[165]

7.1 Results

It has been demonstrated by several studies that while the yield stress may vary considerably across the location of cancellous bone, the yield and ultimate strains may be considered constant. The cancellous bone in our simulation was modeled as elasto-perfectly plastic material with heterogeneous Young's modulii. Yielding was taken to occur at a strain of 0.8% and no load carrying capacity was predicted at strains of and greater than 1.5%. The thin layer of cortical bone was modeled as a homogeneous elasto-perfectly plastic material with a yield strength of 100 MPa. For the Young's modulus of 9,650 MPa, the calculated yield strain is 1.09%. The cortical bone was predicted to have no load carrying capacity at strains greater than 3%. The von Mises strain was used to

predict failure. Elastic strains were calculated with a Poisson's ratio of 0.3 and plastic strains were calculated with a Poisson's ratio of 0.5.

The strains in the cancellous bone of the talus for both talar component designs are given in Figure 7.2. The dark blue color represents contours of strains from 0.7-0.9%, predicting yield. The orange color represents contours of strain from 1.4-1.6% for the prediction of failure zones. The cancellous bone is predicted to yield only around the edges of the implants. Both implants are predicted to cause a localized failure of the bone on the medial-posterior corner. The strains in this corner reached 1.7% in the "Modified" implant and 2.6% in the "Standard" implant. Both of the talar components had higher strains on the medial side than the lateral side.

For a more detailed inspection of the average strains under the implants, strains were computed along four different paths on the surface of the cancellous bone. The paths run medially, laterally, posteriorly and anteriorly under the implants (Figure 7.2). For each path, an average strain was calculated (Table 8) from the flat portions of the curves on Figure 7.3 and on Figure 7.4). The largest reduction in strain between the implant designs occurred at the posterior edge where the average strain fell from 0.42% to 0.26%. All the average strains are below the yield strain of 0.8%. On average, the "Modified" talar component decreased strains in cancellous bone by 24%.

Table 8 The average von Mises strain in cancellous bone along different paths

Paths	*Modified (%)*	*Standard (%)*
Medial	0.33	0.41
Lateral	0.25	0.30
Posterior	0.34	0.42
Anterior	0.26	0.42
Average	0.30	0.39

The cortical bone experienced peak strains of up to 1.2% posteriorly for the "Standard" model. The "Modified" model was predicted to create maximum strains of 1.4% anteriorly.

The biggest change of strain during gait was expected in the anterior and posterior regions of the talus. Posteriorly, the average strain (Figure 7.5 top) increased from 0.42% in 10 degrees of dorsiflexion to around 0.6% in 20 degrees of plantarflexion. The strains in 10 degrees of dorsiflexion remained relatively unchanged compared to the neutral position. The strains on the anterior side of the talus had the opposite tendency but only on the lateral side, away from cortical bone.

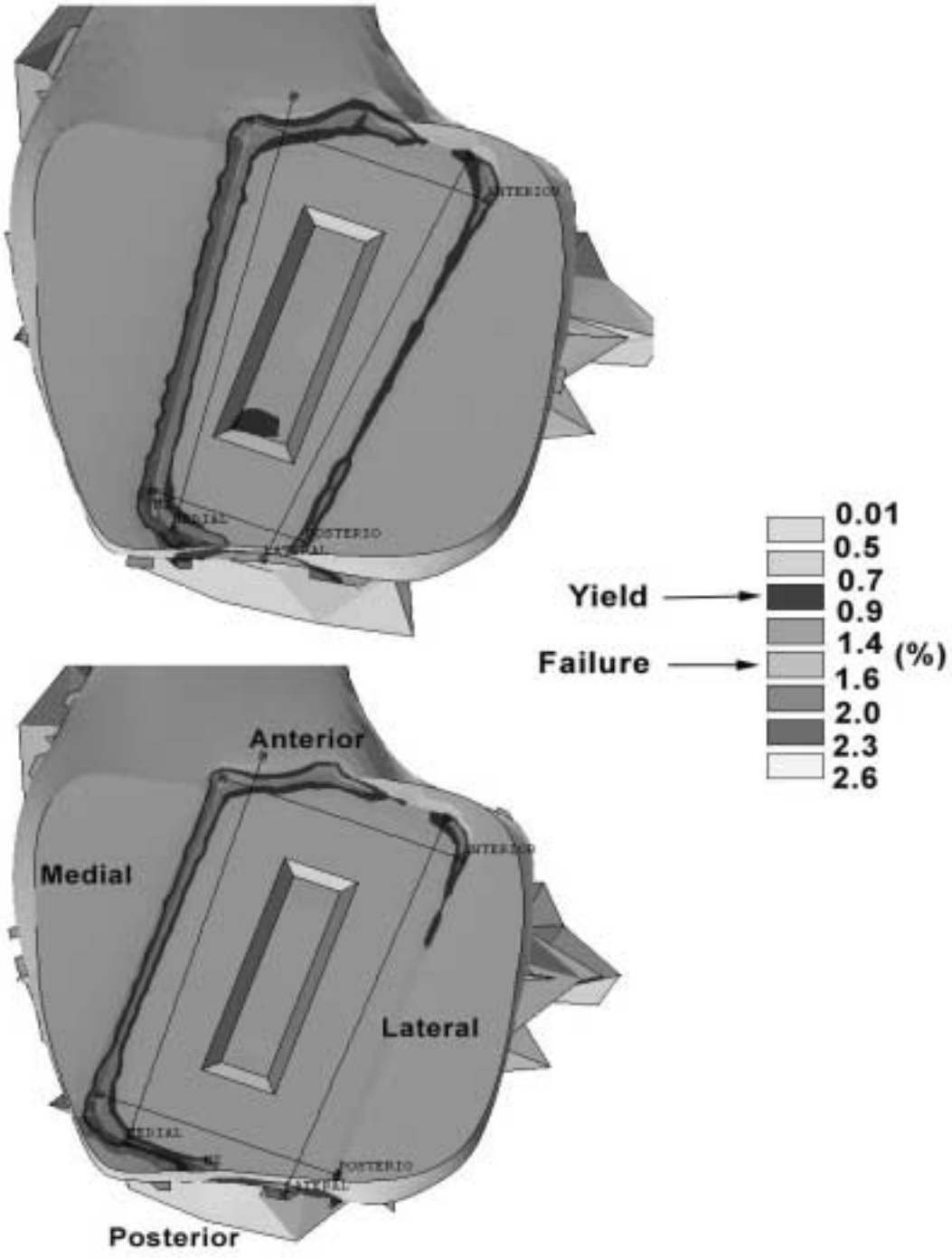

Figure 7.2 von Mises strain distribution in cancellous bone loaded by the "Standard" (top) and the "Modified" (bottom) talar components

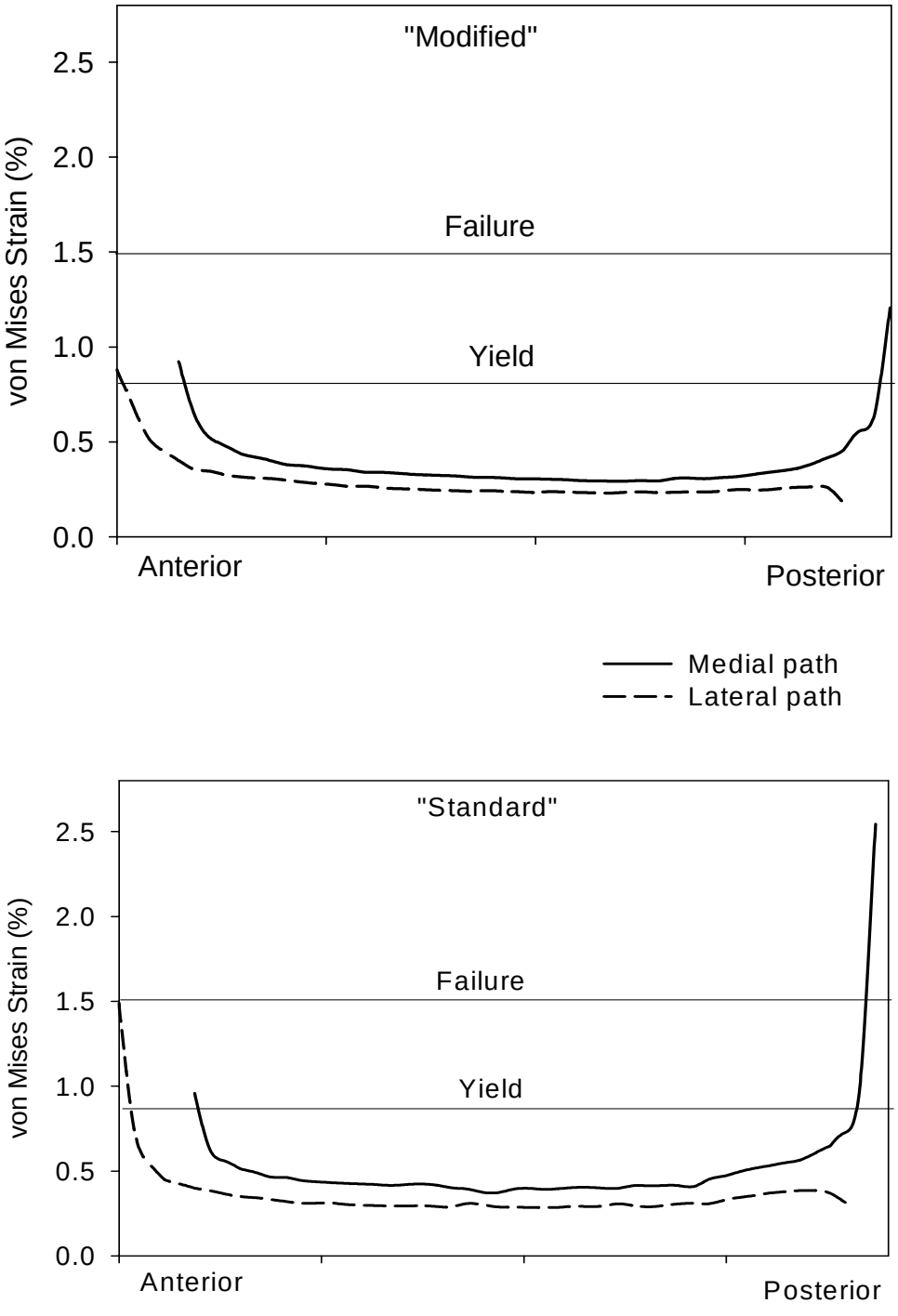

Figure 7.3 von Mises strain in cancellous bone along medial and lateral paths

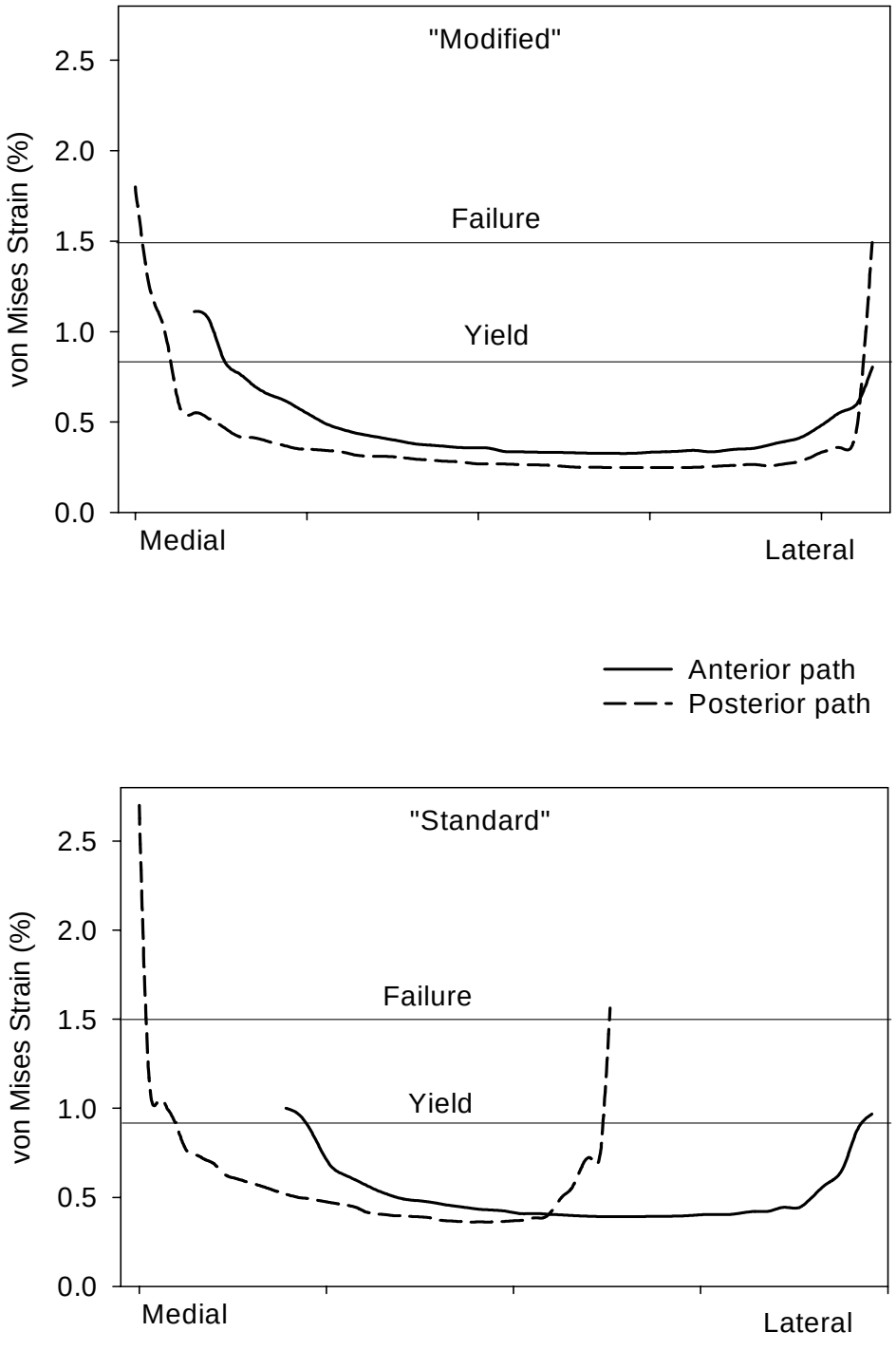

Figure 7.4 von Mises strain in cancellous bone along anterior and posterior paths

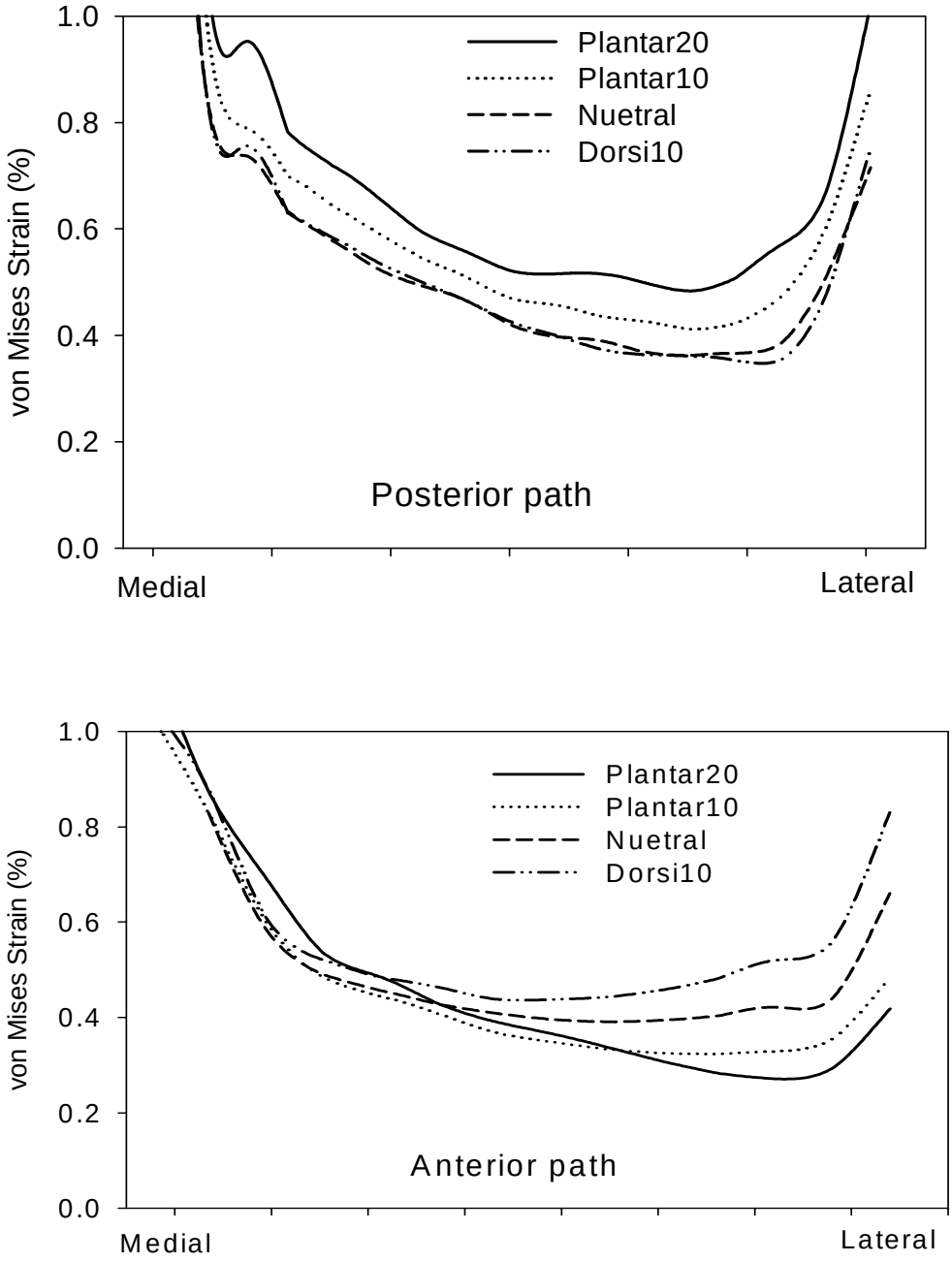

Figure 7.5 Effect of gait on von Mises strain in cancellous bone of the talus loaded by the "Standard" talar component. Results presented along the anterior and posterior paths without strain concentrations at the edges.

7.2 Discussion of Talar Stresses

The main aim of this study was to investigate the magnitude and distribution of strains in the talus loaded by two talar component designs. Cancellous bone was modeled as heterogeneous elasto-plastic material. Anisotropy was not included, but was shown to have a negligible influence on the results if heterogeneity was included.[166] A strain-based failure criteria was chosen because it was observed that failure strains were independent of density and direction.[87, 90] The yield strength calculated from a constant yield strain of 0.8% varied from 4-6.8 MPa. This corresponded well to the ultimate compressive strength of 6 MPa of the stronger medial cancellous bone of the proximal tibial compartment as found by Taylor et al.[167] in a study of effect of bone stresses on knee implant migration. Another study by Taylor et al.[106] found a relationship between stresses in cancellous bone and two year clinically measured subsidence of certain types of hip implants.

Seven of eighty-five clinically observed "Standard" talar components were reported to have tilted.[51] The exact nature of tilt is unclear from the paper. Based on our results it could be estimated that the talar component tilted in the sagittal plane posteriorly. This could have occured if either the talar component did not touch the cortical rim or the cortical bone was damaged during surgery. In this situation, the anterior cortical bone and the stronger anterior-lateral cancellous bone could have served as an axis around which the talar component could subside into the weaker posterior cancellous bone. Given that our study found some localized yielding, initial subsidence could have occurred followed by bone remodeling. Subsequent subsidence would depend

on the strength of the remodeled bone. Our FEM model predicted a 0.1 mm displacement on the medial side of the talar component. Thus it is likely that subsidence is related more to a progressive failure of the bone over a period of time. It was hypothesized[107] that cancellous bone will fail in creep at a low cycle, high initial strain load and by accumulated microdamage at a high cycle, low initial strain. Taylor et al.[168] felt that the subsidence of implants was more likely due to fatigue bacause it was unlikely that older patients would load the bone for an extended period of time. Kempson et al.[32] estimated the fatigue strength of cancellous bone to be one third of the ultimate compressive strength. Michel et al.[107] reported the fatigue strength of cancellous bone to be 40% of the ultimate compressive strength of bovine bone for one million cycles. Based on the above results we decided to take one third of the ultimate compressive strength as an approximation of fatigue failure strength of cancellous bone. The strain at the fatigue limit was then calculated as 0.5%. Our results indicated that the trabeculae in the vicinity of the edges experienced plastic deformation due to stress concentrations. The shear strains at the edges reached 3.5%, very close to the reported value of ultimate shear strain of bovine bone (Table 1). These areas may serve as initiators for subsidence. As discussed in Section 6.3 rounding the edges would not eliminate theses stress concentrations. The average strain away from the edges was 0.39% for the "Standard" model and 0.3% for the "Modified" model, both below the estimated fatigue value of 0.5%. However, the average strains varied with dorsi-plantarflexion and reached 0.5% both posteriorly at 20 degrees of plantarflexion and anteriorly at 10 degrees of dorsiflexion in the "Standard" model (Figure 7.5).

The positioning of the talar component with respect to the cortical rim seemed to have an importance for strains in the cancellous bone. This was demonstrated on the "Standard" talar component design. In dorsiflexion, more load was transferred to the anterior portion of the implant. The implant was resting on the cortical bone only on the medial side creating a pivot point around which the implant was pushed into cancellous bone on the lateral side (Figure 7.5, bottom). Thus we recommend, especially for the wider "Modified" talar component, that ideally all four corners rest on the cortical rim. This could prevent the implant from causing yield of the cancellous bone under the implant. The shape of the talar component is rectangular and the shape of the resected talar surface is round but irregular. For the talar component to rest on all four corners, it would be necessary that some parts of the implant would overhang the cortical rim. This could potentially influence the soft tissues surrounding the ankle joint.

The cortical bone was modeled as a homogeneous elasto-plastic material. The maximum strains found in the cortical bone were up to 1.4% which is above the yield limit of 1.09%. Thus, localized yield can be expected under parts of the talar components. It is not expected that the cortical bone would loose load carrying capacity as the ultimate compressive strain of 3% was not reached.

8.0 CONCLUSIONS

A three-dimensional (3-D) FEM model of the tibia, fibula, talus and Agility® ankle implant were developed. The model was used for the analysis of stresses and strains in the UHMWPE insert and in the talus for two designs of the talar component. For the study of stresses in the UHMWPE insert, we also derived an analytical solution for the contact of two counterformal cylinders and included a two-dimensional (2-D) FEM model.

The results indicated that the wider "Modified" talar shape decreased UHMWPE von Mises stress in the middle of the sagittal plane below the value of the yield strength of 10.86 MPa. The peak von Mises stress at the lateral edge reached 13.6 MPa and was the same as that of the "Standard" shape. The stress concentrations at the lateral and medial edges may cause local plastic deformation.

The analytical solution provided good results compared to a geometrically identical FEM model but failed to predict results comparable to that of the 3-D FEM model. The 2-D FEM model was a good approximation of the 3-D FEM model when plane strain conditions were satisfied.

It is generally believed and intuitive that increased pressure will increase the von Mises stress. We showed on two examples that this is not always true. Firstly, increasing Poisson's ratio increased contact pressure while the von Mises stress decreased. Secondly, an example more important for study of ankle joint implants showed that contact pressure decreased with increasing thickness as expected. However, the von Mises stress increased. It was during this study that we discovered that the 2-D FEM

model was a good approximation of the 3-D FEM model only when plane strain conditions were satisfied. In the “Standard” model, the plane strain condition was not satisfied and the 3-D FEM model predicted a decrease of both the contact pressure and von Mises stress with increasing thickness of the UHMWPE.

The analysis of strains in the cancellous bone of the talus showed that both of the talar components created concentrations of strain near the edges of the base. These strain concentrations caused localized yield and could be related to clinically observed talar component tilt. The average strain away from the edges was below the estimated fatigue strain limit for both of the designs. Due to the increased area of the base, the “Modified” design decreased average strains by 24% compared to the “Standard” design. Seating the talar component on the rim of the cortical bone could help prevent penetration of the corners of the implant into the cancellous bone during walking.

Future work could improve the 3-D FEM model model by including all or most of the bones, ligaments and muscles of the foot. Ground reaction pressure distribution could then be applied to the sole of the foot. The tibia could be constrained but the fibula should be allowed to move 1-2 millimeters relative to the tibia and attached to the tibia with nonlinear springs. The muscles and ligaments could be modeled with solid or shell elements although a computationally more effective way would be use of beam elements. The attachment of muscles and ligaments modeled with beam elements would not have to be restricted to a single node. Constraint equations could be used to model a line where the muscles and ligaments attach. Some of the ligaments glide on the top of the bones which should be captured by contact elements. Some of the joints in the foot do not

experience large relative motion and could be modeled with elements with a very small (almost zero) Young's modulus instead of creating separate surfaces requiring contact elements.

Future work on the implant model could investigate the effect of modeling the interface between the polyethylene insert and the tibial tray with contact elements. In our study this interface was modeled as perfectly bonded. In reality, the tibial tray has slots on the medial and lateral sides (not modeled here) for insertion of the polyethylene and the tray and insert are otherwise not bonded.

APPENDIX

APPENDIX

BASIC ANATOMIC TERMS OF THE FOOT

There still exists a considerable ambiguity in the use of terms concerning the joints of the human foot despite the efforts toward standardizing both of anatomists and clinicians. A nice explanation of basic anatomic terms from clinical point of view can be found on http://www.footmaxx.com/clinicians/glossary.html The following basic terms are citations with some editing for better clarity of the terms.

1 Proximal and Distal

Proximal means closer to the heart.

Distal means further away from the heart.

2. Three anatomical planes

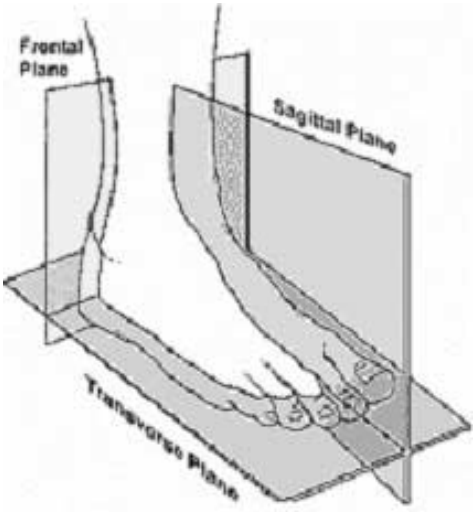

Transverse: divides top and bottom.

Frontal (coronal): divides front and back.

Sagittal: divides left and right.

Figure A- 1 Anatomical planes of the foot

3. Three single plane motions of the foot

3a, Motions occurring in the transverse plane.

Abduction of the foot is it's lateral rotation (i.e. away from the mid-line body axis).

Adduction of the foot is it's medial rotation (i.e. towards the mid-line body axis).

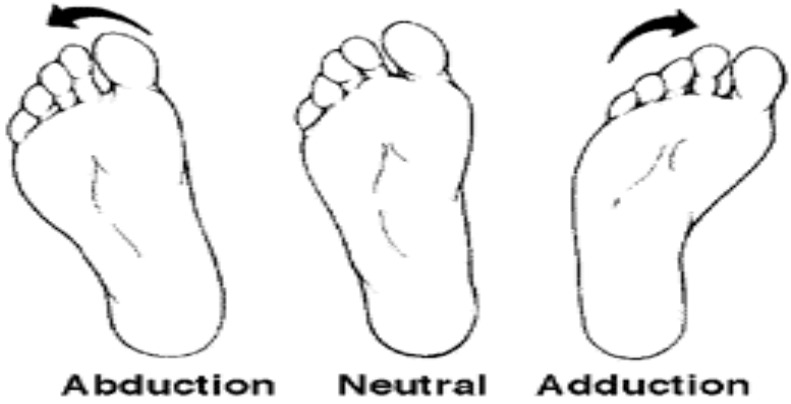

Figure A- 2 Abduction and Adduction.

3b, Motions occurring in the frontal plane.

Inversion is rotation of the foot in to the mid-line of the body and upward.

Eversion is rotation of the foot away from to the mid-line of the body and upward.

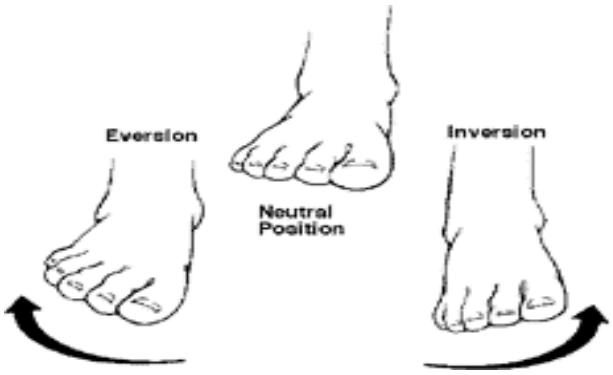

Figure A- 3 Inversion and Eversion

3c, Motions occurring in the sagittal plane.

Plantarflexion is downwards motion of the foot away from the body.

Dorsiflexion . is upwards motion of the foot towards the body.

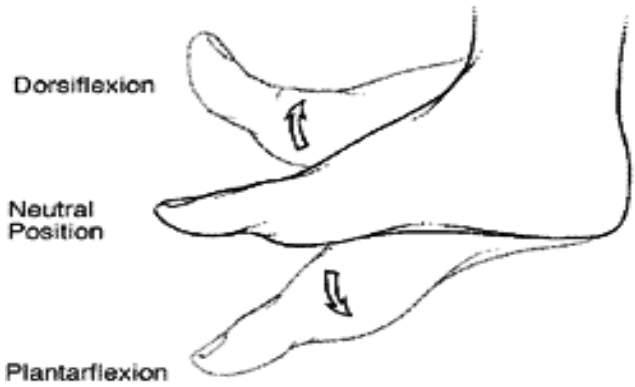

Figure A- 4 Dorsiflexion and plantarflexion

4. Simultaneous motions in the frontal, sagittal and transverse planes

Pronation is a triplane motion consisting of simultaneous motions of eversion, abduction, dorsiflexion.

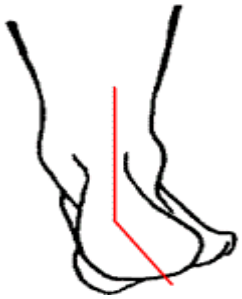

Figure A- 5 Pronated foot

Supination is a triplane motion which combines the motions of inversion, adduction, plantarflexion.

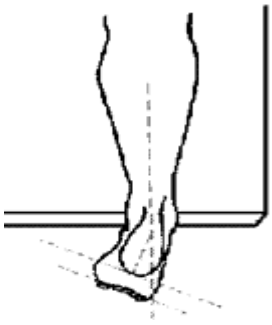

Figure A- 6 Supinated foot

5. Lateral and Medial

Lateral means on the side away from the mid-line sagittal plane.

Medial means on the side closer to the mid-line sagittal plane.

6. Dorsum and Plantar surfaces

The **dorsum** surface of the foot is the top part of the foot.

The **plantar** surface of the foot is the sole of the foot.

BIBLIOGRAPHY

BIBLIOGRAPHY

1. Conti, S.F. and Y.S. Wong, *Complications of Total Ankle Replacement.* Clinical Orthopeadics and Related Research, 2001(391): p. 105-114.

2. Tooms, R.E., *Arthroplasty of Ankle and Knee*, in *Campbell's Operative Orthopedics*, A.H. Crenshaw, Editor. 1987, C. V. Mosby Company: St. Lois. p. 1145-1150.

3. Crowell, H.P., *III: Three Dimensional Finite Element Analysis of an Ankle Prosthesis.* Innovative Technological Biological Medicine, 1991. **12**: p. 2-12.

4. Calderale, P.M., et al., *Biomechanical Design of the Total Ankle Prosthesis.* Engineering in Medicine, 1983. **12**(2): p. 69-80.

5. Falsig, J., I. Hvid, and N.C. Jensen, *Finite Element Stress Analysis of Some Ankle Prosthesis.* Clinical Biomechanics, 1986. **1**: p. 71-76.

6. Lewis, G. and G.E. Austin, *A Finite Element Analysis Study of Static Stresses in a Biomaterial Implant.* Innovations and Technology in Biology and Medicine, 1994. **15**(5): p. 634-644.

7. Oonishi, H., *Cementless Alumina Ceramic Artificial Ankle Joint*, in *Biomaterials and Biomechanics*, P. Ducheyne, Editor. 1984, Elsevier Science Publishers B. V.: Amsterdam. p. 85-90.

8. Genda, E., et al. *Three Dimensional Stress Analysis of Ankle and Foot Joints*. in *45th Annual Meeting, Orthopaedic Research Society*. February, 1999. Aneheim, California. p. 390.

9. DiGioia, A.M. *A Structural Model of the Ankle: an Examination of Normal Joint Mechanics.* in *38th Annual Meeting, Othopedic Research Society*. February 17-20, 1992. Washington, D.C. p. 263.

10. Giddings, V.L., et al., *Calcaneal Loading During Walking and Running.* Medicine & Science in Sports & Exercise, 2000. **32**(2): p. 627-634.

11. Bandak, F.A., R.E. Tannous, and T. Toridis, *On the Development of an Osseo-Ligamentous Finite Element Model of the Human Ankle Joint.* International Journal of Solids and Structures, 2001. **38**: p. 1681-1697.

12. Digges, K.H., et al., *Determination and Modeling of Ankle Injury Causation*, http:/www.ncac.gwu.edu/archives/papers/ankle/ankle.html.

13. Ledoux, W.R., et al., *Finite Element Foot Modeling*, http://www.truegrid.com/gallery/show_foot.html.

14. Tannous, R.E., et al. *A Three-Dimensional Finite Element Model of Human Ankle: Development and Preliminary Application to Axial Impulsive Loading*. in *Proceedings of the 40th Stapp Car Crash Conference*. Nov. 1996. Albuquerque, N.M.: Warrendale, PA: Society of Automotive Engineers. p. 219-238.

15. McIff, T.I., *Contact and Internal Stress Distribution in Two Types of Contemporary 'Unconstrained' Total Ankle Designs.* Journal of Biomechanics, 2001. **34**: p. S23-S28.

16. Williams, P.I. and R. Warwick, *Grays Anatomy*. 36th ed. 1980, N.Y.: W. B. Saunders Company. p. 397-410.

17. Rosse, C. and P. Gaddum-Rosse, *Textbook of Anatomy*. 5th ed. 1997, Philadelphia: Lippincott-Raven. p. 342.

18. Jacques, G., *Atlas of Human Limb Joints*. 1981, N.Y.: Spring-Verlag Berlin Heidelberg. p. 93.

19. Stiehl, J.B., ed. *Inman's Joints of the Ankle*. 2nd ed. 1991, Williams & Wilkins: Baltimoro. 1-84.

20. Ellis, H., *Clinical Anatomy*. 5th ed. 1972, Oxford: Blackwell Scientific Publications. p. 224.

21. Stauffer, R.N., E.Y.S. Chao, and R.C. Brewster, *Force and Motion Analysis of the Normal, Diseased, and Prostetic Ankle Joint.* Clinical Orthopedics, 1977. **127**: p. 189-196.

22. Pal, G.P. and R.V. Routal, *Architecture of the Cancellous Bone of the Human Talus.* The Anatomical Record, 1998(252): p. 185-193.

23. Lewis, G., *The Ankle Joint Prosthetic Replacement: Clinical Performance and Research Challenges.* Foot & Ankle International, 1994. **15**(9): p. 471-476.

24. Mann, R.A., *Biomechanics of the Foot*, in *Atlas of Orthotics/ American Academy of Orthopaedic Surgeons*. 1985, C. V. Mosby Company: St. Louis, Missouri. p. 112-125.

25. Buechel, F.F., M.J. Pappas, and L.J. Iorio, *New Jersey Low Contact Stress Total Ankle Replacement: Biomechanical Rationale and Review of 23 Cementless Cases.* Foot & Ankle, 1988. **8**(6): p. 279-290.

26. Giannini, S., A. Leardini, and J.J. O'Connor, *Total Ankle Replacement: Review of the Designs and of Current Status.* Foot & Ankle Surgery, 2000. **6**: p. 77-88.

27. Lachiewicz, P.F., et al., *Total Ankle Replacement in Rheumatoid Arthritis.* Journal of Bone and Joint Surgery, 1984. **66-A**(3): p. 340-343.

28. Saltzman, C.L., et al., *Total Ankle Replacement Revisited.* Journal of Orthopedic & Sports Physical Therapy, 2000. **30**(2): p. 56-57.

29. William, P., *Total Ankle Arthroplasty*, in *Total Joint Replacement*. 1991, W.B. Saunders company. p. 749-759.

30. Inman, V.T., *The Joints of the Ankle*. 1976, Baltimore: Williams & Wilkins.

31. Alvine, F.G., *Agility Total Ankle System, Surgical Technique*. 1999, DePuy a Johnson & Johnson company: Warsaw, Indiana. p. 10.

32. Kempson, G.E., M.A.R. Freeman, and M.A. Tuke, *Engineering Consideretions in the Design of an Ankle Joint.* Biomedical Engineering, 1975. **10**: p. 166-180.

33. Pappas, M., F.F. Buechel, and A.F. DePalma, *Cylindrical Total Ankle Joint Replacement: Surgical and Biomechanical Rationale.* Clinical Orthopedics and Related Research, 1976(118): p. 82-92.

34. Morrissy, R.T., ed. *Dynamics of the Foot and Gait*. 3rd ed. Lovell and Winter's Pediatric Orthopedics. Vol. 1. 1990, Lippincott: Philadelphia.

35. Barnett, C. and J. Napier, *The Axis of Rotation at the Ankle Joint in Man, its Influence Upon the Form of the Talus and Mobility of the Fibula.* Journal of Anatomy, 1952(86): p. 1-9.

36. Hicks, J.H., *The Mechanics of Foot. I: The Joints.* Journal of Anatomy, 1953(87): p. 345.

37. Sarrafian, S.K., *Anatomy of theFoot and Ankle: descriptive, Topographic, Functional*. 2nd ed. 1993, Philadelphia: J. B. Lippincott Company. p. 474-509.

38. Bottlang, M., J.L. Marsh, and T.D. Brown, *Articulated External Fixation of the Ankle: Minimizing Motion Resistance by Accurate Axis Alignment.* Journal of Biomechanics, 1999. **32**: p. 63-70.

39. Leardini, A., et al., *A Geometric Model of the Human Ankle Joint.* Journal of Biomechanics, 1999. **32**: p. 585-591.

40. Lundberg, A., et al., *The Axis of Rotation of the Ankle Joint.* The Journal of Bone and Joint Surgery, 1989. **71-B**(1): p. 94-99.

41. Lundberg, A., et al., *Kinematics of the Ankle/Foot Complex-Part1: Plantarflexion and Dorsiflexion.* Foot & Ankle, 1989. **9**(4): p. 194-200.

42. Lundberg, A., et al., *Kinematics of the Ankle/Foot Complex-Part2: Pronation and Supination.* Foot & Ankle, 1989. **9**(5): p. 248-253.

43. Lundberg, A., et al., *Kinematics of the Ankle/Foot Complex-Part3: Influence of Leg Rotation.* Foot & Ankle, 1989. **9**(5): p. 304-309.

44. Siegler, S., J. Chen, and C.D. Schneck, *The Three-Dimensional Kinematics and Flexibility Characteristics of the Human Ankle and Subtalar Joints. Part 1: Kinematics.* Journal of Biomechanical Engineering, 1988(110): p. 364-373.

45. Leardini, A., et al., *The Role of the Passive Structures in the Mobility and Stability of the Human Ankle Joint: A Literature Review.* Foot & Ankle International, 2000. **21**(7): p. 602-614.

46. Leardini, A., et al., *Computer Assisted Design of the Sagittal Shapes of a Ligament-Compatible Toatl Ankle Replacement.* Medical & Biological Engineering & Computing, 2001. **39**: p. 168-175.

47. Demetriades, L., E. Strauss, and J. Gallina, *Osteoarthitis of the Ankle.* Clinical Orthopedics and Related Research, 1998(349): p. 28-42.

48. Coventry, M.B., *The History of Joint Replacement Arthroplasty*, in *Reconstructive Surgery of the Joints*, B.F. Morrey, Editor. 1996, Churchill Livingstone: New York. p. 3-5.

49. Canale, S.T., ed. *Campbell's Opperative Orthopedics*. 9th ed. 1998, Mosby-Year Book Inc.: St. Louis, Missouri. 233-234.

50. Jensen, N.C. and K. Kroner, *Total Ankle Joint Replacement: A Clinical Follow up.* Orthopedics, 1992. **15**: p. 236-239.

51. Pyevich, M.T., et al., *Total Ankle Arthroplasty:Unique Design, Two to Eleven Year Follow-up.* The Journal of Bone and Joint Surgery, 1998. **80-A**(10): p. 1410-1420.

52. Petty, W., *Total Joint Replacement*. 1991, Philadelphia: W. B. Saunders. p. 7-10.

53. Michelson, J.D., G.R. Schmidt, and M.S. Mizel, *Kinematics of a Total Arthroplasty of the Ankle: Comparison to Normal Ankle Motion.* Foot & Ankle International, 2000. **21**(4): p. 278-284.

54. Bauer, G. and e. al., *Total Ankle Replacement. Review and Critical Analysis of the Current Status.* Foot and Ankle Surgery (European), 1996. **2**: p. 119-126.

55. Kitaoka, H.B., et al., *Survivorship Analysis of the Mayo Total Ankle Arthroplasty.* The Journal of Bone and Joint Surgery, 1994. **76-A**(7): p. 974-979.

56. Waugh, T.R., P. Evanski, and W.C. McMaster, *Irvin Ankle Arthroplasty, Prostehetic Design and Surgical Technique.* Clinical Orthopedics and Related Research, 1976(114): p. 181-184.

57. Cowin, S.C., *Bone Mechanics*. 1st ed. 1989, Boca Raton, Florida: CRC Press, Inc. p. 97-155.

58. Rho, J.-Y., L. Kuhn-Spearing, and P. Zioupos, *Mechanical Properties and the Hierarchical Structure of Bone.* Medical Engineering & Physics, 1998. **20**: p. 92-102.

59. Wolff, J., *Das Gesetz der Transformation der Knochen*. 1892, Berlin: A. Hirchwild.

60. Carter, D.R. and W.C. Hayes, *The Compressive Behaviour of Bone as a Two-Phase Porous Structure.* Journal of Bone Joint Surgery, 1976. **59**: p. 954-962.

61. Turner, C.H., et al., *The Elastic Properties of Trabecular and Cortical Bone Tissues are Similar: Results from Two Microscopic Measurement Techniques.* Journal of Biomechanics, 1999. **32**: p. 437-441.

62. Keaveny, T.M., et al., *Differencies between the Tensile and Compressive Strengths of Bovine Tibial Trabecular Bone Depend on Modulus.* Journal of Biomechanics, 1994. **27**(9): p. 1137-1146.

63. Keaveny, T.M., et al., *Trabecular Bone Yields Like a Damaging Material.* Advances in Bioengineering, 1993. **26**: p. 187-189.

64. Niebur, G.L., et al., *High-Resolution Finite Element Models with Tissue Strength Asymmetry Accurately Predict Failure of Trabecular Bone.* Journal of Biomechanics, 2000. **33**: p. 1575-1583.

65. Rice, J.C., S.C. Cowin, and J.A. Bowman, *On the Dependence of the Elasticity and Strength of Cancellous Bone on Apparent Density.* Journal of Biomechanics, 1988. **21**: p. 122-168.

66. Zysset, P.K., et al., *Elastic Modulus and Hardness of Cortical Bone and Trabecular Bone Lamellae Measured by Nanoindentation in the Human Femur.* Journal of Biomechanics, 1999. **32**: p. 1005-1012.

67. Rho, J.Y., R.B. Ashman, and C.H. Turner, *Young's Modulus of Trabecular and Cortical Bone Material: Ultrasonic and Microtensile Measurements.* Journal of Biomechanics, 1993. **26**(2): p. 111-119.

68. Pidaparti, R.M.V. and C.H. Turner, *Cancellous Bone Architecture: Advantages of Nonorthogonal Trabecular Aligment Under Multidirectional Joint Loading.* Journal of Biomechanics, 1997. **30**(9): p. 979-983.

69. Muller, R. and P. Ruegsegger, *Analysis of Mechanical Properties of Cancellous Bone Under Conditions of Simulated Bone Atrophy.* Journal of Biomechanics, 1996. **29**(8): p. 1053-1060.

70. Rietbergen, B.V., et al., *A New Method to Determine Trabecular Bone Elastic Properties and Loading Using Micromechanical Finite-Element Models.* Journal of Biomechanics, 1995. **28**(1): p. 69-81.

71. Fung, Y.C., *Biomechanics, Mechanical Properties of Living Tissues*. 2nd ed. 1993, New York: Springer-Verlag. p. 500.

72. Uchiyama, E., Yamakoshi, K. and Sasaki, T., *Measurement of Mechanical Characteristics of Tibial Periosteum and Evaluation of Local Differencies.* Journal of Biomechanical Engineering, 1998. **120**: p. 85-91.

73. Ricos, V., et al., *Effects of Anisotropy and Material Axis Registration on Computed Stress and Strain Distributions in the Turkey Ulna.* Journal of Biomechanics, 1996. **29**(2): p. 261-267.

74. Buckwalter, J.A., et al., *Bone Biology.* The Journal of Bone and Joint Surgery, 1995. **77-A**(8): p. 1256-1289.

75. Sabry, F.F., et al., *Internal Architecture of the Calcaneus: Implications for Calcaneus Fractures.* Foot & Ankle International, 2000. **21**(2): p. 114-118.

76. Mammone, J.F. and S.M. Hudson, *Micromechanics of Bone Strength and Fracture.* Journal of Biomechanics, 1993. **26**(4/5): p. 439-446.

77. Ford, C.M., T.M. Keaveny, and W.C. Hayes, *The Effect of Impact Direction on the Structural Capacity of the Proximal Femur During Falls.* Journal of Bone and Mineral Research, 1996. **11**(3): p. 377-383.

78. Keaveny, T.M., et al., *Application of the Tsai-Wu Quadratic Multiaxial Failure Criterion to Bovine Trabecular Bone.* Journal of Biomechanical Engineering, 1999. **121**: p. 99-107.

79. Ford, C.M. and T.M. Keaveny, *The Dependence of Shear Failure Properties of Trabecular Bone on Apparent Density and Trabecular Orientation.* Journal of Biomechanics, 1996. **29**(10): p. 1309-1317.

80. Goldstein, G.A., *The Mechanical Properties of Trabecular Bone: Dependence on Anatomic Location and Function.* Journal of Biomechanics, 1987. **20**(11): p. 1055-1061.

81. Linde, F., I. Hvid, and F. Madsen, *The Effect of Specimen Geometry on the Mechanical Behaviour of Trabecular Bone Specimens.* Journal of Biomechanics, 1992. **25**(4): p. 359-368.

82. Rohl, L., et al., *Tensile and Compressive Properties of Cancellous Bone.* Journal of Biomechanics, 1991. **24**: p. 1143-1149.

83. Neil, J.L., et al. *Tensile and Compressive Properties of Vertebral Trabecular Bone*. in *Transactions of 29th Orthopeadic Reasearch Society*. 1983. p. 334.

84. Carter, D.R., G.H. Schwab, and D.M. Spengler, *Tensile Fracture of Cancellous Bone.* Acta Orthopedica Scandinavia, 1980. **51**: p. 733-741.

85. Kaplan, S.J., et al., *Tensile Strength of Bovine Trabecular Bone.* Journal of Biomechanics, 1985. **18**: p. 723-727.

86. Keaveny, T.M., et al., *Trabecular Bone Exhibits Fully Linear Elastic Behaviour and Yields at Low Strains.* Journal of Biomechanics, 1994. **27**(9): p. 1127-1136.

87. Keaveny, T.M., et al. *Yield Strains for Bovine Trabecular Bone are Isotropic but Asymmetric*. in *Transactions of 40th Orthopaedic Research Society*. 1994. p. 428.

88. Keaveny, T.M., et al., *Author's Response.* Journal of Biomechanics, 1995. **28**(6): p. 765.

89. Turner, C.H., *Yield Behaviour of Bovine Cancellous Bone.* Journal of Biomecanical Engineering, Transactions of the ASME, 1989. **111**: p. 256-260.

90. Turner, C.H., *Is Yield Strain in Cancellous Bone Isotropic?* Journal of Biomechanics, 1995. **28**(6): p. 763.

91. Kopperdahl, D.L. and T.M. Keaveny, *Yield Strain Behaviour of Trabecular Bone.* Journal of Biomechanics, 1998. **31**: p. 601-608.

92. Morgan, E.F. and T.M. Keaveny, *Dependence of Yield Strain of Human Trabecular Bone on Anatomic Site.* Journal of Biomechanics, 2001. **34**: p. 569-577.

93. Fenech, C.M. and T.M. Keaveny, *A Celular Solid Criterion for Predicting the Axial-Shear Failure Properties of Bovine Trabecular Bone.* Journal of Biomechanical Engineering, 1999. **121**: p. 414-422.

94. Lotz, J.C., E.J. Cheal, and W.C. Hayes, *Fracture Prediction of the Proximal Femur Using Finite Element Models: Part II-Nonlinear Analysis.* Journal of Biomechanical Engineering, Transactions of the ASME, 1991. **113**: p. 361-365.

95. Silva, M.J., T.M. Keaveny, and W.C. Hayes, *Computed Tomography-Based Finite Element Analysis Predicts Failure Loads and Fracture Patterns for Verterbal Sections.* Journal of Orthopeadic Research, 1998. **16**: p. 300-308.

96. Keyak, J.H. and S.A. Rossi, *Prediction of Femoral Fracture Load Using Finite Element models: An Examination of Stress- and Strain Based Failure Theories.* Journal of Biomechanics, 2000. **33**: p. 209-214.

97. Fyhrie, D.P. and D. Vashishth, *Bone Stiffness Predicts Strength Similarly for Human Verterbal Cancellous Bone in Compression and for Cortical Bone in Tension.* Bone, 2000. **26**(2): p. 169-173.

98. Lotz, J.C., E.J. Cheal, and W.C. Hayes, *Fracture Prediction of the Proximal Femur Using Finite Element Models: Part I-Linear Analysis.* Journal of Biomechanical Engineering, Transactions of the ASME, 1991. **113**: p. 353-361.

99. Keaveny, T.M. and W.C. Hayes, *A 20- Year Perspective on the Mechanical Properties of Trabacular Bone.* Journal of Biomechanical Engineering, 1993. **115**: p. 534-542.

100. Jensen, N.C., I. Hvid, and K. Kroner, *Strength Pattern of Cancellous Bone at the Ankle Joint.* Engineering in Medicine, 1988. **17**(2): p. 71-76.

101. Hvid, I., et al., *Trabecular Bone Strength Profiles at the Ankle Joint.* Clinical Orthopedics, 1985(199): p. 306-312.

102. Choi, K. and S.A. Goldstein, *A Comparison of the Fatigue Behaviour of Human Trabecular and Cortical Bone Tissue.* Journal of Biomechanics, 1992. **25**(12): p. 1371-1381.

103. Taylor, M. and K.E. Tanner, *Fatigue Failure of Cancellous Bone: A Possible Cause of Implant Migration and Loosening.* Journal of Bone and Joint Surgery, 1997. **79-B**(2): p. 181-182.

104. Martin, R.B. and D.B. Burr, *A Hypothetical Mechanism for the Stimulation of Osteonal Bone Remodeling by Fatigue Damage.* Journal of Biomechanics, 1982. **15**: p. 137-139.

105. Caler, W.E. and D.R. Carter, *Bone Creep-Fatigue Damage Accumulation.* Journal of Biomechanics, 1989. **22**: p. 625-638.

106. Taylor, M., Tanner, K.E., and Freeman, M.A.R., Yettrman A.L., *Cancellous Bone Stresses Surrounding the Femoral Component of a Hip Prosthesis: An Elastic-Plastic Finite Element Analysis.* Medical Engineering & Physics, 1995. **17**(No. 7): p. 544-550.

107. Michel, M.C., et al., *Compressive Fatique Behaviour of Bovine Trabecular Bone.* Journal of Biomechanics, 1993. **26**(4/5): p. 453-463.

108. Reilly, D.T. and A.H. Burstein, *The Elastic and Ultimate Properties of Compact Bone Tissue.* Journal of Biomechanics, 1975. **8**(393-405).

109. Lotz, J.C., T.N. Gerhart, and W.C. Hayes, *Mechanical Properties of Metaphyseal Bone in the Proximal Femur.* Journal of Biomechanics, 1991. **24**(5): p. 317-329.

110. Rohlman, A., et al., *A Nonlinear Finite Element Analysis of Interface Conditions in Porous Coated Hip Endoprostheses.* Journal of Biomechanics, 1988. **21**(7): p. 1988.

111. Brown, T.D. and A.B. Fergusson, *The Development of a Computational Stress Analysis of the Femoral Head.* Journal of Bone and Joint Surgery, 1978. **60-A**: p. 619-629.

112. Goldstein, G.A., et al., *The Mechanical Properties of Human Tibial Trabecular Bone as a Function of Metaphyseal Location.* Journal of Biomechanics, 1983. **16**(12): p. 965-969.

113. Chu, T.M., N.P. Reddy, and J. Padovan, *Three Dimensional Finite Element Stress Analysis of the Polypropylene, Ankle-Foot Orthosis: Static Analysis.* Medical Engineering and Physics, 1995. **17**(5): p. 372-379.

114. Cheal, E.J., et al., *Stress Analysis of a Condylar Tibial Component: Influence of Metaphyseal Shell Properties and Cement Injection Depth.* Journal of Orthopaedic Research, 1985. **3**: p. 424-434.

115. Seireg, A. and R.J. Arkivar, *The Prediction of Muscular Load Sharing and Joint Forces in the Lower Extremities During Walking.* Journal of Biomechanics, 1975. **8**: p. 89-102.

116. Procter, P. and J.P. Paul, *Ankle Joint Biomechanics.* Journal of Biomechanics, 1982. **15**(9): p. 627-634.

117. Komistek, R.D., et al., *Mathematical Model of the Lower Extremity joint Reaction Forces Using Kane's Method of Dynamics.* Journal of Biomechanics, 1998. **31**: p. 185-189.

118. Lambert, K.L., *The Weight-Bearing Function of the Fibula.* Journal of Bone Joint Surgery, 1971. **53-A**(3): p. 507-513.

119. Takebe, K., *Role of the Fibula in Weight-Bearing.* Clinical Orthopedics and Related Research, 1984. **189**: p. 289-292.

120. Goh, J.C.H., et al., *Biomechanical Study on the Load-Bearing Characteristics of the Fibula and the Effects of Fibular Resection.* Clinical Orthopedics and Related Research, 1992(279): p. 223-228.

121. Wang, Q., et al., *Fibula and Its Ligaments in Load Transmission and Ankle Joint Stability.* Clinical Orthopedics and Related Research, 1996(330): p. 261-270.

122. Dean, D.D., et al., *Ultra High Molecular Weight Polyethylene Particles Have Different Effects on Proliferation, Differentiation, and Local Factor Production of MG63 Osteoblast-like Cells.* Journal of Orthopaedic Research, 1999. **17**: p. 9-17.

123. Lewis, G., *Polyethylene Wear in Total Hip and Knee Arthroplasties.* Wear of UHMWPE, 1997: p. 55-75.

124. Edidin, A.A. and S.M. Kurtz, *The Evolution of Paradigms for Wear in Total Joint Arthroplasty: The Role of Design, Material, and Mechanics*. 2000.

125. Kurtz, S.M., et al., *The Yielding, Plastic Flow, and Fracture Behaviour of Ultra-High Molecular Weight Polyethylene Used in Total Joint Replacements.* Biomaterials, 1998. **19**: p. 1989-2003.

126. Estupinan, J.A., D.L. Bartel, and T.M. Wright, *Residual Stresses in Ultra-High Molecular Weight Polyethylene Loaded Cyclically by a Rigid Moving Indenter in Nonconforming Geometries.* Journal of Biomedical Material Research, 1998. **16**(1): p. 80-88.

127. Bartel, D.L., et al., *Stresses in Polyethylene Components of Contemporary Total Knee Replacements.* Clinical Orthopaedics and Related Research, 1995(317): p. 76-82.

128. Ishikawa, H., H. Fujiki, and K. Yasuda, *Contact Analysis of Ultrahigh Molecular Weight Polyethylene Articular Plate in Artificial Knee Joint During Gait Movement.* Journal of Biomechanical Engineering, 1996. **118**: p. 377-386.

129. Reeves, E.A., et al., *A Two-Dimensional Model of Cyclic Strain Accumulation in Ultrahigh Molecular Weight Polyethylene Knee Replacements.* Proceedings of the Institution of Mechanical Engineers, 1998. **212**: p. 189-198.

130. Kennedy, F.E., et al., *Contact Fatigue Failure of Ultra-High Molecular Weight Polyethylene Bearing Components of Knee Prostheses.* Journal of Tribology, 2000. **122**: p. 332-339.

131. Teoh, S.H., W.H. Chan, and R. Thampuran, *An Elasto-Plastic Finite Element Model for Polyethylene Wear in Total Hip Arthroplasty.* Journal of Biomechanics, 2002. **35**: p. 323-330.

132. Kuster, M.S., et al., *The Effects of Conformity and Load in Total Knee Replacement.* Clinical Orthopeadics and Clinical Research, 2000(375): p. 302-312.

133. Kitagawa, M., T. Onoda, and K. Mizutani, *Stress-Strain Behaviour at Finite Strains for Various Strain Paths in Polyethylene.* Journal of Materials Science, 1992. **27**: p. 13-23.

134. Bergstrom, J.S., et al., *Constitutive Modeling of Ultra High Molecular Weight Polyethylene under Large-Deformation and Cyclic Loading Conditions*. 2002, www.uhmwpe.org.

135. Lin, L. and A.S. Argon, *Review: Structure and Plastic Deformation of Polyethylene.* Journal of Materials Science, 1994. **29**: p. 294-323.

136. Ritchie, S.J.K., *A Model for the Large-Strain Deformation of Polyethylene.* Journal of Materials Science, 2000. **35**: p. 5829-5837.

137. Kurtz, S.M., et al., *Exponential Model for the Tensile True Stress-Strain Behaviour of As-Irradiated and Oxidatively Degraded Ultrahigh Molecular Weight Polyethylene.* Journal of Orthopaedic Research, 1996. **14**(5): p. 755-761.

138. Wang, A., C. Stark, and J.H. Dumbleton, *Mechanistic and Morphological Origins of Ultra-High Molecular Weight Polyethylene Wear Debris in Total Joint Replacement Prostheses.* Proceedings of the Institution of Mechanical Engineers, 1996. **210**: p. 141-155.

139. Bartel, D.L., V.L. Bicknell, and T.M. Wright, *The Effect of Conformity, Thickness, and Material on Stresses in Ultra-High Molecular Weight Components for Total Joint Replacement.* Clinical Orthopaedics and Related Research, 1986. **68-A**(7): p. 1041-1051.

140. Pruitt, L., et al., *Cyclic Copressive Loading Results in Fatigue Cracks in Ultra-High Molecular Weight Polyethylene.* Journal of Orthopaedic Surgery, 1995. **13**: p. 143-146.

141. Wang, A., et al., *Lubrication and and Wear of Ultra-High Molecular Weight Polyethylene in Total Joint Replacements.* Tribology International, 1998. **31**(1-3): p. 17-33.

142. Goodman, G.A., et al., *The Histological Effects of the Implantation of Different Sizes of Polyethylene Particles in the Rabbit Tibia.* Jornal of Biomedical Material Research, 1990. **24**: p. 517-524.

143. Wang, A., *A Unified Theory for Ultra-High Molecular Weight Polyethylene in Multi-Directional Sliding.* Wear, 2001. **248**: p. 38-47.

144. Bartel, D.L., et al., *The Effect of Conformity and Plastic Thickness on Contact Stresses in Metal Backed Plastic Implants.* Journal of Biomechanical Engineering, 1985. **107**: p. 193-199.

145. Psychoyios, A., et al., *Wear of Congruent Meniscal Bearings in Unicompartmental Knee Arthroplasty.* The Journal of Bone and Joint Surgery, 1998. **80-B**(6): p. 976-982.

146. Komvopoulus, K., N. Saka, and N.P. Suh, *The Role of Hard Layers in Lubricated and Dry Sliding.* Journal of Tribology, 1987. **109**.

147. Hertz, H., *Uber die Beruhrung Fester Elastischer Korper.* J. of Reine und Angewandte Mathematik, 1896. **92**: p. 156-171.

148. Johnson, K.L., *Contact Mechanics*. 1985, NY: Cambridge University Press. p. 84-135.

149. Boresi, A.P., R.J. Schmidt, and O.M. Sidebottom, *Advanced Mechanics of Materials*. 5th ed. 1993, NY: John Wiley & Sons, Inc. p. 716-718.

150. Persson, A., *On the Stress Distribution of Cylindrical Elastic Bodies in Contact*, in *Chalmers Tekniska Hogskola*. 1964: Goteborg.

151. Kalker, J.J., *On Elastic Line Contact.* Journal of Applied Mechanics, 1972. **39**: p. 1125-1132.

152. Ahmadi, N., L.M. Keer, and T. Mura, *Non-Hertzian Contact Stress Analysis for an Elastic Half Space-Normal and Sliding Contact.* International Journal of Solids Structures, 1983. **19**(4): p. 357-373.

153. Chiu, Y.P. and M.J. Hartnett, *A Numerical Solution for the Contact Problem Involving Bodies with Cylindrical Surface Considering Cylinder Effect.* Journal of Tribology, 1987. **109**: p. 479-485.

154. Rawlinson, J.J. and D.L. Bartel, *Flat Medial-Lateral Conformity in Total Knee Replacements does not Minimize Contact Stress.* Jornal of Biomechanics, 2002. **35**: p. 27-34.

155. Greening, D.R., *Automated Selection and Entry of Computed Tomography Data in Finite Element Modeling of the Human Femur*, in *Faculty of Engineering and Applied Science*. 1998, Memorial University of Newfoundland: Newfoundland, Canada.

156. Bernakiewicz, M. and M. Viceconti, *The Role of Parameter Identification in Finite Element Contact Analysis with Reference to Orthopaedic Biomechanics Applications.* Journal of Biomechanics, 2002. **35**: p. 61-67.

157. DeHeer, D.C. and B.M. Hillberry. *The Effect of Thickness and Nonlinear Material Behaviour on Contact Stresses in Polyethylene Tibial Components*. in *38th Annual Meeting of the ORS*. 1992. p. 327.

158. Li, G., M. Sakamoto, and E.Y.S. Chao, *A Comparison of Different Methods in Predicting Static Pressure Distribution in Articular Joints.* Journal of Biomechanics, 1997. **30**(6): p. 635-638.

159. Schroeder, U., et al. *The Influence of Tractive Force on the Shear Stresses in UHMWPE of a TKR Component*. in *Transactions of the 43rd Annual Meeting, Orthopaedic Research Society*. 1997. San Fransisco, California. p. 794.

160. Barbour, P.S.M., D.C. Barton, and J. Fisher, *The Influence of Contact Stress on the Wear of UHMWPE for Total Hip Replacement Hip Prosthesis.* Wear, 1995. **181-183**: p. 250-257.

161. Balasubramanian, V., et al. *Effect of Flexion on Stresses in UHMWPE Tibial Liners*. in *Transactions of the 43rd Annual Meeting, Orthopaedic Research Society*. 1997. San Fransisco, California. p. 793.

162. Baldini, T., et al. *Wear Damage is Affected by Conformity in Knee Joint Geometries*. in *Transactions of the Society of Biomaterials*. 1999. p. 25.

163. Kitaoka, H.B., *Salvage of Nonunion Following Ankle Arthrodesis for failed Total Ankle Arthroplasty.* Clinical Orthopedics and Related Research, 1991(268): p. 37-43.

164. Edidin, A.A., et al., *Degradation of Mechanical Behaviour in UHMWPE after Natural and Accelerated Aging.* Biomaterials, 2000. **21**: p. 1451-1460.

165. Perillo-Marcone, A., D.S. Barrett, and M. Taylor, *The Importance of Tibial Alignment.* The Journal of Arthroplasty, 2000. **15**(8): p. 1020-1026.

166. Huiskes, R. and E.Y.S. Chao, *A Survey of Finite Element Analysis in Orthopedic Biomechanics: The First Decade.* Journal of Biomechanics, 1983. **16**(6): p. 385-409.

167. Taylor, M., Tanner, K.E., and Freeman, M.A.R., *Finite Element Analysis of the Implanted Proximal Tibia: A Relationship Between the Initial Cancellous Bone Stress and Implant Migration.* Journal of Biomechanics, 1998. **No. 31**: p. 303-310.

168. Taylor, M. and K.E. Tanner, *Finite Element Modeling- Predictor of Implant Survival?* Journal of Materials Science: Materials in Medicine, 1995. **No. 6**: p. 808-812.